THE GEOMECHANICAL RESPONSE OF AXIALLY LOADED FULLY GROUTED ROCK BOLTS UTILIZING FIBRE OPTICS TECHNOLOGY

LA RÉPONSE GEOMÉCANIQUE DU BOULONNAGE À ANCRAGE RÉPARTI SOUS SOLLICITATIONS AXIALES EN UTILISANT LA TECHNOLOGIE FIBRE OPTIQUE

A Thesis Submitted to the Division of Graduate Studies of the Royal Military College of Canada by

Daniel Felipe Cruz, BEng, rmc
Second Lieutenant

In Partial Fulfillment of the Requirements for the Degree of
Masters of Applied Science

April, 2017

Dedication

This dissertation is dedicated to my friend and brother Harrison Kelertas (aka Harry the Frog), whose short life greatly influenced many, including myself. You have taught me so much without knowing it, and I can truly say that without you I would not be where I am today. Ad Vitam Cantavit.

Acknowledgements

I would like to express my sincere appreciation to my supervisor, Dr. Nicholas Vlachopoulos for his constant guidance and encouragement without which this dissertation would not have been possible. I am truly grateful for the unwavering support he provided throughout my stay at the Royal Military College of Canada (RMCC), as well as the many learning opportunities both at home and abroad that he made possible. I am also grateful for all the other members of the Civil Engineering Department for their help and support towards the completion of my studies in Kingston.

The work completed herein would not have been possible without the expertise and assistance provided by Mr. Bradley Forbes and Mr. Yannis Vazaios. I would also like to sincerely thank Mr. Dexter Gaskin and Mr. Steve Vanvolkingburgh for their invaluable support provided in the structures laboratory at RMCC.

My gratitude extends to Dywidag Systems International for supplying all of the reinforced bars used as part of this investigation, and YieldPoint for providing technical capabilities and the sensing equipment required for the success of this investigation.

Finally, I would like to thank my parents, Olga and Carlos, and my sister, Juliana, for the unconditional love and support that they have provided me throughout my whole life. I would also like to thank Elsie Pitman for her love and support throughout.

Abstract

Rock bolts have been used in mining and civil engineering applications for over 40 years, and have since been one of the primary surficial support systems for underground excavation projects. The main function of a rock bolt is to stabilize the rock mass around the opening of an excavation by fastening to more stable formations behind the excavation face. The lack of discrete design criteria with respect to rock bolts, as well as the emergence of infrastructure projects in more difficult conditions has led to an increase in ground falls associated with failure of the support member. Accordingly, this research programme aimed to increase the industry's understanding of how this support member functions by utilizing a newly developed Distributed Optical Sensing technology that provided an unprecedented spatial resolution of 0.625 mm. Fifteen (15) pull-out tests on rock bolts that were grouted within concrete specimens were conducted under similar loading conditions for different grout types, embedment lengths, and borehole sizes. The fibre optic technology was placed within diametrically opposing grooves that were machined into the bolt samples. This provided a high spatial resolution, continuous strain profile of all studied samples and therefore successfully obtained insight into the micro-mechanisms involved, overcoming the limitations of research previously conducted with conventional laboratory equipment.

This rigorous testing scheme systematically determined specific support features and interaction parameters within the rock bolts. It also enabled an in-depth look at the critical embedment length and failure mechanisms associated with this type of loading. These results were then compared with ten (10) numerical models, developed within the two-dimensional finite element method numerical modelling software RS2 (Phase2 9.0). Comparisons of the results from the laboratory testing programme and numerical models showed significant differences. These differences warrant further research into utilizing the physical results to improve these numerical modelling programs used for the analysis of geotechnical structures for civil and mining applications. Overall, the results included in this thesis substantially improve upon the industry's understanding of the inherent complexities of the axial loading mechanisms of fully grouted rock bolt support elements.

Resumé

Les boulonnages ont été utilisés pendant plus de 40 ans en génie civil et en génie des mines, et sont depuis devenus un des principaux systèmes de support superficiel pour les projets d'excavation. Ces boulons ont pour objectif principal de stabiliser la masse rocheuse autour de l'ouverture d'une excavation en se fixant à des masses plus stables derrière le front d'excavation. Le manque de critères discrets de design par rapport aux boulons d'ancrage et l'émergence de projets d'infrastructure dans des conditions plus difficiles ont mené à une augmentation d'effondrement des sols dû à des défaillances d'un équipement de support. En conséquence, ce programme de recherche vise à améliorer la compréhension de l'industrie de la façon dont ce membre de support fonctionne en utilisant une nouvelle technologie de Détection Optique Distribuée qui procure une résolution spatiale sans précédent de 0.625 mm. Quinze (15) essais d'arrachement sur des boulonnages qui avaient été cimentés dans des échantillons de béton ont été conduits sous des conditions de charge similaires pour différents types de ciment, de longueurs d'ancrage et de grosseur de trou borgne. La technologie de fibre optique a été placée à l'intérieur de rainures diamétralement opposées qui avaient été usinées dans des échantillons d'armature. Cela a procuré une haute résolution spatiale, un profil continu de la déformation en fonction de tous les échantillons étudiés et, ainsi, une meilleure idée des mécanismes microscopiques impliqués, surmontant les limites de la recherche qui avait été faite avec les instruments conventionnels de laboratoire.

Ce plan rigoureux de test détermine systématiquement les fonctionnalités spécifiques de support et leurs paramètres d'interaction avec le boulonnage. Cela permet également de voir en profondeur la longueur d'ancrage critique et les mécanismes de faillite associés à ce type de charge. Ces résultats ont par la suite été comparés avec dix (10) modèles numériques du logiciel d'analyse numérique de modélisation d'éléments finis en 2 dimensions RS2 (Phase2 9.0). La comparaison des résultats obtenus avec le programme de test de laboratoire et ceux obtenus avec la méthode numérique ont montré des différences significatives. Ces différences justifient la nécessité de recherches subséquentes afin d'utiliser les résultats physiques pour améliorer ces logiciels de modélisation numérique pour l'analyse des structures géotechniques pour des applications civiles ou minières. Les résultats inclus dans cette dissertation améliorent substantiellement la compréhension de l'industrie vis-à-vis la complexité du boulonnage à ancrage reparti sous sollicitations axiales.

Table of Contents

List of Figures

List of Tables

Notations

A = Cross sectional area

C = Cohesion

c = Speed of light

CV = Coefficient of variance

C_ε = Fibre strain constant

E = Young's modulus

E_b = Rebar Young's modulus

E_l = Embedment length

F_g = Gauge factor

F_y = Axial force

Ja = Degree of alteration or filling along the weakest joints

Jn = Number of joint sets

Jr = Roughness of weakest joint

K_ε = Strain calibration constant

J_w = Degree of water inflow (Jw)

k_n = Joint normal stiffness

k_s = Joint shear stiffness

n_{eff} = Fibre refractive index

r = Radius

S_t = Tensile strength

u = Displacement

v = Frequency

V_a = Acoustic velocity

w:c = Water to cement ratio

ΔF = Optical frequency range

Δl = Spatial resolution

Δz = Spatial resolution

A = Spacing in between gratings

ε = Strain

ε_y = Axial strain

λ = Wavelength

ν = Poisson's ratio

£ = Laser pulse width

σ = Normal stress

τ = Shear stress

ϕ = Friction angle

List of Abbreviations

2D = 2-dimensional

ASTM = American Society for Testing and Materials

BEM = Boundary Element Method

BOTDA = Brillouin Optical Time Domain Analysis

BOTDR = Brillouin Optical Time Domain Reflectometry

BPM = Bonded Particle Model

CFC = Continuously Frictionally Coupled

CMC = Continuously Mechanically Coupled

CSA = Canadian Standards Association

DAQ = Data acquisition system

DDA = Discontinuous Deformation Analysis

DEM = Distinct Element Method

DMFC = Discretely Mechanically of Frictionally Coupled

DOS = Distributed Optical Sensing

DSI = Dywidag Systems International

EMI = Electromagnetic Interference

FBG = Fibre Bragg Grating

FDM = Finite Difference Method

FEM – Finite Element Method

FOS = Fibre Optical Sensor

GSI = Geological Strength Index

LC = Lucent Connector

LVDT = Linear Variable Displacement Transducer

MHC = Modified Hoek Cell

MTS = Material Testing System

NGI = Norwegian Geotechnical Institute

ODiSI-B = Optical Distributed Sensor Interrogator

OFDR = Optical Frequency Domain Reflectometry

OTDR = Optical Time Domain Reflectometry

Q = Rock Mass Quality

RMCC = Royal Military College of Canada

RMR = Rock Mass Rating

RQD = Rock Quality Designation

RS2 = Rock and Soil 2-Dimensional Analysis Program

SEPT = Short encapsulation performance test

SG = Strain Gauge

SHM = Structural Health Monitoring

SRF = Stress reduction factor

STS = Splitting Tensile Strength

UCS = Uniaxial compressive strength.

1 INTRODUCTION

1.1 Purpose of Study

The design and implementation of support elements within underground excavations is a non-trivial pursuit, that when improperly employed can lead to the loss of not only valuable assets and infrastructure but also human life. Available design methods are largely based off empirical criteria that often constitute over conservative designs. As such, it is crucial for design engineers to have an adequate knowledge of the mechanical behaviour of individual support members as well as the complex interaction and influence between all elements within the support system. This constitutes not only knowledge of the surrounding rock mass but also explicit understanding of how each individual support member behaves in accordance with all of the possible loading conditions it may undergo throughout its life. Despite the best efforts of previous researchers there is currently limited knowledge on the mechanisms involved with the loading of these various types of ground support elements. The geomechanical response of the individual support elements in these support structures is a critical part of the considerations for developing a more complete understanding of how to best design not only underground excavations, but also a multitude of projects involving earthworks.

Rock bolts are one of the most commonly used temporary support elements in the field. Temporary support elements are charged with maintaining the load bearing capacity of an excavation before the final support is put in place. In this way, rock bolts are used as a first-pass technique of 'minimal support' that maintains the integrity and thresholds of the tunnel to provide a safe working environment long enough for the final lining to be prepared and constructed. As such, rock bolts play a pivotal role in helping support the rock during this critical stage; especially within weak rock masses. This research is part of a larger research program, spearheaded by Professor Nicholas Vlachopoulos and PhD candidate Bradley Forbes, investigating such temporary support systems in underground excavations. The research included in this thesis aimed to capture, analyze and determine the mechanistic response of fully grouted rock bolts loaded axially. Pull-out tests were performed in the RMCC structures laboratory to study the response of the support member under axial loading conditions. The tests consist of applying an axial load onto a rock bolt until failure occurs. Many of these pull-out tests have previously sought to analyse the effectiveness of rock bolt support systems (Azziz & Webb, 2003; Benmokrane, Chennouf, & Mitri, 1995; Mark, Compton, Oyler, & Dolinar, 2002; Signer, 1990).

In order to perform a detailed study, a Material Testing System (MTS) was modified in order to fit the boundary conditions and loading scenarios necessary for the study. A Distributed Optical Sensing (DOS) strain measuring technology

was utilized alongside conventional instrumentation commonly seen in laboratory environments and in previous research programs. This state of the art fibre optic technology has already been proven to work both in the laboratory and *in situ* (Forbes, 2015), and provides an unprecedented spatial resolution of 0.625 mm. All of the tests were performed with the same general setup shown in Figure 1.1. Several permutations of samples involving different grout and embedment lengths were used in a rigorous testing scheme that was focused on systematically determining specific support features and interaction parameters within the temporary support element. The data from these tests was then consolidated for use as validation in terms of numerical modelling with an emphasis to influence design and incorporation of relevant support.

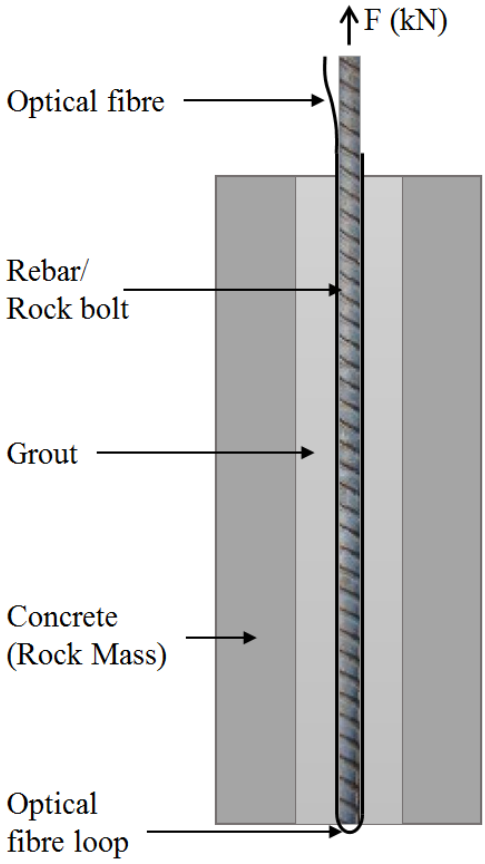

Figure 1.1 Typical testing setup including the use of optical fibre to measure strain

1.2 Research Objectives

The main objectives of the research included in this thesis were to:

1. Develop a laboratory testing scheme capable of properly monitoring fully grouted rock bolts subjected to axial loads. This included:

    a. Designing a rig capable of holding specimens of various sizes throughout the required loading sequence;
    b. Selecting conventional instrumentation to be used;
    c. Implementation of fibre optic technology to monitor the strain deformation of bolt samples; and,
    d. Selection of testing parameters.

2. Conduct a rigorous physical laboratory testing program with a specific emphasis on:

    a. The critical embedment length for fully grouted rock bolts;
    b. Specific loading mechanisms; and,
    c. Failure mechanisms.

    The testing program addressed the limitations of previous research endeavours. Overall 15 pull-out tests were performed on 14 distinct specimens. The attained results were analysed in order to study the mechanical behaviour of fully grouted rock bolts.

3. Simulate the physical testing results within the frame of numerical modelling software RS2 (Phase2 9.0) in an attempt to determine the limitations associated with the industry standard numerical modelling software that is used for these purposes.

The completion of each of these objectives occurred sequentially as one stage was necessary for the subsequent one to progress. Overall, the accomplishment of said objectives led to an increase in scientific knowledge as related with the micro-mechanisms associated with the axial loading of fully grouted rock bolts.

1.3 Thesis Organization

This thesis has been prepared in traditional format following the thesis writing guidelines as provided by the Royal Military College of Canada (RMCC). The thesis was written surrounding a central issue as covered in Section 1.1. The organization of the included chapters and their contents are as follows (as seen in Figure 1.2):

Chapter 1 – Introduction: This chapter introduces the main themes and objectives associated with this research as well as providing a general introduction to the overall framework and context of the problem at hand.

Chapter 2 – Background: This chapter gives an overview of underground excavation works, with an emphasis on rock bolt support members. It discusses the current understanding of the behaviour of fully grouted rock bolts and points out the various scientific gaps that can be highlighted in previous work.

Chapter 3 – Rock Bolt Monitoring and Instrumentation: This chapter includes a review of the conventional techniques that are used in order to instrument and monitor temporary support members. The chapter introduces the selected technology (*i.e.* Rayleigh distributed sensing), which was chosen in an attempt to address the highlighted scientific gaps.

Chapter 4 – Materials: This chapter includes an overview of all of the used materials as well as the preparation of the testing samples. It covers the preliminary uniaxial compressive strength, splitting tensile strength and tensile tests performed in the RMCC structures laboratory. These tests were performed in order to determine the properties of all of the materials used throughout testing.

Chapter 5 – Laboratory Testing Program: This chapter discusses preparation of all pull-out test specimens. The chapter also covers the rationale behind the testing setup used throughout testing. The extensive physical laboratory testing program along with the testing procedures followed throughout the experimental work are covered. This includes an overview of all of the variables of interest, selected conventional instrumentation, as well as the non-trivial capturing and processing of data through data acquisition (DAQ) software.

Chapter 6 – Numerical Modelling: This chapter highlights the importance and relevance of numerical modelling within the context of the study of the behaviour of underground excavation support elements. A brief overview of how numerical models function is included. The rationale behind the parametric modelling procedure performed is discussed, including the selection of input material properties, and model geometry.

Chapter 7 – Results and Discussion: This chapter provides a summary of the results associated with the conducted tests. This includes results from conventional instrumentation, the state of the art fibre optic instrumentation, as well as numerical modelling efforts. It highlights the major findings associated with this research.

Chapter 8 – Conclusions and Recommendations: This chapter summarizes the contributions of this research program to Civil and Mining Engineering industries, including the primary conclusions that can be drawn from results. It additionally highlights possible areas of future work within the scope of the study.

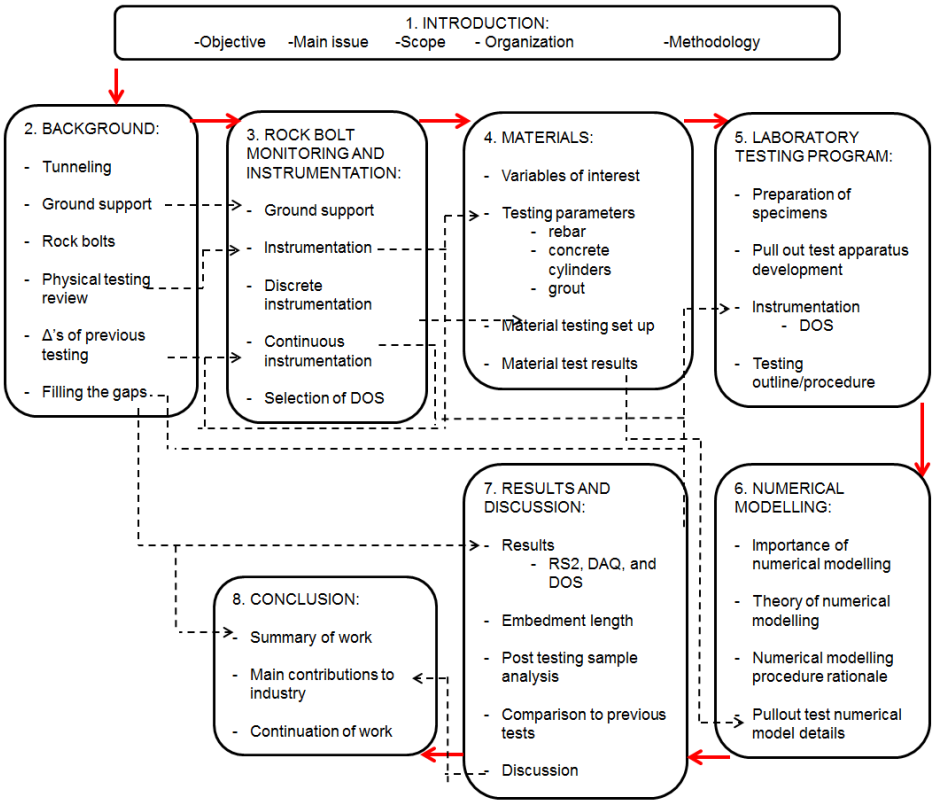

Figure 1.2 Organization, Themes and Methodology of Thesis Document

1.4 Relevance to Research

This Chapter introduced the main themes and objectives associated with this investigation. It provided a general introduction to the framework and context of the main research problem at hand.

2 BACKGROUND

2.1 Introduction

Rock bolts have been used for over 40 years in mining and civil engineering applications, as part of a reinforcing system in underground excavations, due to their ease of installation, efficiency, and relatively low costs (Stillborg, 1986). They function to reinforce a rock mass by restraining the deformation around the periphery of the excavation. In this manner, the stresses experienced by the rock mass decrease and are transferred to the rock bolt as mainly axial loads. In mining, bolts are predominantly used as support elements for low entry excavations, whereas in civil and geological engineering applications, bolts are used in order to reinforce excavation sites such as roadway and railway tunnels. As such, the proper use of these support elements for applications *in situ* is crucial. Improper techniques and installations can lead to the loss of lives and elevated project costs. This highlights the importance in understanding the composition of this reinforcing element, not only within the overall support scheme when using rock bolt support, but also at the smaller scale in all of the different components that contribute to their performance. In this chapter, the themes and methodologies associated with rock bolt support are covered. Additionally, an overview of previous research endeavours is included to highlight the existing scientific gaps with respect to the support element.

2.2 Rock Support

Instability problems are generally associated with two separate scales: the global and the local scale. The former involves an entire orebody, mine/excavation infrastructure and surrounding rock mass. Conversely, the latter involves the immediate rock surrounding an underground excavation. Generally, the stability of an underground excavation is affected by the chosen geometry of the opening (Kaiser, Yazici, & Nose, 1992; Peng & Tang, 1984). This includes the magnitude and orientations of the *in situ* stresses, the excavation sequence, the location of shafts and ore-passes, pillar sizes in between stopes, and the location of other excavation infrastructure such as cross passages. However, at the local scale, the stability of an opening is mainly dependant on the stress and conditions of the rock mass a small distance away from the actual excavation boundary. In these conditions rock will converge towards zones of lower stress.

Within the design of support for underground excavations and openings, it is local scale instability problems with which engineers are concerned with. Rock support in this case refers to the steps taken and materials used in order to maintain

the load bearing capacity of the rock near the opening of an excavation (Brady & Brown, 2004; Hoek & Wood, 1987). The use of rock bolts within these conditions of local instability is paramount. Support within underground openings covers a wide range of subsets including: rock bolts, dowels, cables, mesh, straps, shotcrete and steel ribs (as seen in Figure 2.1). These different support members are used in a wide array of combinations in order to minimize the instability of a rock mass around an opening. Such arrangements are more fully described by Vlachopoulos (2009).

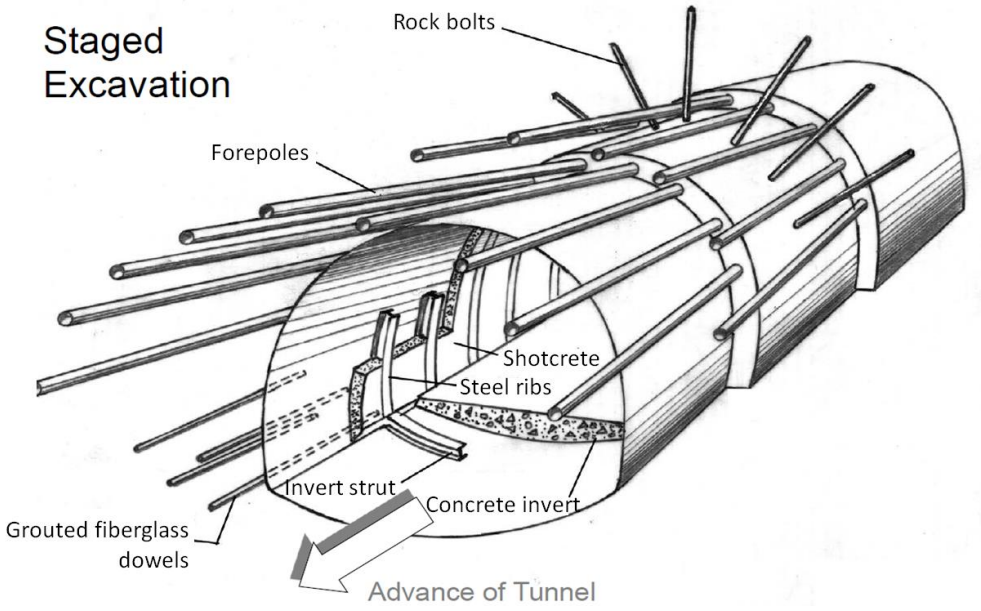

Figure 2.1: Example of Support Elements Commonly Used within Underground Excavations (modified after Hoek, 2000)

The term ‘support’ is commonly used as a ubiquitous term to denote all procedures and materials used to support and reinforce a rock mass. However, it more accurately describes the scenario where the supporting members are external to the rock mass. In this manner, the member applies support only when movement of the rock around the excavation boundary has occurred, and the member applies a supporting load external to the rock mass at the excavation periphery. This is regarded to as passive rock support and includes materials such as shotcrete, mesh, steel ribs, and concrete liners. On the other hand, rock bolts function in a much different manner as they become an integral part of the ground. In this case, the member provides reinforcement to the rock mass, successfully conserving or

improving the rock mass properties through means such as ground anchors, cable bolts, and rock bolts. This is, throughout the literature, referred to as 'active support' (Barton N. , 2012; He, An, & Zhao, 2015; Hoek & Wood, 1987). These definitions were introduced by Windsor & Thompson (1993) and are accepted throughout the literature.

Traditionally, rock support is also described as being either temporary or permanent. Temporary support refers to the first-pass techniques used in order to ensure safe working conditions for workers during mining and excavation stages of a project. For projects that require to be operable for extended periods of time (*i.e.* 50-plus years), permanent support is installed. Modern day practice now regards support and reinforcement techniques as being either primary or secondary (Brady & Brown, 2004). Primary support or reinforcement is that which is applied during or immediately after the excavation, in a way as to conserve the inherent strength of the rock mass. Additional support installed at a later stage is known as secondary support.

Overall, rock support/reinforcing systems use a combination of reinforcement: through elements such as tensioned bolts and cables, and support: through elements such as shotcrete, and steel ribs. These aid the rock mass to support itself such that the loads experienced within the individual support element are smaller than those acting on the rock (Stillborg, 1986).

2.3 Rock Bolts

Rock bolting is one of the most commonly used support/reinforcing techniques in underground excavations. A wide selection of bolts is readily available to meet the different requirements of both mining and civil engineering environments. The most basic make up of a rock bolt support system consists of a plain steel rod which is mechanically or chemically anchored at one end, and contains a face plate or nut at the other end. The bolt can be tensioned after installation in such a way that the bolt applies a positive reinforcement force to the face of the opening. The following section covers the many different rock bolts that are often encountered as an integral part of support systems within underground openings.

2.3.1 Mechanically Anchored Rock Bolts

Mechanically anchored rock bolts were the most commonly used type of bolt up until the late 1970s in the vast majority of underground coal mines in the USA (Peng & Tang, 1984). These end anchored systems function by tensioning a steel rod between a face plate and nut arrangement (at the borehole collar) and an anchor (at the toe end of the bolt) as seen in Figure 2.2. The anchor is composed of

a tapered cone with an internal pair of wedges that is held in place by a bail. The cone is inserted into one of the threaded ends of the bolt, which is then inserted into a pre-drilled borehole. The anchor is set in place by pulling sharply on the bolt. The faceplate is necessary in order to distribute the load built up along the bolt onto the rock surface.

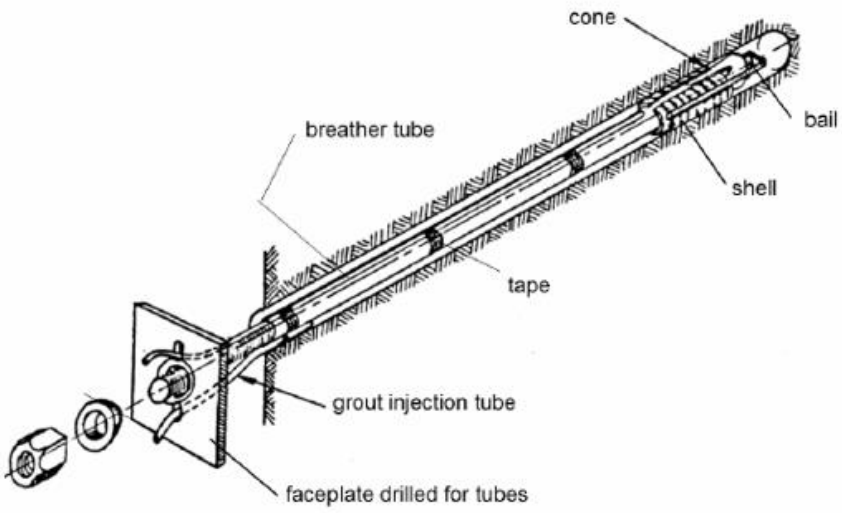

Figure 2.2: Mechanically anchored rock bolt (Hoek & Wood, 1987)

Mechanically anchored rock bolts are normally tensioned up to 70% of their ultimate bearing load and immediately reinforce the ground. They are extremely useful in the retaining of loose blocks of rock caused by intersecting joints and bedding planes. This type of bolt is known to work well in hard rock, but has issues in cases where closely jointed (*i.e.* average joint spacing of 5 mm to 15 mm) or soft rocks are expected. This difficulty is attributed to the deformation and failure of the contact between the rock and wedge grips. This causes the wedges to sink within the borehole wall in soft rock conditions.

2.3.2 Fully Grouted Rock Bolts

Fully grouted rock bolts were initially proposed to reduce the corrosion observed with the use of mechanically anchored rock bolts as they have the entire embedded length of the bolt and borehole annulus grouted with either a cement-based or resin-based grout as seen in Figure 2.3. In this manner, the grout provides a protective barrier from moisture within the ground. Resin grout is made up of two component cartridges: a polyester based resin and an organic peroxide based

hardener. The cement grout is made up of a mixture of cement, water, and other admixtures which are used to improve the mechanical properties of the mixture. Installation of fully resin anchored rock bolts proceeds by placing cartridges ahead of the bolt in the borehole. The plastic sheath containing the cartridges breaks when the bolt is spun into the borehole and the two components are mixed together. Fully cement grouted rock bolts are installed by grouting the cement mortar into the borehole once the steel bar has been placed within the borehole. As with mechanically anchored rock bolts, a faceplate and nut are put in place at the excavation face to hold the supporting system in place once the grout has set.

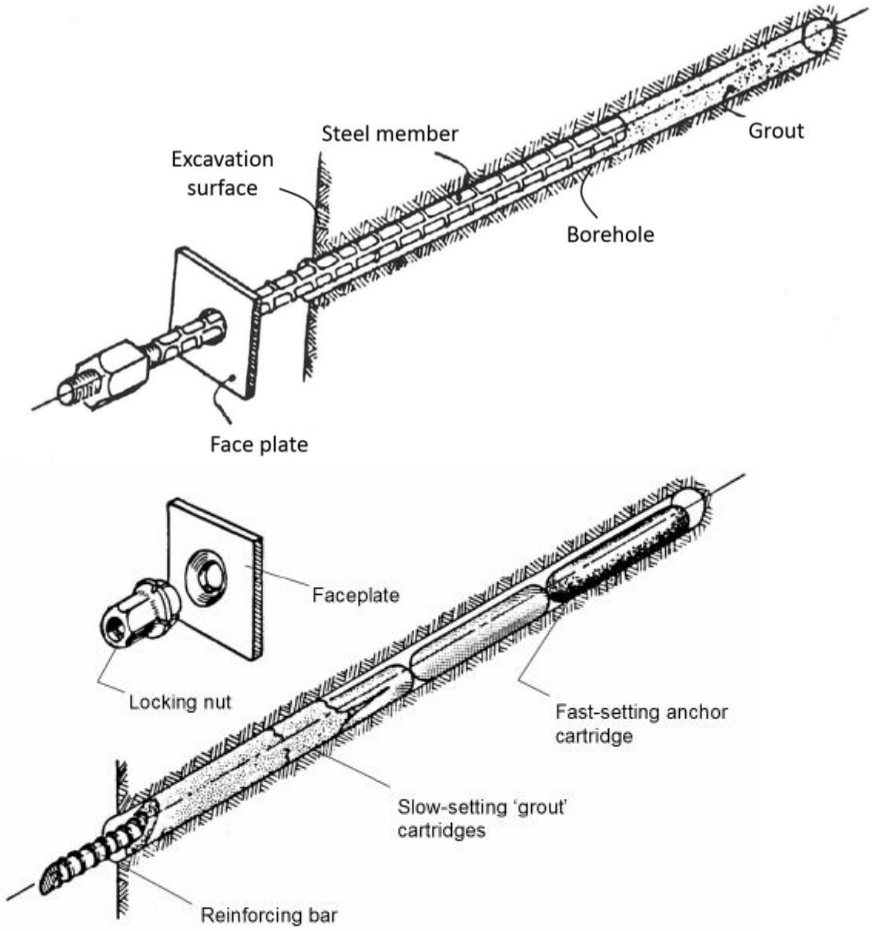

Figure 2.3: Top; Fully cement grouted rock bolt. Bottom; Fully resin grouted rock bolt (Hoek & Wood, 1987)

The use of resin over cement mortar as a grout has some advantages including:

1. It sets faster than cement;
2. It is easier to handle;
3. It does not degrade over time; and,
4. It does not shrink during the curing process.

However, resin grout is not without its drawbacks, most notable it is more expensive than cement-based grouts. Other disadvantages encountered with the use of resin are the poor mixing of the resin and hardener during installation, as well as gloving (Campbell & Mould, 2005). Gloving occurs when the plastic cartridge partially or entirely encases a section of the bolt. This reduces the bonding effectiveness of the bolt and decreases the bolt's efficiency in reinforcing the ground.

Fully grouted rock bolts can be used to immediately support an unstable rock mass close the excavation face. This allows the support member to be put in place before the ground experiences any significant movements. Since the member becomes an integral part of the rock mass, no active force is applied to excavation face. In this sense, the bolt provides reinforcement to the ground and is an example of passive support. As with mechanical anchors, tension can be applied to a resin anchored rock bolt by using a slow setting resin near the excavation boundary. When the bolt is spun into place, the faster setting resin near the toe end of the bolt will quickly set and allow a tensioning force to be applied to the bolt, prior to the setting of the slower resin near the borehole collar. This locks in the applied tension and results in a fully tensioned and grouted rock bolt where the bolt applies an active supporting force on the excavation face. However, it has been found that there is little benefit gained from tensioning these sorts of bolts as there is enough shear strength developed along the length of the bolt to support the loads it will take on throughout its lifetime (Haas, 1975).

Fully grouted rock bolts can be used in a plethora of ground conditions including weak shales and mudstones. They are commonly used in areas that show severe roof conditions and have helped mining proceed in regions previously not possible (Peng & Tang, 1984). To improve the anchoring that exists between the bolt and the borehole annulus, bars are often made with ridges. The bars are called reinforcing bars (rebars). Rebars create a rock joint-like interface between the ridges (also known as ribs) and surrounding grout material. A rougher bolt profile is known to increase the capacity of a rock bolt as rebar has been proven to withstand up to 7 times the loading of a smooth rod (Fabjanczyk & Tarrant, 1992). Overall, in modern day practice the fully grouted rock bolt with rebar is the most used reinforcing element in both mining and civil engineering applications (Li, 2007).

2.3.3 Frictionally Anchored Rock Bolts

Friction rock bolts can generally be split up into two types: *Split Set* and *Swellex* bolts (as seen in Figure 2.4). They both provide a frictional anchor along the entire length of a borehole, and are extremely useful in mild rock burst environments since they tend to slip rather than rupture. They are therefore used with mesh to hold back bursting rock pieces. To install a *Split Set* bolt, a high-strength hollow steel tube is pushed into a hole that is of smaller size than the bolt itself. The radial spring force generated in this process is the source of the frictional anchoring force that holds the bolt in place.

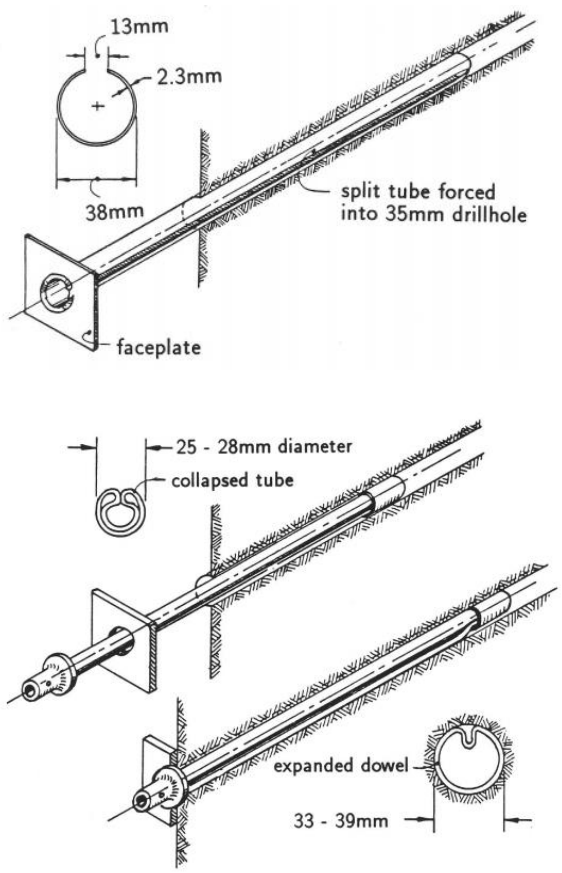

Figure 2.4: Top; *Split Set* rock bolt. Bottom; *Swellex* rock bolt (Hoek, Kaiser, & Bawden, 2000)

Swellex bolts on the other hand consist of a steel tube that is folded in during manufacturing. The tube is inserted into a 33mm to 39mm hole and

expanded using high water pressure. This inflates the folded tube and causes the edges of the bolt to come into contact with the borehole annulus. The *Swellex* bolt works well in fractured ground experiencing low to medium stress conditions.

Frictionally anchored bolts are beneficial as they provide a fast and simple installation procedure that provides immediate support to the excavation face. They should therefore be installed prior to any significant movement of the rock mass taking place, in order to conserve the inherent strength of the ground. These sorts of bolts have issues when used in regions experiencing high water flow as these conditions increase the risk of corrosion of the high strength steel of which both members are made. This can be minimized by galvanizing the tube to increase its resistance to corrosion. However, especially in areas where long term support is required, other bolts should be considered since rusting can greatly affect the reinforcing capacity of the member.

2.3.4 Fully Grouted Rock Bolts Load Transfer Mechanics

Proper knowledge of the load transfer mechanisms associated with the use of fully grouted rock bolts is essential to the success of an excavation. Knowledge of these mechanisms helps design engineers understand the mechanics associated with each individual component within a project (Cao, Jan, Ren, & Naj, 2013). Windsor (1997) proposed that a reinforcement system comprises of 4 main elements, as seen in Figure 2.5:

1. the rock;
2. the reinforcing element itself;
3. the internal fixture; and,
4. the external fixture.

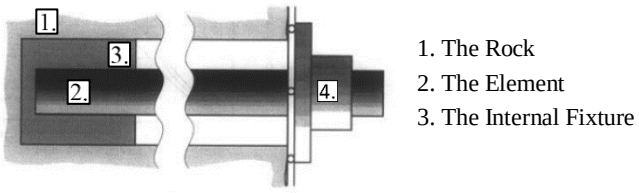

Figure 2.5 Components of a reinforcing system (modified after Windsor, 1997)

As it pertains to rock bolts, the reinforcing element is the bolt itself. The internal fixture is a medium that is attributed with the transfer of load from the rock to the element. This could either be a medium such as cement grout (for fully grouted rock bolts) or an actual mechanical action such as friction (in the case of frictionally anchored rock bolts). The external fixture is the face plate and nut

arrangement at the excavation periphery that simply helps distribute the load throughout the system.

The internal fixture is of great importance to the transfer of load in a rock bolt system since it provides a coupling interface between the rock and the element. With regards to rock bolting, the mechanics associated with the reinforcing of a rock mass can be classified into three main divisions (Windsor, 1997):

1. Continuously Mechanically Coupled (CMC) – *i.e.* fully grouted rock bolts;

2. Continuously Frictionally Coupled (CFC) – *i.e.* friction anchored rock bolts; and,

3. Discretely Mechanically or Frictionally Coupled (DMFC) – *i.e.* mechanically anchored rock bolts.

It is understood that, for fully grouted rock bolts (*i.e.* CMC bolts), the shear strength present at the bolt-grout interface is made up of three main components: adhesion, mechanical interlock, and friction. Adhesion is the inherent chemical bond that exists between the different interfaces. Mechanical interlocking is the embedding effect that is created between the irregularities of the grout, borehole annulus, and the rebar ribs. Friction is the resisting force generated as a surface moves over another. These three components of shear strength are lost in sequence as a fully grouted rock bolt is incrementally loaded, and compatibility of deformation along the interface is lost (Li & Stillborg, 1999). At the onset of this behaviour, the remaining shear strength is regarded as the residual shear strength of the interface.

All loads taken on by a bolt are transferred to the surrounding media through this shear strength/resistance. Previous work has stated that there is little if any adhesion between the bolt-grout and grout-rock interfaces (Azziz & Webb, 2003; Signer, 1990). This is due to the fact that the adhesion cannot be mobilized along with the ultimate frictional strength of the bolt (Stillborg, 1984). Therefore, throughout the lifetime of a fully grouted rock bolt, the mechanical interlock due to the asperity at the bolt-grout interface is the predominant component of this bond shear strength, up to the moment where compatibility amongst the interfaces in the system fails and movement begins (Cao, Jan, Ren, & Naj, 2013).

Depending on the *in situ* stresses, the mechanical properties of surrounding media, and the orientation of joints and bedding planes within the rock mass, load can be induced on a fully grouted rock in two separate manners. As shown in Figure 2.6, the existence of intersecting joints and bedding planes (*e.g.* discontinuities in the figure) can cause a loose piece of rock (*i.e.* a rock wedge) to

move towards the opening of an excavation. This effectively applies a load onto the bolt in two separate mechanisms, depending on the alignment of the rock bolt with respect to the discontinuities. The load experienced by the bolt in this manner can be composed of a combination of both axial and shear components. The existence of joints can also cause only a section of a bolt to be completely bonded to the borehole annulus. This bonded section of the bolt is referred to as the embedment length of the bolt (also referred to as anchorage length in the literature).

In cases where only axial loading is applied to the bolt, the axial force is at a maximum at the location of the discontinuity. This location is regarded as the neutral point of the bolt - which together with the anchor length and pick-up length make up the three different regions along the embedment length of a bolt (Freeman, 1978) as shown in Figure 2.7. The pick-up length refers to the section of the bolt near the borehole collar that takes on load from the incoherent rock mass close to the excavation boundary. The anchor length defines the region beyond the neutral point towards the end of the bolt where it is anchored to a more coherent rock mass.

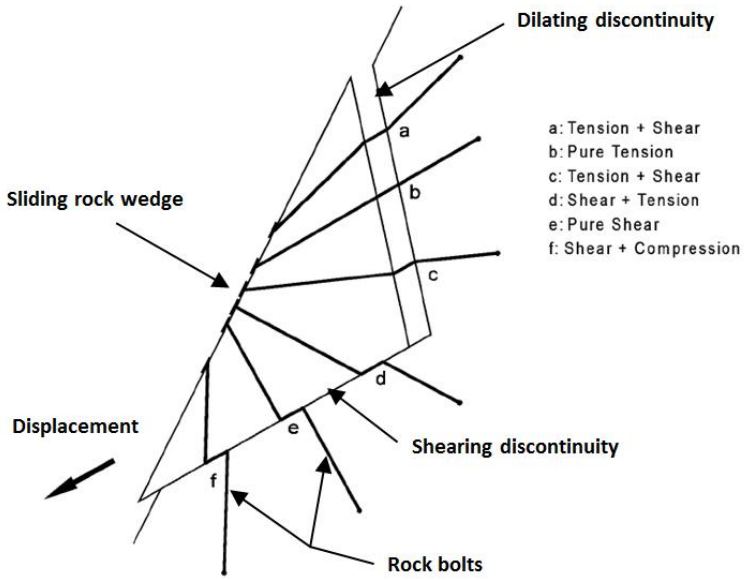

Figure 2.6: Loading of rock bolts caused by a sliding rock wedge (modified after Barley & Windsor, 2000)

To contrast this loading scenario, in cases where a rock mass behaves as a continuous media, the greatest movement is experienced at excavation boundaries.

Along the bolt itself, the maximum load will be experienced at the borehole collar (Hyett, Bawden, Macsporran, & Moosavi, 1995; Li & Stillborg, 1999). These conditions are seen in homogeneous rock masses as well as in highly fractured ground conditions. The external fixture of the fully grouted rock bolt plays an important role in these situations as the movement of the rock towards the centre of the opening causes the face plate and nut to transfer the load to the bolt. This increases the effectiveness of the transfer of load from the bolt to the rock mass.

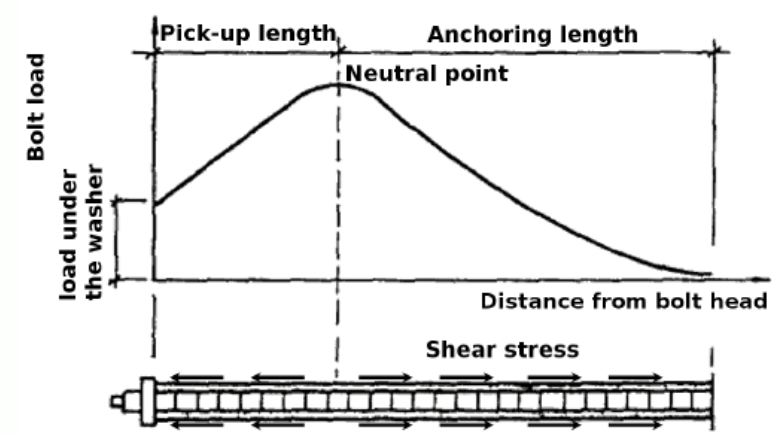

Figure 2.7: Load distribution along a rock bolt (Stille, 1992)

Overall, load is transferred within a fully grouted rock bolt through three main processes (Windsor, 2004):

1. As the ground experiences movement, load is transferred from an unstable region to the reinforcing element;
2. Load is transferred from the unstable region to a stable region via the rock bolt; and,
3. The load on the element is transferred to a stable rock mass.

The internal fixture (*i.e.* the grout) transfers load between the rock and the reinforcing element. This is a result of movements within the rock-mass, whether they are associated with dilating joints, or relaxation of stresses. Thus, rock bolts are able to reinforce and support a rock mass in the following means (Figure 2.8):

A. Deterioration control: In cases where a strong rock mass exists in low stress levels, the existence of cracks, joints, and cross-beds can cause loose pieces of rock near the surface of the excavation. Rock bolts prevent these rock pieces from falling or slipping without sacrificing the stability of the excavation profile;

B. Rock mass reinforcement and support: This is seen in cases where a weak layer of rock is created due to the changing *in situ* stresses caused by an excavation. Rock bolts clamp these weaker rock layers together in order to improve the mechanical properties of the rock mass as a whole. In cases where an undisturbed region of the ground exists close to the excavation boundary, the weaker layers of rock are also suspended from the more coherent rock unit at a greater distance from the excavation boundary; and,

C. Rock mass confinement: This occurs where a compressive layer of rock is created as the bolt is loaded. This damaged rock belt helps confine the stable rock mass.

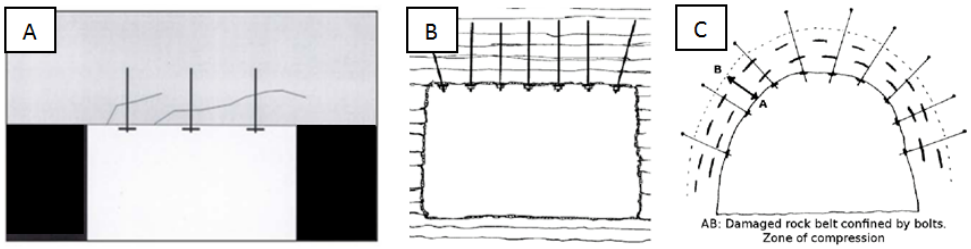

Figure 2.8: Rock bolt support and reinforcement roles: A. Deterioration control (Mark, 2000); B. Rock mass reinforcement and support (Stillborg, 1986); C. Rock mass confinement (Tincelin & Fine, 1991)

2.3.5 Rock Bolt Failure

The orientation of rock bolt installation in comparison to the rock mass movement vector is a significant factor in the loading of the support member. A bolt is loaded axially when ground movements are coaxial with the alignment of the bolt. When this is not the case, a fully grouted bolt undergoes shear loading as seen in Figure 2.9. Movements associated with these stresses can arise from a combination of sources including: shearing along a bedding place, vertical sag, and dilation of a roof layer (Mark, Compton, Oyler, & Dolinar, 2002). Failure of the system as a whole in such cases depends on many factors including:

1. The mechanical properties of individual components;
2. The characteristics of the installation including grout quality, type of surrounding media, and installation procedures; and,

3. The locations of discontinuities.

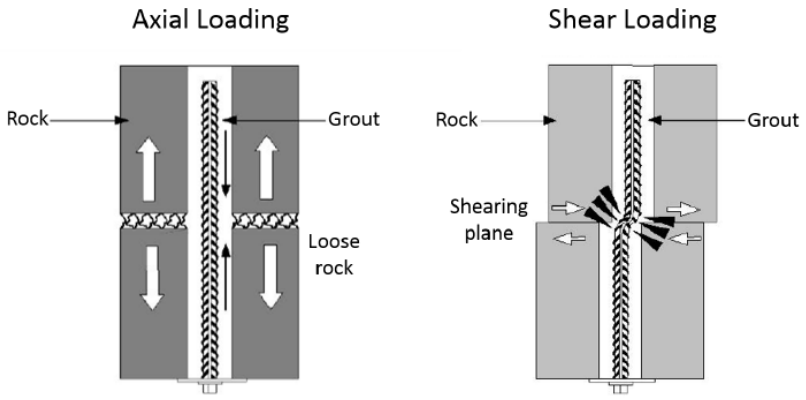

Figure 2.9: Typical loading conditions for rock bolts (modified after Mark, Compton, Oyler, & Dolinar, 2002)

In this regard, a rock bolt support system can be expected to fail at any of the individual components or along either the bolt-grout or the grout-rock interface. Specifically, the following failure modes are expected when only axial loading is applied to a rock bolt (Serbousek & Signer, 1987) as seen in in Figure 2.10:

1. Grout failure;
2. Bolt failure in tension; and,
3. Failure of the grout column.

Grout failure differs from failure of the grout column in that it consists of the failure of the actual grout whereas the latter consists of failure along either the bolt-grout or grout-rock interfaces due to inadequate embedment length. It is generally accepted that for fully grouted rock bolts, failure is most likely to occur at the bolt-grout interface through a decoupling mechanism, as explained in Section 2.3.4.

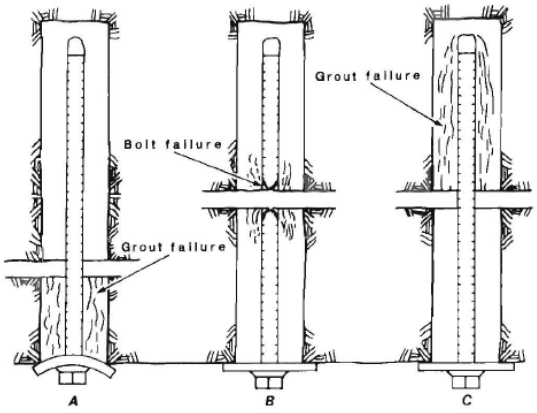

Figure 2.10: Axial Loading Failure Modes (Serbousek & Signer, 1987)

The failure of the bolt-grout interface proceeds through one of two main mechanisms: radial splitting of the concrete cover surrounding the bolt and shearing of the bolt along the grout annulus (Hyett, Bawden, & Reichert, 1992; Tepfers, 1979). The former consists of two separate modes that arise due to the tensile distribution of stresses within the grout and rock. The concentrations of stresses experienced by a rock bolt cause the bolt to pull out and either cone-shaped cracks or longitudinal splitting cracks will initiate once the tensile capacity of the grout is exceeded (as seen in Figure 2.11). The geometry of the interface as well as its properties (and surrounding material properties) affect the manner in which radial splitting will ensue. In contrast to this failure mode, shearing of the bolt against the grout annulus involves the crushing of the grout ahead of the ribs on the rebar. This results in the pulling out of the bolt along a cylindrical frictional surface.

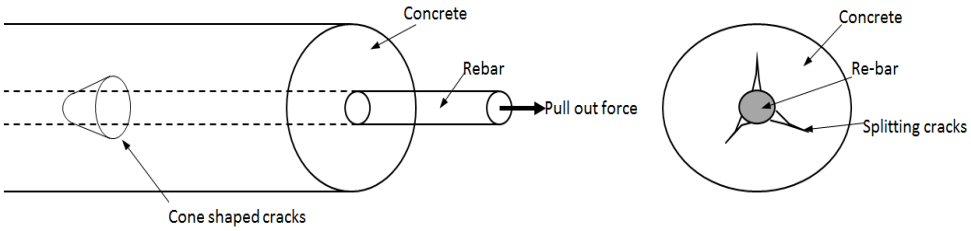

Figure 2.11: Radial splitting modes (modified after Tepfers, 1979)

It is generally accepted that the failure mechanism is governed by the amount of radial confinement present at the interface (Hyett, Bawden, & Reichert, 1992). Samples existing in low radial confinement will undergo radial splitting whereas samples existing in states of higher radial stiffness will experience

shearing of the grout at the bolt-grout interface. Both of these failure mechanisms cause the bolt to pullout as loading continues.

2.3.6 Design of Rock Bolt Support System

The design of underground works is a non-trivial undertaking that has become increasingly more demanding as the demand for larger subterranean works grows. Underground projects can fail for many different reasons including: poor design, inferior materials, substandard construction, poor supervision, and unforeseen ground conditions (Barton N. , 2012). There are numerous solutions available to help an engineer properly design a proper support system including:

1. Existing standards and empirical methods;
2. Closed form solutions (*i.e.* analytical models); and,
3. Numerical models.

In the exploration and early design stages of underground works, little information is available to help engineers make informed decisions about the most appropriate type and amount of support to be used. Available information is mainly composed of regional geology maps, geophysical studies, surface mapping and exploration boreholes. Often very little geotechnical information is provided from exploration drilling programmes and as such, only very basic rock mass classification exists on which to base the initial decision of rock support required around an excavation. To improve the amount of geotechnical data available, a geotechnical technician carefully logs the core. The resultant data is used to construct a more detailed rock mass classification of the area and to help plan further site investigations. As work continues on a project, more information becomes available to help improve the initially chosen design criteria. Accordingly, once initial laboratory testing has helped to determine the most basic material strength parameters, design can proceed with the use of the three solutions highlighted herein.

Numerical models consist of the use of available methods to help predict the response of the rock mass with different support selections. This makes it possible to select the more suitable support implementation for a given situation. In many of the available numerical modelling software, various types of rock bolts are included as members that can be easily implemented into the model. This makes it possible to help design bolting patterns. Further details on numerical models will be discussed in Chapter 6. Similarly, analytical models make it possible to predict the response of individual bolts, as implemented into the support scheme. There are numerous analytical models that can be implemented, some of which are covered in more detail in Section 2.4. Analytical formulas are limited in that several assumptions need to be made prior to their implementation, such as elastic

behaviour of the ground, homogeneous ground, and isotropic ground. Finally, empirical design solutions are based largely on rock mass classification systems and past experience. Due to the limited information available in the early design stages of an excavation, rock mass classifications aid in making primary support decisions. The main objectives of a rock mass classification system are (Bieniawski, 1993):

1. To identify the most significant parameters influencing the behaviour of a rock mass;

2. To divide a rock mass into a number of rock mass classes of differing qualities;

3. To provide a basis for understanding the characteristics of each rock mass class;

4. To derive quantitative data for engineering design;

5. To recommend support guidelines for tunnels and mines;

6. To provide common basis for communication between engineers and geologists; and,

7. To relate experiences at different sites.

A quantified and discrete classification aids in proper and effective communication as a foundation for sound engineering judgement on a given project (Hoek E. , 2007). One of the earliest examples of a rock mass classification system is seen in Deere's Rock Quality Designation (RQD), which was first used in 1964 and was developed as an index of rock quality (Deere, Hendron, Patton, & Cording, 1967). The method consists of counting the pieces of rock core that are of 100 mm in length or more – a length that was chosen after considering a reasonable limit for fair quality rock mass with three or four joint sets. The quality of the rock is then judged, depending on the percentage of rock core that is retrieved, as being either: excellent, good, fair, poor, or very poor. In this manner, sound rock requires less intensive support techniques.

Although RQD offers a technique to evaluate the effects of fracturing, shearing, and alteration, it does not take into account other factors such as joint orientation, joint continuity, gouge material, the friction angle of altered joint fillings, and the roughness or planarity of joint walls. Accordingly, Bieniawski's Rock Mass Rating System (RMR) (Bieniawski, 1993), and the Rock Mass Quality

System (Q) (Barton, Lien, & Lunde, 1974) were developed to improve RQD. RMR takes the following parameters into account:

1. RQD index;
2. State of weathering;
3. Uniaxial compressive strength of intact rock;
4. Spacing of joints and bedding;
5. Strike and dip orientations;
6. Separation of joints;
7. Continuity of joints; and,
8. Groundwater inflow.

The Q-system, which was initially proposed by the Norwegian Geotechnical Institute (NGI), contains the combination of six classification parameters:

1. RQD index;
2. Number of joint sets (Jn);
3. Roughness of the weakest joints (Jr);
4. Degree of alteration or filling along the weakest joints (Ja);
5. Degree of water inflow (Jw); and,
6. Stress reduction factor (SRF).

These rock mass classification systems use their perspective criteria to arrive at a final RMR or Q-value with the use of an empirical formula. The RMR defines the rock mass class, and different support implementations are recommended for different classes – including rock bolting specifics. An example of the support categories specified for different rock classes under the Q-system can be seen in Figure 2.12.

To contrast these systems of classification, the Geological Strength Index (GSI) was developed by Everit Hoek and Paul Marinos to be used in weaker rock masses where RQD is meaningless (Hoek E. , 1994). The method consists of estimating rock mass properties as defined by the Hoek-Brown failure criterion from the intact rock mass. It relies on the visual analysis of a rock mass including the assessment of its lithology, structure and the condition of the present discontinuities. The system is geologically sound as it takes into account the two fundamental parameters of the geological process: the blockiness of the mass and the conditions of discontinuities. Once a GSI number is decided upon by using one of the developed charts, the rock mass properties can be estimated with the use of empirically developed formulas. Different support classes are then suggested for different rock mass classes, as developed from previous experience.

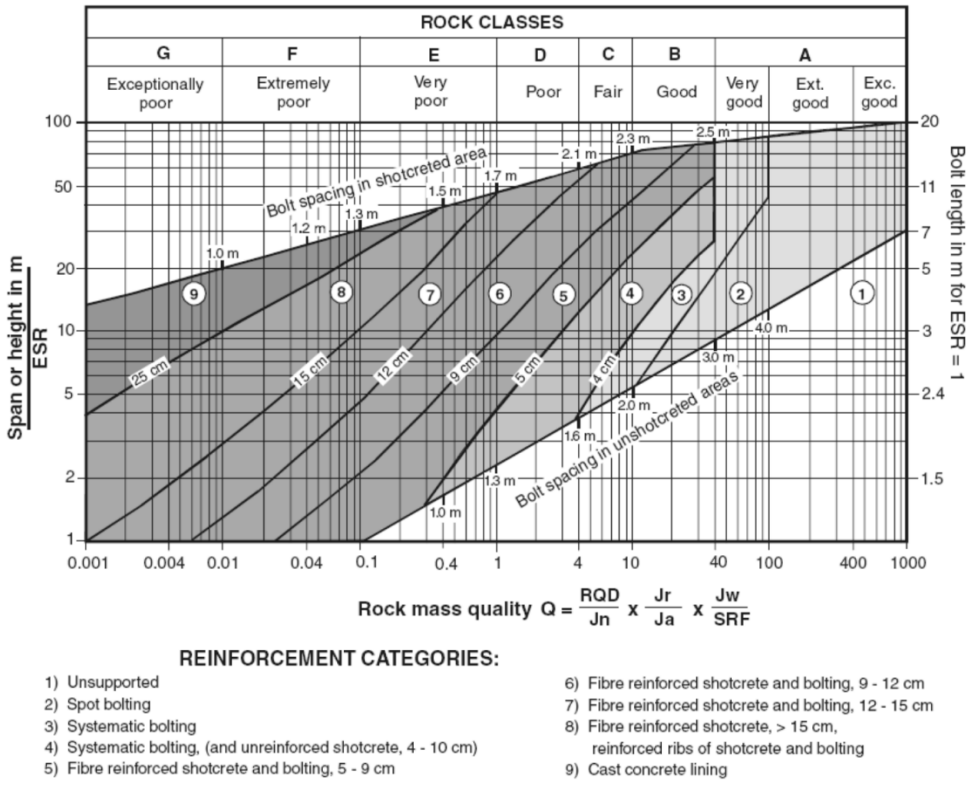

Figure 2.12: Estimated support categories based on the tunneling quality index Q (as seen in Hoek, 2000)

The use of a combination of design methods available makes it possible for design engineers to develop a rock bolting support system capable of withstanding the loading expected throughout its serviceability life. Overall, the reinforcing pattern of a rock bolt support system requires the following parameters to be determined prior to installation:

1. Bolt type;
2. Bolt length;
3. Bolt diameter; and,
4. Bolt spacing.

Consequently, the difficult conditions encountered in underground excavations have made it difficult for one design method to be widely accepted. In the end, important support design decisions are left up to the experience of the

engineer and are generally based on what has worked in the past. The use of a combination of design techniques is a common successful solution to design a rock bolt support system.

2.4 Historical Research

The understanding of the behaviour of fully grouted rock bolts has been subject to a multitude of different research programs. The specific loading scenario for cases solely experiencing axial loads can be seen in Figure 2.13. The embedded section of the bolt on the upper rock mass corresponds to the load carrying section of the bolt. Since the research at hand is focused on studying the behaviour at the bolt-grout interface, it is assumed that the bolt and surrounding media properties are of higher quality than the interface itself (*i.e.* stiffer). In this manner, the shear stress distribution existing along an infinitesimal length (*dy*) section on the bolt can be defined as:

$$\pi {r_b}^2 d\sigma = 2\pi r_b \tau_b dy \tag{2.1}$$

Where r_b is the radius of the bolt and τ_b is the shear stress along the bolt. Here, y denotes the axial direction along the bolt. Accordingly, the shear stress distribution at the interface is equated to the change in axial stress along the embedment length, or the rate at which load is transferred.

In 1975, Farmer developed analytical models that considered the bolt to be an elastic steel rod resin grouted into different materials. The models presented both thin and thick grout annuli. For the thing grout annuli model the shear stress at the bolt-grout interface was representative of the shear stress in the annulus itself.

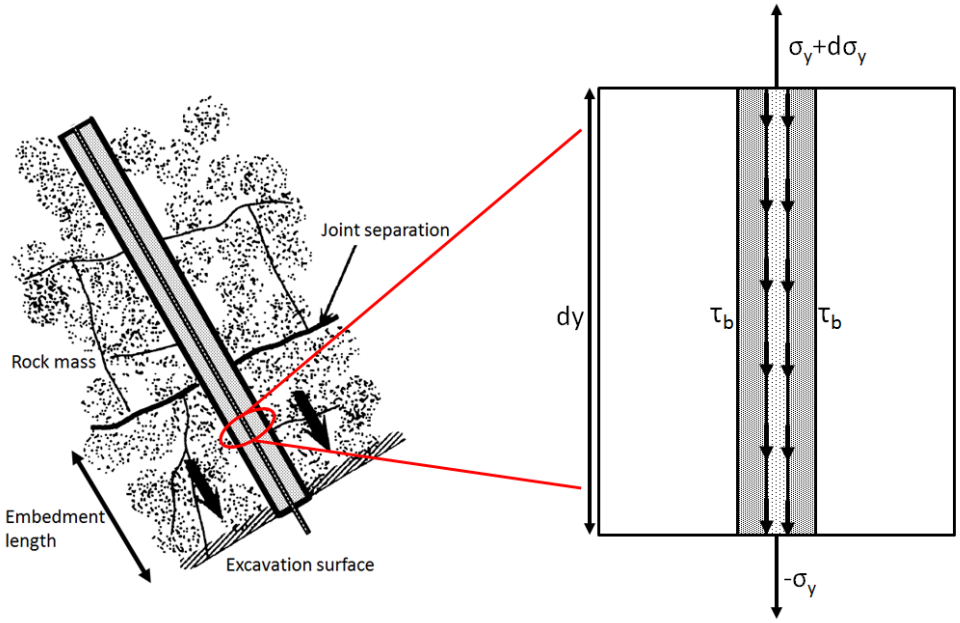

Figure 2.13: Loading Scenario (modified after Hyett, 1992)

Farmer developed analytical formulas that yielded non-linear strain and shear stress distributions along the embedded section of the bolt shown in Figure 2.14. In this manner, the load applied on a bolt is dissipated across a length, starting from the point where the load is applied. Farmer called this length, the transfer length, and defined it as the length where the strain and sresses experienced by the bolt are reduced to 1% of their initial magnitude at the borehole collar. Afterwards, Farmer resin grouted 20 mm diameter rebar bolts into different materials and conducted a series of laboratory tests to study the maximum load carrying capacity of the fully grouted rock bolt and the shear distribution along the grouted length of the bolt.

These results were significant since they were one of the first instances where a focus was placed on the behaviour at the bolt-grout interface, and a non-uniform stress distribution was hypothesized. However, as the laboratory results pointed out, the developed formulas were only able to simulate the response of the bolt at low axial loads. The decoupling mechanism that can be observed at the interface was not emphasized and as such, at higher loads, the analytical models and laboratory results diverged from one another. Performing an axisymmetric finite element method (FEM) analysis of a pullout test, Fuller and Cox were also able to simulate this non-linear strain distribution (1975). Results from other laboratory research programs were also in agreement with the modelled

exponential decay of load along the bolt (Dunham, 1976; Fuller & Cox, 1975; Serbousek & Signer, 1987; Signer, 1990).

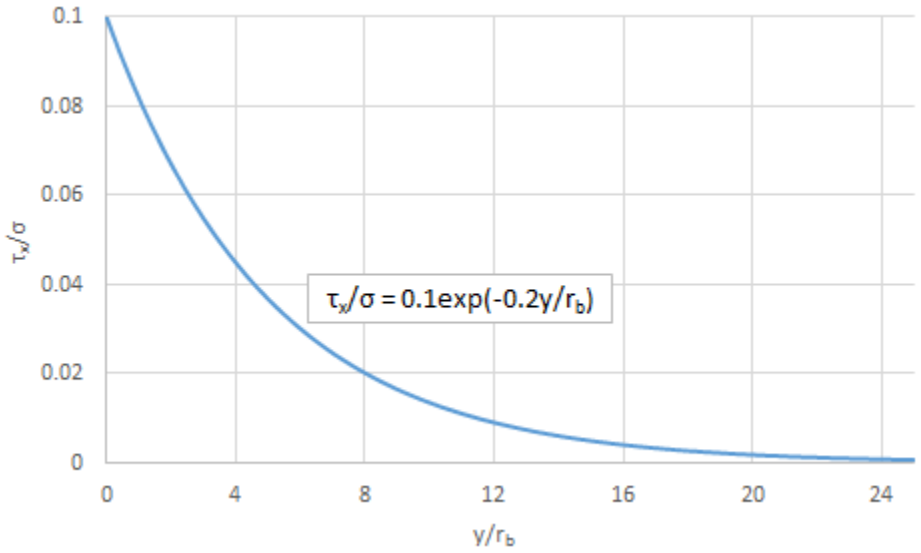

Figure 2.14: Theoretical stress distribution along a fully grouted rock bolt (modified after Farmer, 1975)

In 1995 Benmokrane *et al.* conducted a laboratory study on two separate rock bolt types: a 7-wire stranded cable bolt and a *Dywidag* solid steel thread-bar (1995). The bolts were cement grouted into 200 mm diameter concrete cylinders. The concrete cylinders were used to simulate the host rock. A tri-linear slip model was developed in order to correlate the interaction between the shear bond stress and the shear slip. Where tests such as Farmer's placed emphasis on the shear stress distribution along the bolt-grout interface, Benmokrane *et al*. analysed the bond-slip relationship at the bolt-grout interface. Accordingly, the interface shear strength is calculated by dividing the pull-out load by the surface area of the interface under Equation (2.2).

$$\tau_b = \frac{F_y}{2\pi r_b E_l} \tag{2.2}$$

This interface shear strength (or bond strength) interacts with the slip of the bolt across the interface under the following proposed formula:

$$\tau_b = ms + n \tag{2.3}$$

Where *s* is the shear slip and *m* and *n* refer to coefficients that change across different observed loading stages. In this manner, only the bond-strength is emphasized as the shear distribution at the interface is not analysed. These results are associated with the average shear strength present at the interface and make the assumption that the shear distribution is uniform across the entire embedded section of the bolt.

The tri-linear slip model is broken up into three main stages as seen in Figure 2.15. In the first stage of the model, an ascending branch is linked with the elastic behaviour between the axial slip and shear stress. The peak value corresponds to the interface shear strength. In the second stage of the model, a descending branch can be linked to the ongoing decoupling at the bolt and grout interface. In the third stage of the model, the residual interface shear resistance is seen as a plateau.

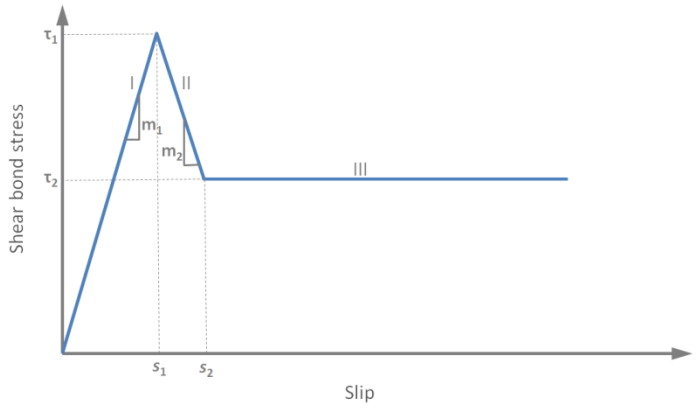

Figure 2.15: Tri-linear slip model (Benmokrane, Chennouf, & Mitri, 1995)

Another point of interest in Benmokrane's tests was the effect of the embedment length on the load capacity of a rock bolt. Results showed that the maximum pull-out force increases almost linearly with an increase of embedment length. These results agree well with those from other research programmes (Goris, 1990; Hyett, Bawden, & Reichert, 1992; Kilic, Yasar, & Celik, 2002).

To explain the discrepancies previously seen in the shear stress distribution at the bolt-grout interface at higher loads, Li & Stillborg (1999) introduced the idea of a decoupling front. This decoupling front begins once a certain load is reached, and moves towards the far end of the bolt as loading continues. In this manner, the decoupling front moves away from the loading point to the far-end of the specimen and denotes the separation between the coupled and decoupled section along the embedment length of a bolt. Three different models were introduced for both CMC

and CFC rock bolts: a model of a pull-out test situation, a model for rock bolts within uniformly deformed rock masses, and a model for rock bolts existing in dilating joint conditions. The models are based on the description of the mechanical coupling occurring between a bolt and grout and the exponential decay theory previously derived by Farmer (1975). Figure 2.16 shows the simplification of this model for the shear stress experienced by an axially loaded fully grouted rock bolt.

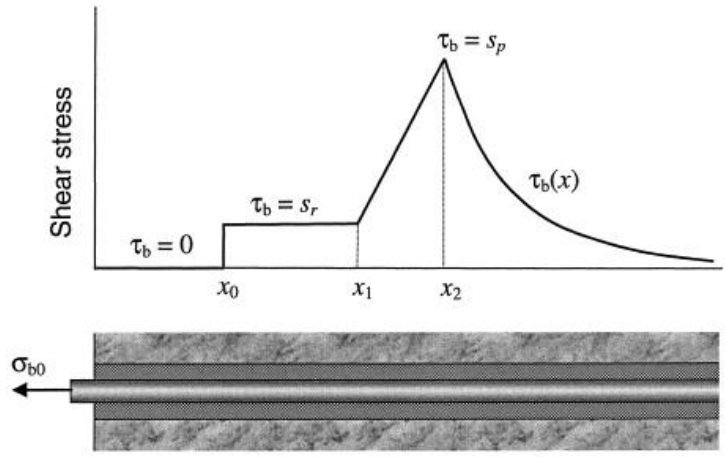

Figure 2.16: Theoretical shear stress distribution along a fully grouted rock bolt (Li & Stillborg, 1999)

One of the most recently proposed analytical models expands upon this decoupling (or debonding) behaviour and looks at the behaviour of the bolt along a full loading range (*i.e.* up until the bolt is completely pulled out of the borehole) (Ren, Yang, Chen, & Chen, 2010). Closed-form solutions for the prediction of the behaviour of grouted rock bolts are proposed for the load displacement relationships, distributions of shear stress, axial stress, and shear slip. Under the conditions of the model, the deformation of the surrounding rock and grout is negligible. This is due to the massive volume and stiffness of the surrounding rock in comparison to those of the bolt. The bolt is therefore assumed to be under uniaxial tension, whereas the bolt-grout interface is under interfacial shear deformation only. This leads to the idealised model that can be seen in Figure 2.17, in which failure is assumed to occur at the bolt-grout interface.

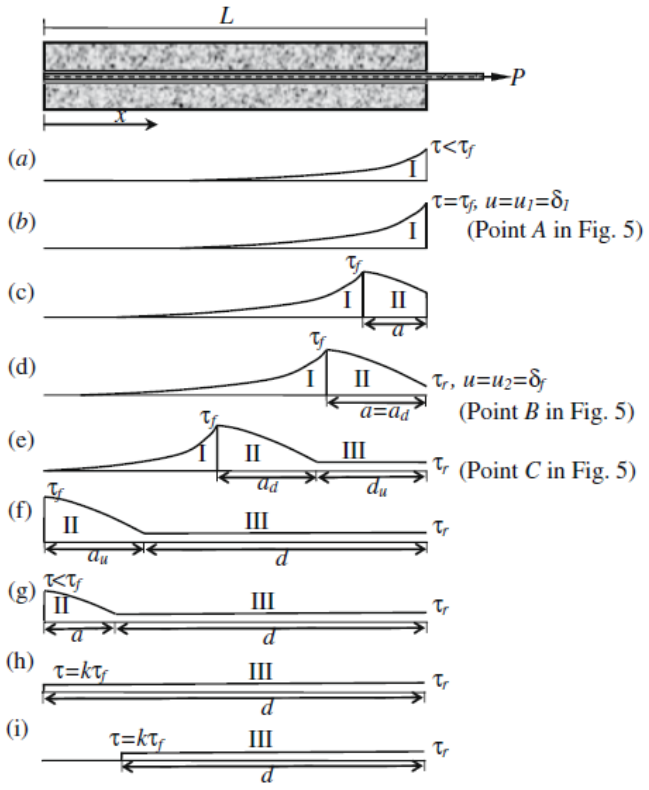

Figure 2.17: Evolution of interfacial shear stress distribution and propagation of debonding (Ren, Yang, Chen, & Chen, 2010)

The model uses boundary conditions and the tri-linear slip model previously developed by Benmokrane *et al*. (1995) to predict the shear stress distribution as decoupling occurs at the bolt-grout interface. This allows an analysis of the shear slip, shear stress distributions along the interface, axial stress in the bolt, and load displacement behaviour of the system. The stages highlighted in Figure 2.17 are:

1. Elastic stage (*i.e.* a – b);
2. Elastic-softening stage (*i.e.* c – d);
3. Elastic-softening-debonding stage (*i.e.* e – f);
4. Softening-debonding stage (*i.e.* g): and,
5. Debonding stage (*i.e.* h – i).

The stages are controlled by the behaviour at the bolt-grout interface. The softening region on a bolt consists of an interface that has not fully debonded. In the final stage, as the bolt is progressively pulled out of the borehole, the pull-out load decreases as there is a decreasing length of interface interaction between the bolt and grout.

2.4.1 Historical Research Scientific Gaps

As seen in the sections above, much work has previously been performed with a view to understand the mechanics associated with axially loaded, fully grouted rock bolts. However, the understanding of the response of the support member is still not fully understood. The following scientific gaps are present in previous research endeavours:

1. Previous results did not take into account the decoupling that occurs at the bolt-grout interface;
2. Only shorter embedment lengths were tested in most research endeavours due to the necessity of assuming that there exists an uniform shear stress distribution across the interfaces;
3. Previous analysis of results only used the average shear stress present at the interface to analyse the mechanisms associated with axial loading (*i.e.* minimal research done to look at stress distributions along the embedment length);
4. Previous tests did not have a sufficient strain sampling scale in order to capture or determine the specific micro-mechanisms that may be present and ultimately influence performance; and,
5. Laboratory testing programs were incapable of adequately confirming the accuracy of analytical models due to the lack of analysis of the stress distributions.

In general, it can be stated that these scientific gaps have led to limited knowledge of the support member as a whole system. This has limited the progress made in order to improve the available design solutions covered in the chapter. Accordingly, more work is warranted, specifically, to the end of better understanding the loading mechanisms associated with axially loaded fully grouted rock bolts.

2.5 Relevance to Research

This chapter focused on the background necessary to provide a solid foundation for the underlying concepts associated with this body of research. It presented an overview of underground excavation works, emphasizing on the use of rock bolt support members. The various types of bolts commonly used were described. Current scientific understanding of the mechanics associated with the loading of fully grouted rock bolts was detailed. Furthermore, the scientific gaps in the literature were also covered herein.

3 ROCK BOLT MONITORING AND INSTRUMENTATION

3.1 Introduction

Pull-out tests, also known in the literature as anchorage capacity tests, are the most common method used to analyse the effectiveness of the load transfer that occurs within a rock bolt support system. These tests can be performed both in laboratory environments and *in situ*. *In situ*, pull-out tests are generally done in order to analyse the efficiency of the reinforcing system as a whole. One such way to categorize the *in situ* efficiency of a rock bolt is by using conventional instrumentation such as strain gauges, deflection gauges, pressure gauges, and pressure transducers. These instruments have made it possible to measure the load at which failure is observed, which is commonly regarded as the anchorage capacity of the support system. This can then be normalized to create an anchorage factor, making it possible to compare the results of pull-out tests at different sites (Mark, Compton, Oyler, & Dolinar, 2002).

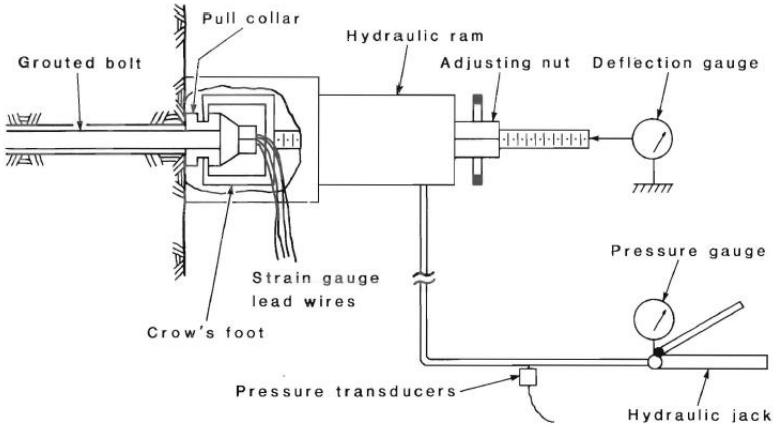

Figure 3.1: Typical pull-out test setup (Serbousek & Signer, 1987)

On the other hand, laboratory pull-out tests are focused on analysing general tendencies seen with the variation of a specific component within a rock bolt support system. It is common practice to grout rebar into a rock sample, or into a man-made sample. The latter are designed in such a way as to simulate the mechanical properties of the rock. Pull-out testing involves applying a tensile load onto a rebar specimen up to the point where failure occurs, and the system is incapable of taking on any additional load. Conventional instrumentation is installed within the boundaries of the testing rig in order to record the required data as seen in Figure 3.1.

3.2 Conventional Instrumentation

The applied load and displacement experienced at the borehole collar are the most commonly monitored values in testing. This adequately captures the behaviour of the system as a whole to be represented in a typical load displacement graph. Load cells are the most common instrument used to monitor the amount of load applied to a test subject. Load cells are transducers which come in many forms including mechanical, hydraulic, photo-elastic, and electrical. The most common load cell configuration consists of utilizing strain gauges to measure force indirectly by measuring the strain that is produced on a calibrated carrier as seen in Figure 3.2. Pressure transducers are also commonly connected directly to the hydraulic jack that is used to apply the load to the bolt. This makes it possible to monitor the applied load directly.

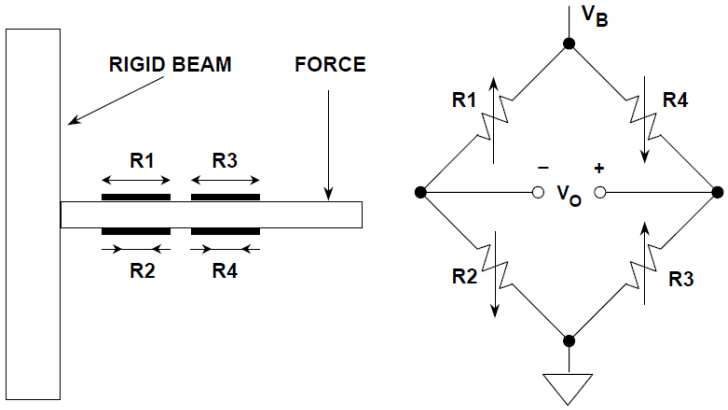

Figure 3.2: Using strain gauges to measure force (Chapter 3: Sensors, 2007)

Dial gauges were commonly used in the past to monitor the deflection at the end of the rebar as seen in Figure 3.1. However, due to the relatively low fidelity data that can be retrieved from such instrumentation, electrical transducers are more frequently seen in more modern testing. A Linear Variable Differential Transformer (LVDT) is an electromechanical transducer used to measure linear deflections *in situ* and in the laboratory. As seen in Figure 3.3, an LVDT consists of a moveable core of magnetic material (nickel-iron) and three coils. As the magnetic core moves within the coil assembly a potential difference is generated, which can be calibrated to measure displacement. LVDTs offer good accuracy, linearity, sensitivity, infinite resolution, as well as frictionless operation and ruggedness.

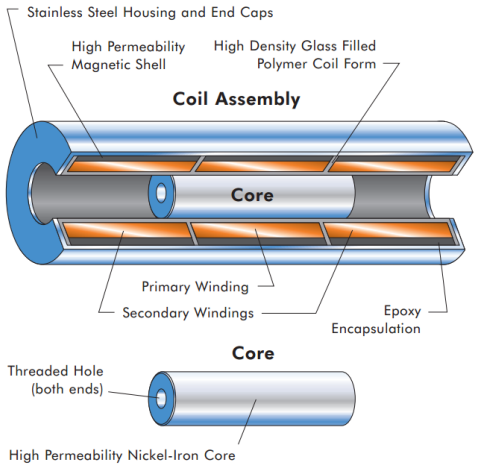

Figure 3.3: LVDT composition (Macro Sensors, 2014)

The cumulative performance of rock bolts has been successfully represented in previous research endeavours using instrumentation such as dial gauges, LVDTs, load cells, and pressure transducers (Farmer, 1975; Benmokrane, Chennouf, & Mitri, 1995; Serbousek & Signer, 1987). Since these techniques offer very little insight into the variability of the loading profile along the length of the bolt, additional instrumentation may be added to the bolt itself. In this manner, the axial strain experienced along the bolt is monitored as loading progresses.

Strain is measured *in situ* and in the laboratory most commonly with the use of strain gauges. Strain gauges consist of a small diameter wire attached to a backing material commonly made of plastic. Strain gauges are installed by orienting them such that they are co-linear with the direction along which strain is of interest. Wires (*i.e.* leads) connect the strain gauge to an electrical circuit which measures the change in resistance as the strain gauge changes in length. For proper measurements to take place, the strain gauge must be precisely coupled with the surface of the testing material. This is achieved by following a set of procedures as highlighted by Johnston and Cox (1993), and as covered in Section 4.5.

Examples of the use strain gauges are commonly found in the literature (Farmer, 1975; Goris, 1990; Serbousek & Signer, 1987). This manner of instrumentation allows the monitoring of the experienced strain at various positions along the bolt as seen in Figure 3.4. These measurement points can then be interpolated to create a plot of the strain distribution along the axis of the bolt. However, as the strain gauges are commonly installed externally on the rebar (*i.e.* the bolt) they may interfere with the interaction between the bolt and grout. This

may influence results and improperly represent the load transfer mechanisms being studied.

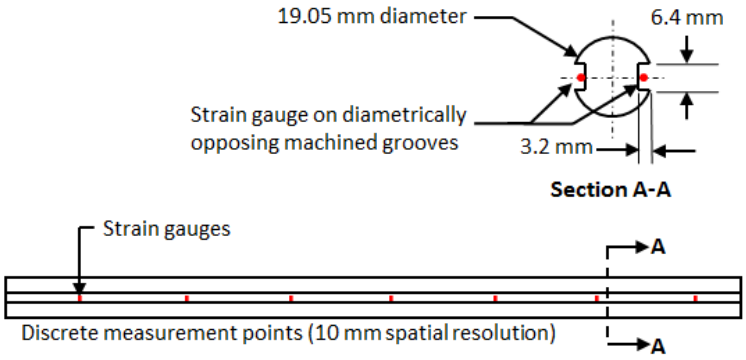

Figure 3.4: Instrumentation of bolts using strain gauges (modified after Serbousek and Signer, 1987)

In order to avoid interfering with the bolt-grout interface mechanics, research has been focused on developing in-destructive types of monitoring instruments. These include the installation of internal strain gauges (Mitri, 2011) as well as SMART bolts (Bawden & Lausch, 2000). The latter focuses on cable bolts and as such, will not be discussed further. The former involves the installation of internal strain gauges within a coupler by drilling a hole along the axis of the bolt. The coupler contains the strain gauges and is attached to the bolt within this drilled hole. This allows the measurement of axial deformation along the bolt at locations where a strain gauge has been placed within the coupler.

3.2.1 Conventional Instrumentation Limitations

As previously discussed, a vast amount of research has been performed both *in situ* and in laboratory environments utilizing much of the highlighted conventional instrumentation (Benmokrane, Chennouf, & Mitri, 1995; Blanco Martin, 2012; Farmer, 1975; Fuller & Cox, 1975; Kaiser, Yazici, & Nose, 1992; Mark, Compton, Oyler, & Dolinar, 2002; Serbousek & Signer, 1987) In most cases reviewed, only the load and deflection are monitored at a single point along the entire rebar alignment. However, the ground in which rock bolts are installed is anisotropic and inhomogeneous. Therefore, categorizing the response of the support system as a whole in this manner makes it impossible to analyse the load transfer mechanics associated with loading at the micro-scale. Likewise, it has been shown that the common practice of normalizing bolt capacities should be avoided as longer embedment lengths do not portray linearity (Hyett, Bawden, & Reichert,

1992). Additionally, in cases where the rebar (*i.e*. bolt) is discretely monitored with strain gauges, large sections of the bolt go unmonitored. This leaves unmonitored gaps in between instrumented sections of the bolt, which can lead to improperly representing the mechanics in these regions by means of interpolating between values. In essence, local phenomena might be completely missed if the rebar is not discretely instrumented at the exact location where a significant loading feature may occur. Overall, the data from these strain measurements is limited by the amount of discrete strain gauges that can practically be installed on a rebar. This is governed by the amount of space required by the gauge itself, the number of connecting wires required, economic considerations, and time constraints. This lack of spatial resolution in conventional strain instrumentation has given rise to a partial understanding of the complex mechanical behaviour at hand. Overall, the inherent limitations associated with the use of conventional instrumentation have diminished the overall quality and accuracy of previous pull-out testing investigations.

Suitably, an optimal method of monitoring the axial strain along the bolt must be looked at in order to improve upon the setbacks of conventional forms of instrumenting. Innovative techniques for capturing the strain along the bolt come in the form of fibre optic sensors. Such solutions have vastly been used in Civil Engineering applications as part of structural health monitoring (SHM) (Barrias, Casas, & Villalba, 2016; Lanticq, et al., 2009; López-Higuera, Cobo, Incera, & Cobo, 2011). They have also successfully been used to monitor the response of underground support members (Forbes, Vlachopoulos, Oke, & Hyett, 2014).

3.3 Fibre Optic Sensors

In the past four decades there has been an increase in the interest of the development of fibre optics and optoelectronics technologies. This increase in interest was initially associated with the utilization of fibre optics in the medical field with their use in endoscopic applications (National Instruments, 2011). In the 1960s, the efficacy of fibre optics within the telecommunications industry was proposed since fibre was found to have much lower attenuation rates in comparison to previously used copper wires. Additionally, fibre is able to carry much greater amounts of data than copper wires. The use of fibre within the telecommunications industry was made possible by the development of low loss optical fibres in the late 1970s (Udd & Spillman, 2011). The technology has since significantly reduced in cost and improved in quality. The main benefits associated with the use of fibre optics are (Dakin, 1990):

1. Immunity to electromagnetic interference (EMI);

2. Nonconductive;
3. Electrically passive;
4. Low loss/attenuation;
5. High bandwidth;
6. Small and lightweight; and,
7. Relative low cost per sensor compared to other conventional solutions.

A standard optical fibre consists of three main components: a glass core, a cladding layer, and an outer buffer coating. The core is made up of a thin strand of glass through which light is guided. The cladding keeps the light within the core through reflection and refraction according to Snell's law since the core has a higher refractive index than the cladding (Figure 3.5). This ensures minimal signal loss. The buffer coating offers protection from external conditions and minimizes physical damage. Further layers are also common in order to provide more ruggedness and protection depending on the application. Overall, the outer diameter of an optical fibre ranges anywhere between 145 and 250 micrometers – or about the size of a human hair (Glisic, 2013).

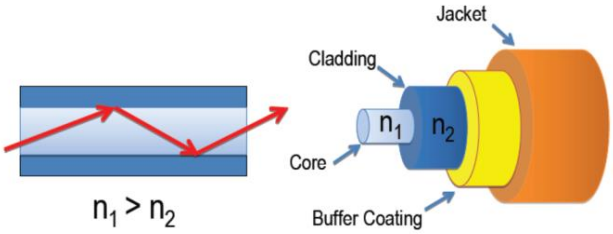

Figure 3.5: Optical fibre schematic (National Instruments, 2011)

The entirety of a fibre optic sensor (FOS) consists of a light source (*e.g.* a laser), the optical fibre (*i.e.* the sensing element), and the detector (*e.g.* a photodetector). The propagating light wave within the core contains the following physical properties: amplitude, intensity, phase, polarization, and frequency. As the optical fibre is either bonded to the surface or embedded within the material (López-Higuera, Cobo, Incera, & Cobo, 2011), any external perturbations will cause a physical change on the fibre that will induce a change to the signal within the fibre. These fluctuations in the signal can be related back to the physical perturbations by analysing the change in spectral shift of the signal (*i.e.* change in amplitude, frequency, and phase).

Based on topology and configuration, a fibre optic sensor can be regarded as being either a single-point, multi-point, or distributed sensor. Single-point sensors have a sensing portion of the fibre located only at the tip. Multi-point fibre optic sensors contain two or more sensing regions along the length of fibre, spaced

anywhere from a few centimeters to meters apart. Distributed fibre optical sensors, as the name suggests, contain virtually innumerable sensing regions along the length of the fibre. In this manner, single-point and multi-point FOSs are analogous to discrete conventional means of instrumentation as they are able to monitor a finite number of regions. The capability of sensing a virtually infinite number of regions along an optical sensor is unique to distributed FOSs and proposes a solution to the limited spatial resolution of conventional instrumentation.

Different fibre optic solutions are available to monitor the strain and temperature along an optical fibre either discretely or in a distributed manner. Discrete optical sensing solutions include:

1. Fabry-Perot interferometers; and,
2. Fibre Bragg gratings (FBG).

Distributed optical sensing solutions use either optical time domain reflectometry (OTDR) or optical frequency domain reflectometry (OFDR) by sending a narrow pulse of light through the optical fibre. There will be a spontaneous back reflected component of this light within the fibre that arises due to three main scatter phenomena (as seen in Figure 3.6):

1. Rayleigh backscatter (Posey, Johnson, & Vohra, 2000);
2. Raman backscatter (Kikuchi, Naito, & Okoshi, 1988); and,
3. Brillouin backscatter (Kurashima, Horiguchi, & Tateda, 1990).

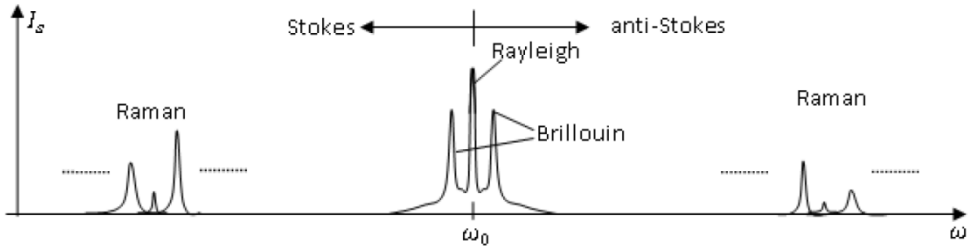

Figure 3.6: Spontaneous scattering spectrum for solids (Bao & Chen, 2012)

All of the available FOS solutions benefit from the inherent long term stability and reliability of the fibre. This means that the sensors do not need to be re-calibrated for long term applications as conventional instrumentations do. Additionally, FOS can survive chemically charged environments, can be installed in tight areas, and can form optical sensors with one optical fibre (Habel & Krebber, 2011). These benefits evidently make FOS the perfect solution for

monitoring longitudinal strain along a bolt. The following sections detail the aforementioned fibre optic sensing solutions.

3.3.1 Fabry-Perot Interferometer

Fabry-Perot interferometers are FOS composed of two parallel mirrors separated by a cavity as seen in Figure 3.7. This cavity (gap) can either be created by a continuous segment of single-mode optical fibre or by an air gap. As light makes its way through the sensor, there are a series of light interferences between the two mirrors. These create a series of peaks in the resulting optical spectrum. The spacing between spectrum peaks varies directly with the spacing between the two mirrors. The fluctuation of the spacing between peaks is directly caused by external perturbations on the fibre. Accordingly this shift in spectrum can be associated with two physical phenomenon – strain and temperature. This method enables the use of one measuring point per sensor. Due to their small size and simplicity Fabry-Perot interferometers are common in medical applications or oil and gas industry as pressure transducers. However, since these function as single-point sensors, their application within rock bolt monitoring would require more than one fibre optic cable to be used along a bolt profile. Although this may be feasible for numerous sensors due to their small size, limitations arise for the data acquisition required as well as the impracticality of having countless cables. As such, this solution is not optimum for monitoring longitudinal strain along a rock bolt.

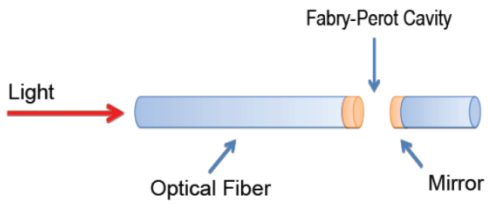

Figure 3.7: Fabry-Perot interferometer composition (National Instruments, 2011)

3.3.2 Fibre Bragg Grating

Fibre Bragg grating sensors are one of the most versatile and commonly used optical sensors since their discovery in 1978 (Hill, Fujii, Derwyn, & Kawasaki, 1978). Common in the telecommunications industry, their inherent capabilities have made them favourable to sensing applications as well. A FBG is a modulation that is created by exposing a section of the fibre to an ultraviolet light. This changes the index of refraction along this region of the fibre, which reflects

portions of the incident light. In this manner, the fibre acts as a dielectric mirror (Venghaus, 2006). These light reflections interfere constructively only for a specific wavelength. This is regarded as the Bragg wavelength. Any changes to the modulation caused by strain or temperature result in a shift of the Bragg wavelength as seen in Figure 3.8. This wavelength has a centered position according to the spacing of the grating structure (A) and the refractive index of the fibre (n_{eff}) as follows:

$$\lambda_{BRAGG} = 2n_{eff}A \tag{3.1}$$

Only this wavelength will be reflected as a Bragg grating is crossed. The remainder of the incident light will pass through. Unique Bragg wavelengths can be assigned per modulation, making multiple sensing regions possible on a single fibre. The wavelength shift ($\Delta\lambda_{bragg}$) is directly correlated to the strain experienced across the grating structure through Equation (3.2) (Micron Optics Inc., 2016):

$$\varepsilon F_g = \frac{\Delta\lambda_{bragg}}{\lambda_{bragg}} \tag{3.2}$$

Here, F_g is the expected gauge factor of the modulation, as specified by the manufacturer. The change in wavelength can be determined through the use of Equation (3.3).

$$\lambda_{bragg} = 2\left(A\frac{dn_{eff}}{dl} + n_{eff}\frac{dA}{dl}\right)\Delta l \tag{3.3}$$

Overall, the number of sensors possible per single optical fibre is limited by the wavelength range of operation for the sensor itself as well as the total available wavelength range of the used optical sensor interrogator (Dakin, 1990). Although FBG FOSs offer a discrete sensing solution, distributed sensing can virtually be achieved by modulating numerous regions along the optical fibre. This creates a quasi-distributed FBG sensor (Barrias, Casas, & Villalba, 2016). This is done by multiplexing numerous modulations on a fibre in the wavelength domain (López-Higuera J. M., 1998). Regardless, the number of reasonably applicable sensing regions is still limited by increased costs, installation limitations due to space, and the sensor length.

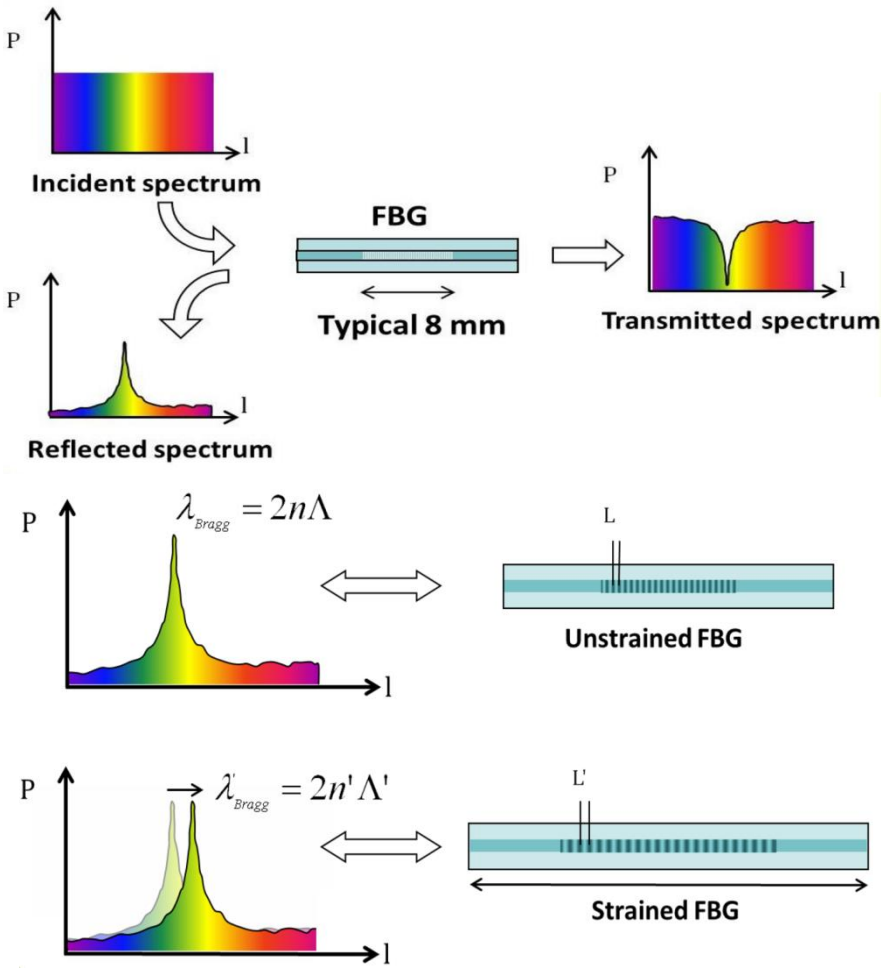

Figure 3.8: Top; FBG structure and ensuing light spectrums. Bottom; Bragg wavelength shift induced by external perturbations (FBGS, 2016)

3.3.3 Raman Distributed Sensing

Raman scattering is a result of a non-linear interaction that occurs as light travels through the silica fibre core. Light scatter occurs as a result of a spontaneous phenomenon that is caused by the incident light stimulating molecular vibrations within the glass core. The change in amplitude of this scattered light is directly related to the temperature changes along the optical fibre. As this

technology is mainly dependent on temperature (Dakin, 1990), its applications are limited and not applicable for the needs of this investigation.

3.3.4 Brillouin Distributed Sensing

Brillouin scatter phenomenon occurs due to acoustic variations in the optical fibre and is induced from the interaction of optical and acoustic waves within (Barnoski, Rourke, Jensen, & Melville, 1977). Acoustic vibrations stimulated within the optical fibre generate a counter propagating wave (*i.e.* a Brillouin scattering wave) that weakens the pulse of the incident light (Barrias, Casas, & Villalba, 2016). Due to energy conservation laws, there exists a frequency shift between the reflected component of light and the incident light. As this shift is intrinsically dependent on the density of the fibre, Brillouin scatter can be used to measure strain and temperature along the length of an optical fibre. Two main techniques make this possible: Brillouin optical time domain reflectometry (BOTDR) and Brillouin optical time domain analysis (BOTDA). The former is based on spontaneous Brillouin scattering. The latter relies on stimulating the Brillouin scattering wave with the use of an additional laser to counter propagate the initial pulsing laser and detect the weak Brillouin scattering signal as seen in Figure 3.9.

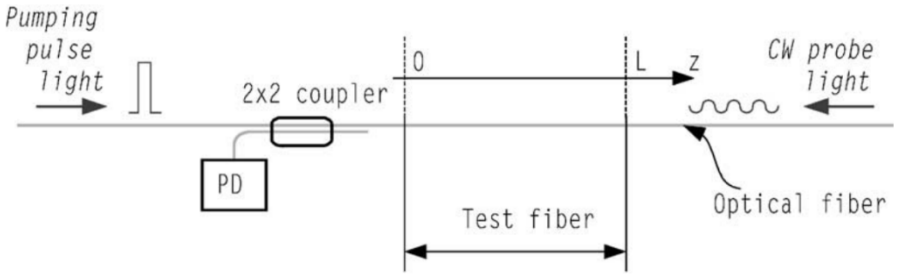

Figure 3.9: BOTDA schematic (Kwon, Baik, Im, & Yu, 2002)

The shift in frequency is caused by a change in acoustic velocity (V_a) due to the change of the density of the fibre. The strain caused by external perturbations and this Brillouin frequency shift can be correlated through Equation (3.4) (Horiguchi & Tateda, 1989):

$$v_b = v_{b0}(1 + C_\varepsilon x \Delta\varepsilon) \tag{3.4}$$

In the equation C_ε is the strain constant – a value that depends on the composition of the fibre materials. The frequency of the scatter is affected by the acoustic velocity under Equation (3.5).

$$v_b = \frac{2n_{eff}V_a}{\lambda} \tag{3.5}$$

Sensors based on stimulated Brillouin scattering are less sensitive to optical losses generated due to manufacturing and installation. Due to this, they are capable of monitoring at longer lengths of up to 10 km (Thévenaz, et al., 1999). The measurement resolution and spatial resolution are however lower than other methods. As such, this is best suited for monitoring more global strain fluctuations over long distances. This method consists of the most used and researched method for the structural health monitoring of civil engineering structures (Barrias, Casas, & Villalba, 2016).

3.3.5 Rayleigh Distributed Optical Sensing (DOS)

The Rayleigh back scattering phenomenon is caused by the density and composition fluctuations created in the fibre during the manufacturing process. These fluctuations create microscopic variations in the index of refraction of the fibre core. As a narrow pulse of light is guided through the fibre, variations in the index of refraction along the optical fibre will back reflect components of the incident light. Unlike previously highlighted techniques, Rayleigh scattering is independent of almost all external physical fields. It is also quasi-elastic in that no energy is transferred to the glass and accordingly there is no difference in the frequencies of the incident and back scattered components of light. This is due to non-propagating density fluctuations within the fibre. For this reason, the techniques used to analyse the scatter signal require high powered lasers as well as long acquisition rates to achieve good resolutions and sensing lengths.

As with Brillouin sensing techniques, Optical Time Domain Reflectometry (OTDR) is used with Rayleigh back scatter by sending a short optical pulse into the fibre. A photo-detector measures the amount of backscatter as the light moves down the fibre. The variability of the refractive index along the optical fibre causes losses to the signal due to Rayleigh scattering. By monitoring these variations in the intensity of the Rayleigh backscatter signal, the spatial variations in the fibre scattering coefficient are detected. If the fibre is in an unaltered state, the back scattered signal decays exponentially with time. Any applied external perturbations onto the fibre will cause a sudden local variation to this signal. In this case, the spatial resolution is regarded as the smallest discernable distance between two scatters. This is governed by Equation (3.6).

$$\Delta z = \frac{c£}{2n} \tag{3.6}$$

The spatial resolution (Δz) is dependent on the speed of light (c), the laser pulse width (£) and the refractive index of the light (n). Correspondingly, to improve the spatial resolution the pulse width needs to be reduced. However doing this will both weaken backscattering signal and increase the noise level of the signal. This makes signal detection cumbersome, especially for longer sensing lengths. To confront these set-backs, Optical Frequency Domain Reflectometry (OFDR) solutions are used to analyse the Rayleigh backscatter. The interference fringes in the back scattered signal are measured and stored as a static reference fibre state in the frequency domain. Any changes in the signal caused by external perturbations are compared to the reference state to deduce the experienced strain. The use of OFDR yields much smaller spatial resolutions as governed by Equation (3.7), where ΔF corresponds to the optical frequency sweep range of a tunable laser source.

$$\Delta z = \frac{c}{2n\Delta F} \tag{3.7}$$

The Optical Distributed Sensor Interrogator (ODiSI-B) unit from Luna innovations provides such a distributed sensing method solution. The ODiSI-B unit splits light from a tunable laser at an optical coupler into a measurement and reference path as seen in Figure 3.10. Another coupler along the measurement path splits the light into the length of optical fibre to be tested and a path to return the back scattered signal. A final coupler recombines the light from the reference and measurement paths. The interference created from the recombination of light gives rise to an interference, which through a Fourier transform, converts the frequency response to the time domain. This allows the signal to be measured at a finite amount of positions along the length of the fibre. The unit stores the backscatter in an unaffected state and determines strain by comparing the strained fibre signature to the original unstrained one. Strain is measured as a shift in the cross-correlation peak ($\Delta\lambda$) as seen in Equation (3.8) (Gifford, Soller, Wolfe , & Froggatt, 2005), where K_ε is a strain calibration constant that is recommended by the manufacturer.

$$\frac{\Delta\lambda}{\lambda} = K_\varepsilon \varepsilon \tag{3.8}$$

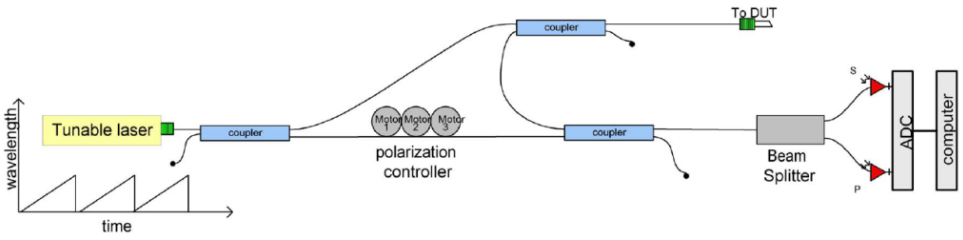

Figure 3.10: ODiSI-B Optical Frequency Domain Reflectometry schematic (Soller, Wolfe, & Froggatt, 2005)

Overall, distributed Rayleigh sensing methods offer small spatial resolutions in comparison to other distributed sensing means. It is relatively insensitive to temperature and has a maximum sensing length of roughly 70 m (Lanticq, et al., 2009).

3.3.6 Optimum FOS for Rock Bolt Monitoring

Table 3-1 summarizes the main capabilities associated with the utilization of the discussed fibre optic sensing solutions.

Table 3-1: Fibre Optical Sensing Technologies Capabilities (as seen in Barrias, 2016; Forbes, 2015)

Sensing Technology	FBG	BOTDA	BOTDR	Rayleigh DOS
Max. sensing length	> 1000 m	200 km	50 km	40 m
Spatial resolution	2 mm	2 cm	1 m	< 1 mm
Accuracy (+/- με)	10	1	1	5
Max. # of measurement points	10-20	> 1000	>1000	> 1000

Although BOTDA is the most common method for SHM in civil engineering applications, the relatively large spatial resolution of the method makes it unfavourable for the purposes of the objectives associated with this research programme. Likewise, BOTDR achieves spatial resolutions that are more suitable for monitoring of global strain fluctuations at longer distances. This is due to the inherent trade-off between sensing length and spatial resolution seen with these fibre optic techniques. Conversely, both FBG and Rayleigh OFDR provide spatial resolutions that vastly improve those achieved with the use of conventional strain gauges on a rock bolt. However, with reference to the spatial resolution of an

FBG sensor, the practically achievable spatial resolution is much closer to 10 cm, since each sensor needs to be individually inscribed onto the optical fibre. This not only limits the spatial resolution but would also affect the cost of the price of each individual sensor.

Accordingly, the only technology suitable that enables the monitoring of the strain profile of the bolt as it is incrementally loaded, is Rayleigh OFDR. Overall, Rayleigh OFDR was used to augment the results attained from conventional instrumentation for this research due to the following reasons:

1. The sensing length (40 m) is sufficient for the purposes of the investigation;
2. The spatial resolution (< 1 mm) makes it possible to capture specific loading mechanisms regardless of where they may materialize;
3. Acceptable operational accuracy (+/- 5 με);
4. Low cost of the fibre means sensors are inexpensive to produce; and,
5. The availability of such an option within the laboratory environment.

The inherent capabilities of Rayleigh DOS make it possible to better capture the complex geomechanical reaction of the support member at the micro-scale. The monitoring of localized strain measurements over relatively short distances is achieved to a high degree of fidelity with this technology. The use of this technology has previously been proven to vastly improve the quality of results in the context of rock bolt monitoring (Forbes, Vlachopoulos, Oke, & Hyett, 2014).

3.4 Relevance to Research

This chapter discussed the conventional methods of monitoring rock bolt support members for both *in situ* and laboratory applications. Conventional instrumentation for pull-out testing includes: strain gauges, LVDTs, load cells, and pressure transducers. The limitations of conventional instrumentation were covered in order to highlight the necessity for a state of the art strain sensing technology. Different FOS technologies that address this gap were then presented. In the end, the Rayleigh DOS method introduced by Hyett, Forbes, & Spearing (2013) and covered to great detail by Forbes (2015), was chosen to be used to monitor the bolt strain profile. The complete implementation of DOS within the constraints of this research programme is covered in further detail in Chapter 5.

4 MATERIALS

4.1 Introduction

In order to properly conduct laboratory pull-out tests, an initial consideration of the materials to be used for the test specimens had to be made. The materials used throughout testing were carefully selected by reviewing previous research endeavours as well as by considering what is most commonly used in civil and mining engineering applications of rock support. This chapter provides a brief overview of this material selection process and identifies all of the materials explored throughout this investigation. Additionally, material properties provided by the manufacturer combined with results from material tests carried out in the RMCC Structures Laboratory were used for testing and analysis throughout this investigation. The ensuing results from these material tests are included in this chapter.

4.2 Pull-Out Test Specimen Materials

The loading scenario used throughout this research program can be seen in Figure 4.1. *In situ*, rock bolts are composed of both a pick up length and an anchor length. However, in laboratory pull-out tests, bolts only have an anchor length. In the figure, the anchor length *in situ* is the section of the bolt from the joint separation up until the toe end of the bolt. This is the section of the bolt which the pull-out tests performed were designed to simulate. Accordingly, all of the specimens utilized throughout the laboratory tests were designed in such a way so as to reproduce the appropriate relationship between the bolt, grout, and rock mass seen *in situ*. The following sections detail, specifically, the materials selected for these three components of the specimens.

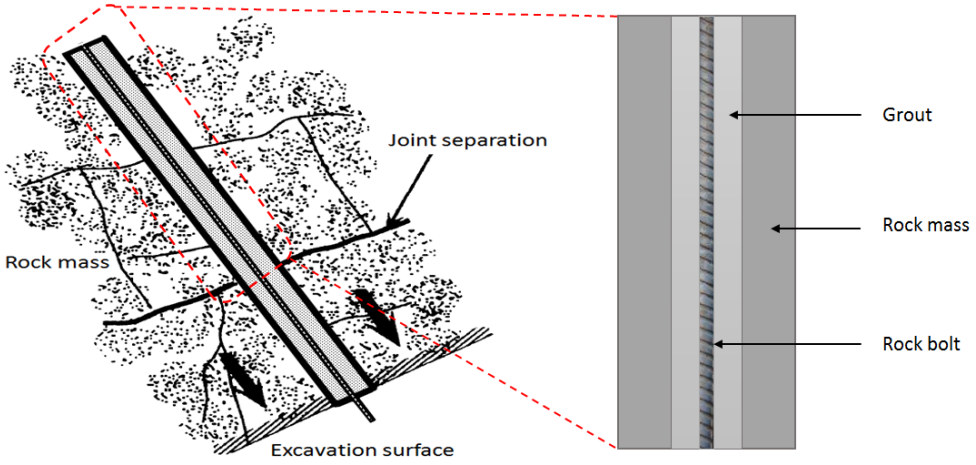

Figure 4.1: Rock bolt loading scenario

4.2.1 Concrete

The rock mass was represented throughout testing with the use of concrete. Concrete was chosen as it accurately portrays the mechanical properties of rock masses *in situ* (Benmokrane, Chennouf, & Mitri, 1995). In addition, concrete can be used to properly reproduce the borehole roughness and radial stiffness that a rock mass tends to provide for a bolt *in situ*. Concrete has been previously proven to provide favourable results in pull-out tests (Benmokrane, Chennouf, & Mitri, 1995; Stillborg, 1984).

Two different batches of concrete were used for the specimens. An initial 25 MPa mix batch was delivered by a ready-mix truck. The second batch of concrete was prepared in the RMCC structures laboratory with the mix ratios seen in Table 4-1. This is akin to a C35 mix of concrete (*i.e.* 35 MPa mix). The cement utilized throughout was Type 10 Portland cement and the aggregate used in the mix was 10 mm course aggregate.

Table 4-1: Concrete Mix Design

Material	Ratio
Portland cement	1
Course aggregate	1.5
Fine aggregate	3
Water	0.55

4.2.2 Cementitious Grout

Two types of grout were used in the pull-out tests. The majority of tests were performed with a cementitious grout since it is commonly used within underground excavation support applications. It is known that the mechanical properties of cement grouts are primarily dependent on the water to cement ratio (w:c) used (by mass). This correlation has been at the centre of many research programs (Benmokrane, Chennouf, & Mitri, 1995; Goris, 1990; Hyett, Bawden, & Reichert, 1992). Generally, it has been proven that as w:c decreases, the mechanical properties of the grout strengthen. This is associated with the fact that any water that is not used during the hydration of the cement evaporates and creates capillary porosity (Kilic, Yasar, & Celik, 2002). This creates a non-homogeneous grout structure that reduces its mechanical properties. As such, for the purposes of this research program, cementitious grout was prepared in the laboratory with a w:c of 0.4. Type 10 Portland cement was used throughout.

4.2.3 Resin Grout

The second type of grout that was used was Ground Lok™ Pourable Resin Grout from Dywidag Systems International (DSI, 2009). This was done in order to analyse the effect that a different grout has on the load transfer mechanisms observed. The manufacturer rated material properties for the resin grout give it a working compressive strength of 78 MPa, and an ultimate compressive strength of 97 MPa (DSI, 2009). In addition to these properties, the manufacturer supplies the pull-out strength chart seen in Figure 4.2.

Figure 4.2: Polyester resin rock bolt pull-out strength chart (modified after DSI, 2009)

4.2.4 Rebar

The tests included as part of this thesis focused primarily on No. 6 Grade 60 rebars from Dywidag Systems International (DSI), as this type of rebar makes up the majority of bolt installations in North America (Li, 2007; Mark, Compton, Oyler, & Dolinar, 2002). The steel rebars have a 19.05 mm diameter, and theoretical yield and tensile strengths of 420 MPa and 620 MPa respectively. The bolt profile was carefully logged since this geometry is directly correlated with the level of interaction along the bolt-grout interface and the development of shear strength along this surface. The salient geometric properties of the rebars include:

A. Rib width;
B. Rib length;
C. Rib spacing; and,
D. Rib height.

The rebar profile can be seen in Figure 4.3 and the individual properties are found in Table 4-2.

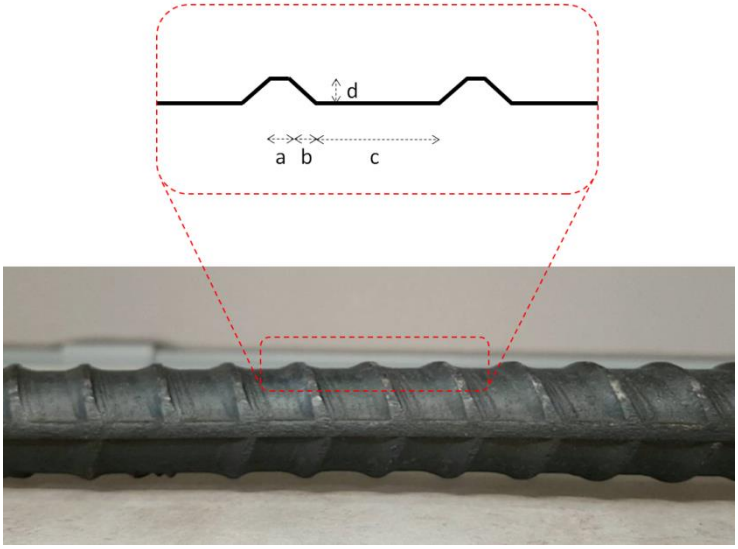

Figure 4.3: No. 6 Grade 60 rebar profile

Table 4-2: No. 6 Grade 60 rebar geometric properties

Property	Rib width [a]	Rib length [b]	Rib spacing [c]	Rib height [d]
Length (mm)	2	3	4	2

4.3 Compression Tests

Uniaxial compression strength (UCS) tests were performed on the concrete, cementitious grout, and resin grout. The tests were performed in accordance to the American Society for Testing and Materials (ASTM) Standard D7012-14 and the Canadian Standards Association (CSA) Standard A23.2-9C. As per the standards, all tests were performed on 100 mm by 200 mm concrete cylinders.

4.3.1 Specimen Preparation

Testing specimens were cast in 100 mm by 200 mm metal cylindrical moulds from the materials covered in Section 4.2. Consolidation of the specimens was achieved using a shaker table to vibrate the cylinders. The specimens were left

to cure in the ambient laboratory environment at the RMCC Structures Laboratory for 28 days. After this, the specimen ends were cut parallel to each other with a grinder and at right angles to the longitudinal axis.

4.3.2 Testing Setup and Procedure

All compression tests were performed on either a 1112 kN Baldwin Universal Testing Machine or a 1350 kN RIEHLE Compression Machine as shown in Figure 4.4. On the RIEHLE Compression Machine, the applied load was read from a dial gauge which has an accuracy of one percent. On the Baldwin Universal Testing Machine, the applied load and displacement were measured directly by the machine and displayed on a conventional computer utilizing the Catman® AP DAQ software. The load was applied to the specimens with a steel bearing block at the bottom base of the setup and a spherically seated steel bearing plate at the top. Additionally, to determine the axial and lateral strains of the concrete cylinders, specimens were outfitted with a steel collar apparatus (*i.e.* a compressometer). The strain both in the axial and lateral directions was derived by dividing the corresponding displacement, as measured by the compressometer, by the gauge length of the instrument.

Figure 4.4: Material Testing Systems. Left; RIEHLE Compression Machine. Right; Baldwin Universal Testing Machine

Compressive tests were done at a loading rate of 1 mm/min. Failure in this case was defined as the point where the specimen continued to experience deformation and could not take on additional load. At this point, the test was complete.

4.3.3 Results

Several compressive tests were performed in order to determine the material properties of the concrete, cementitious grout, and resin grout used in testing. The results of all of the UCS tests can be seen in Table 4-3. The UCS is taken as the maximum load the sample was able to withstand divided by the cross sectional area of the sample.

Table 4-3: Compressive test results for concrete, cementitious grout, and resin grout

Test specimen	Diameter (mm)	Mass (g)	Length (mm)	Max. Load (kN)	UCS (MPa)
C1-a	100.3	3582.1	199.7	161.4	20.4
C1-b	101.0	3401.2	187.0	203.6	25.4
C2-a	101.0	3576.7	191.0	238.7	29.8
C2-b	101.0	3516.1	189.8	237.4	29.6
CG-a	100.8	2911.1	189.7	311.2	39.0
CG-b	100.7	2870.9	187.8	341.5	42.9
RG-a	100.1	2751.1	195.6	105.0	13.3

The first batch of concrete had UCS values close to the expected value of 25 MPa. Likewise, the second batch had UCS values close to the expected value of 35 MPa. The cementitious grout achieved considerably higher values of UCS than did the concrete mixes. Although the concrete and grout shared two of the same materials (*i.e.* water and concrete), the concrete was also made up of aggregate, sand, and a higher w:c. These differences accounted for the lower strength of the concrete. Additionally, the resin grout proved to be the weakest out of all of the materials tested in terms of its' UCS. Lower UCS values were achieved for the resin than the manufacturer specified 97 MPa. This is due to the fact that the ASTM Standard used by the manufacturer to arrive at this value was C578-01, not A23.2-9C. Accordingly, as shown in Figure 4.5, the entire resin sample had not properly cured. The strength of the resin was therefore taken as prescribed by the manufacturer.

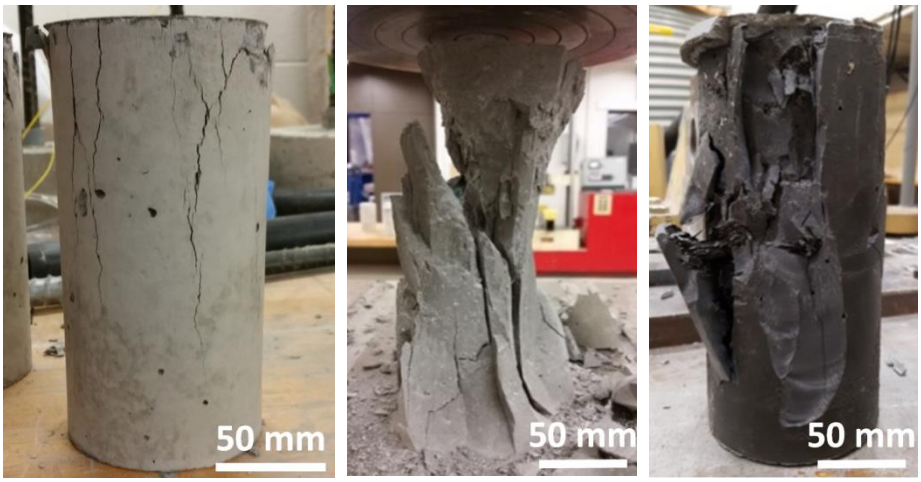

Figure 4.5: Compression test specimens post failure. Left; Concrete. Center; Cementitious grout. Right; Resin grout.

The predominant failure observed for each of the three tested materials can be seen in Figure 4.5. The concrete cylinders failed in a more controlled manner when compared to the failure observed in the cementitious grout and resin grout cylinders. Although the cementitious grout specimens attained higher compressive strength values than the concrete specimens, their failure was governed by a more brittle mechanism.

As mentioned in Section 4.3.2, some of the compressive tests were performed with the use of compressometer. These lateral and axial displacements were used with the gauge length of the compressometer to arrive at values of axial and lateral strain. Figure 4.6 exhibits the stress-strain results for one of the cementitious grout tests. The positive portion of the figure corresponds to the lateral strains experienced by the specimen whereas the negative portion of the graph corresponds to the axial strains. The modulus of elasticity was calculated by taking the average modulus of the linear portion of the axial stress-strain curve. Poisson's ratio was then calculated as the negative slope of the linear portion on the axial curve divided by the slope of the linear portion of the lateral curve. All of the pertinent results for these tests are found compiled in Table 4-4.

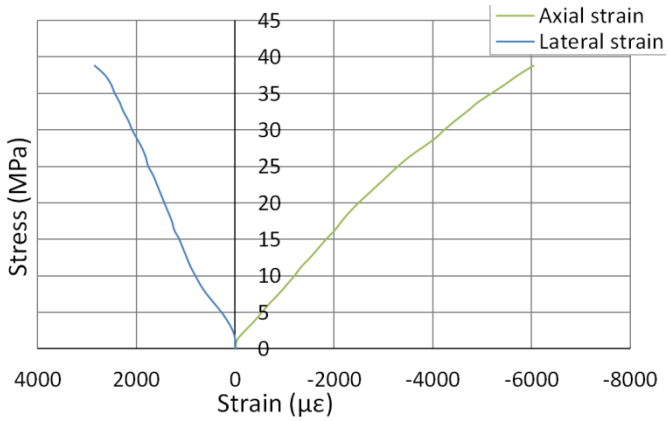

Figure 4.6: Stress-strain results for a cementitious grout UCS test

Table 4-4: Modulus of elasticity and Poisson's ratio results

Test specimen	Diameter (mm)	Mass (g)	Length (mm)	E (MPa)	*v*
Concrete batch 1	100.3	3582.1	199.7	16800	0.24
Concrete batch 2	101.0	3576.7	191.0	15900	0.14
Concrete batch 2	101.0	3516.1	189.8	14300	0.14
Cement grout	100.8	2911.1	189.7	8200	0.14
Resin grout	100.1	2500.1	195.6	2539	-

The modulus of elasticity values attained show that the concrete cylinders had a much stiffer response than both the resin and cementitious grout specimens. Out of the two grouts, the resin grout had the lowest modulus of elasticity. This is again associated with the fact that the grout cylinder did not fully cure. The Poisson's ratio values attained for the concrete and cementitious grouts were within the range of expected values.

4.4 Splitting Tensile Tests

Splitting tensile strength (STS) tests were performed on the concrete and cementitious grout used throughout the testing program. All tests were performed

in accordance to the standards set out in ASTM Standard D3967-08 and CSA A23.2-13C. The tests were done on 100 mm by 200 mm concrete cylinders. The cylinders have the appropriate thickness to diameter ratio (0.5) and had a diameter at least ten times bigger than the largest mineral grain constituent in the materials tested.

4.4.1 Specimen preparation

Testing specimens were prepared in 100 mm by 200 mm metal cylindrical molds from the materials covered in Section 4.2. Immediately after the concrete cylinders were cast, they were consolidated with the use of a shaker table. Over the next 28 days, the specimens were left to cure in the ambient laboratory conditions of the RMCC structures laboratory. After this, specimens were removed from their forms and dimension measurements were taken.

4.4.2 Testing Setup and Procedure

All STS tests were performed on the 1112 kN Baldwin Universal Testing Machine seen in Figure 4.4. The applied load and displacement were measured directly by the machine and displayed on a conventional computer utilizing the Catman® AP DAQ software. Load was applied to the specimen with the use of a machine platen on the bottom and a false steel platen at the top. 2 mm thick plywood cushions were placed in between the machine bearing surfaces and the specimen in order to reduce high stress concentration (as per ASTM D3967-08).

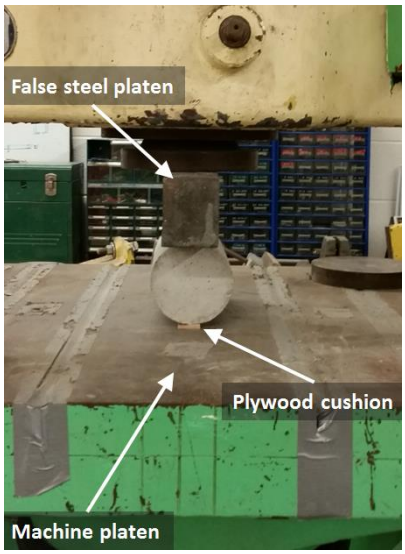

Figure 4.7: STS test specimen setup on Baldwin Universal testing machine

STS tests were performed at a constant loading rate of 1 mm/min. Failure was defined as the point at which the specimen could not take on additional load. At this point, each test was complete.

4.4.3 Results

The overall results of all STS tests can be seen in Table 4-5. The STS of the first batch of concrete was lower than the second batch (roughly 10 % lower). The cementitious grout showed stronger tensile properties than the concrete. However, as with the compressive tests results, the failure results suggested that the grout is a more brittle material than the concrete.

Table 4-5: Splitting tensile test results for concrete, cementitious grout, and resin grout

Material test	Diameter (mm)	Mass (g)	Length (mm)	Max. Load (kN)	STS (MPa)
Concrete batch 1	100.5	3558.0	199.2	82.5	2.6
Concrete batch 1	100.7	3450.2	189.5	90.1	3.0
Concrete batch 2	100.8	3529.6	190.2	95.7	3.2
Concrete batch 2	100.8	3484.7	188.2	110.1	3.7
Cement grout	100.7	2900.3	189.3	54.9	1.8

4.5 Tensile Tests

A series of three (3) tensile tests were performed on a No. 6 Grade 60 rebar. These tests were done to:

1. Ensure that all instrumentation was functioning accordingly;
2. Evaluate any differences observed from the results attained from different instrumentation; and,
3. Validate the material property values for the steel rebar.

The tensile tests were performed in accordance to the ASTM Standard E8/E8M-16a.

4.5.1 Specimen preparation

A No. 6 Grade 60 rebar of 1273 mm length was prepared for the tensile tests. Preparation of the rebar proceeded by instrumenting it with both conventional

strain gauges as well as Rayleigh DOS. The rebar was modified with 2.5 mm by 2.5 mm diametrically opposing grooves along its length in order to accommodate the optical sensing technique as highlighted by Forbes et al. (2014). The modified rebar has a theoretical altered yield and tensile strengths of 117.3 kN and 183.1 kN respectively. The fibre optic sensor used along the rebar was made up of a single mode optical fibre and a terminator and connector end. The fibre was carefully coupled to the steel bars along the grooves with the use of a proprietary metal bonding adhesive. The adhesive was allowed the adequate time to cure prior to testing. This stage of the specimen preparation process can be seen in Figure 4.8.

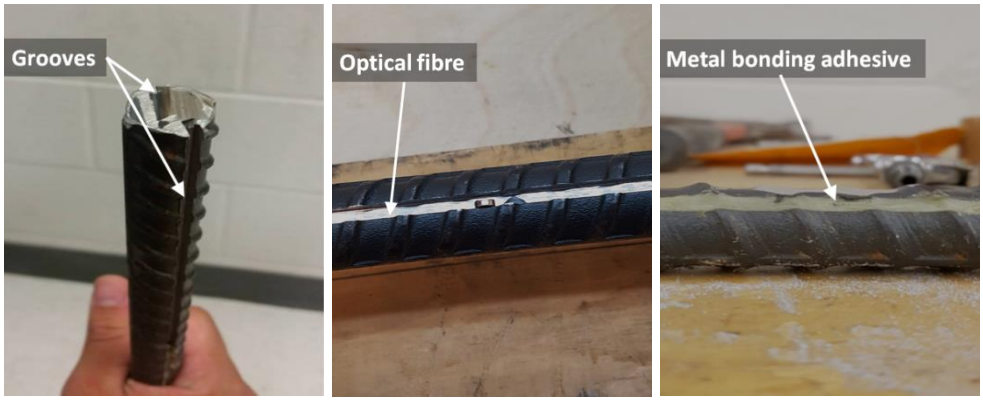

Figure 4.8: Left: Diametrically opposed groves on rebar; Center: FOS within groove; Right: MBA coupling FOS to rebar

After the metal bonding adhesive cured, the steel bars were instrumented with Showa Uniaxial Strain Electrical Resistive Strain Gauges N11-FA-5-120-11 of 3 mm gauge length. The strain gauges were bonded to the steel surface by sanding down the bonding location with the use of a belt sander (Figure 4.9). After this, the bonding surface was cleaned of all possible dirt and particles with the use of a surface contact cleaner. The surface was allowed to dry after which point a Loctite 496 instant adhesive was used alongside an M-200 catalyst to attach the strain gauge to the prepared surface of the rebar. Pressure was applied to the strain gauge for 2 minutes to ensure it was adequately coupled to the surface of the rebar. Carefully following this procedure for each of the strain gauges ensured accurate strain readings throughout the tests. Five (5) strain gauges were bonded to two diametrically opposing sides of the rebar for a total of ten (10) strain gauges.

Figure 4.9: Left: Prepared rebar surface for strain gauge bonding; Center: Protected lead cables on rebar; Right: Prepared concrete surface for strain gauge bonding

The lead cables connecting the strain gauges to the DAQ were carefully lined up on top of the cured metal bonding adhesive within the diametrically opposing grooves on the rebar. The cables and strain gauges were then covered with a flexible adhesive commonly used in dynamic testing projects. This was done in order to protect the leads from breaking within the brittle grout in later tests.

4.5.2 Testing Setup and Procedure

The tests were performed on a 810 MTS outfitted with two 647 MTS hydraulic wedge grips. The fibre was connected to an ODiSI-B unit which transfers the fibre optic data to a conventional desktop through the Luna Innovations ODiSI-B Software 2.0. The strain gauges were connected to an MGC Plus DAQ which communicated with a conventional desktop computer through the Catman® AP DAQ software. Additional parameters of interest were the applied load and the displacement, as were recorded by a 100 mm actuator and 500 kN load cell respectively and recorded by the Catman® AP DAQ software. All tests were done at a loading rate of 0.5 mm/min. Three independent tests were performed on the sample, loading the rebar up to a load of 90 kN. The entire testing setup can be seen in Figure 4.10.

.

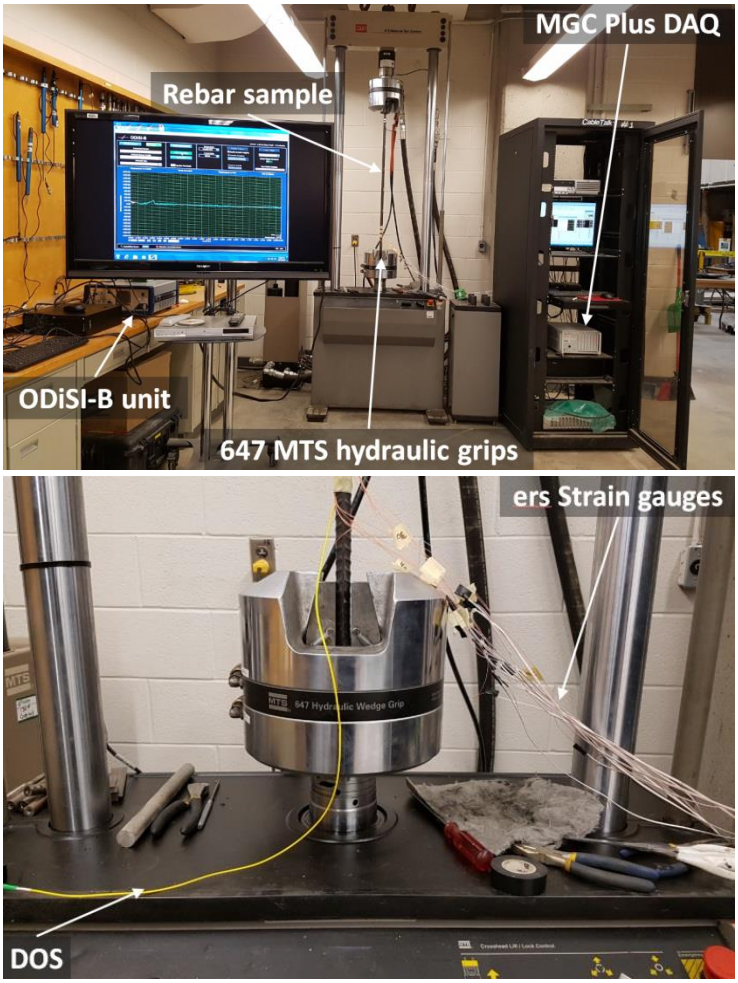

Figure 4.10: Rebar tensile testing setup on 810 MTS. Top; Monitoring program. Bottom; Gripping assembly and strain measuring connections

4.5.3 Results

The Rayleigh DOS, strain gauge, load, and displacement results were used in order to validate the theoretical modulus of elasticity of the rebar. The raw strain profile along both sides of the rebar can be seen in Figure 4.11. The lines in the figure correspond to the strain profile results attained from the DOS whereas the diamonds correspond to the results recorded by the strain gauges.

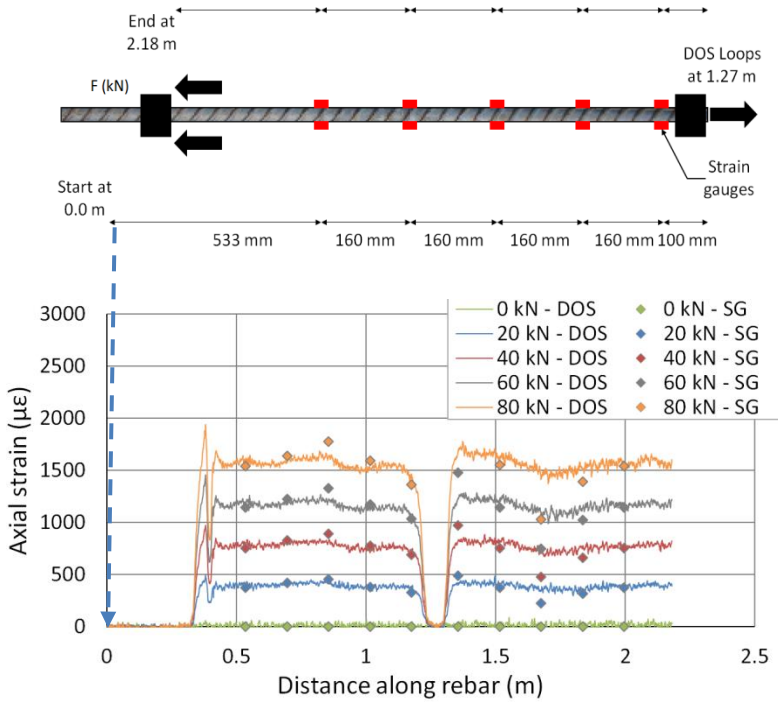

Figure 4.11: Rebar tensile test results for test # 1. Upper; Configuration. Lower; SG and DOS strain profile along rebar length (SG results in diamonds)

As expected, the response of the fibre is relatively symmetrical about the looping point. The strain gauge measurements somewhat reflected the results captured by DOS. However, at the locations where the strain exhibited maximum and minimum values, the strain gauge results seem to diverge from the strain profile of DOS. This can be attributed to the positioning of the instrumentation, as the strain gauges were mounted externally on the rebar whereas the fibre was installed within the diametrically opposing grooves. The fibre alignment is therefore much closer to the neutral axis of the rebar than the strain gauges. Accordingly, even minimal occurrences of bending will have a magnified effect on the strain gauge results. Throughout all of the tensile tests, a small amount of bending was observed as it is virtually impossible to apply a perfectly co-axial (*i.e.* parallel to the bolt alignment) load on the rebar. This is due to both the difficulty in perfectly lining up the bolt and the loading axis, as well as the initial bending of the rebar as loading commences (*i.e.* no rebar is perfectly linear). Bending was removed by averaging the strain along diametrically opposing sides. Figure 4.12 shows the detailed strain profile of the rebar in test # 1. In this manner, the rebar's

strain profile is almost precisely flat and the strain gauge values approach the DOS values to a much higher degree.

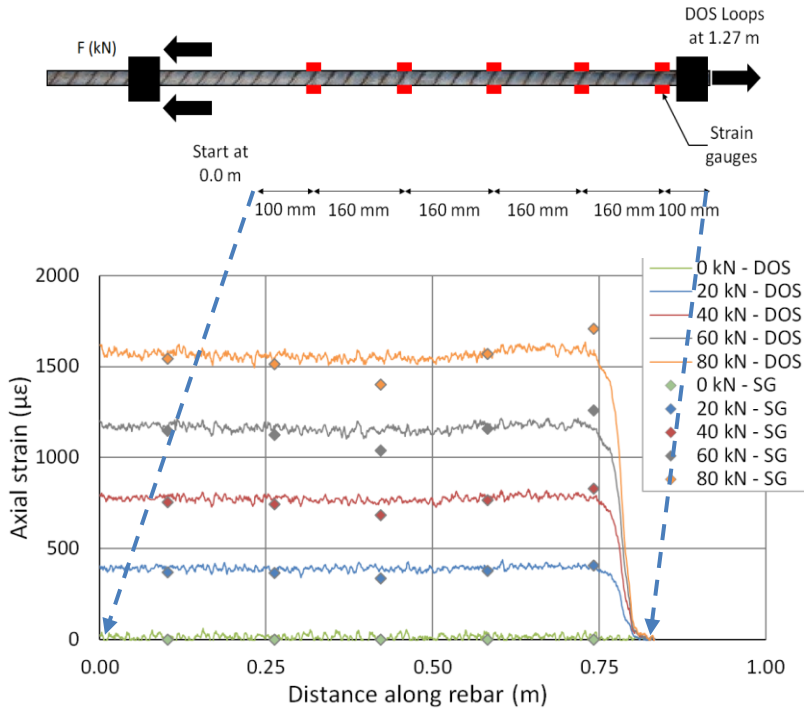

Figure 4.12: SG and DOS strain profile final results for tensile test # 1

A sample of the strain results compiled for test # 1 on the rebar is seen in Table 4-6. The strain results were utilized alongside the applied loading to develop stress-strain profiles for each test. Such results can be seen in Figure 4.13.

Table 4-6: Rebar tensile test results for test # 1

Load (kN)	Axial Displacement (mm)	$\bar{\varepsilon}_{SG}$ (με)	$\bar{\varepsilon}_{DOS}$ (με)	$\bar{\varepsilon}_{THEO}$ (με)	SG % dif.	DOS % dif.
0	0.0	0	13	0	-	-
20	0.5	372	370	358	4	3
40	1.2	755	731	725	4	1
60	1.9	1144	1098	1093	5	0
80	2.8	1547	1475	1460	6	1
60	2.4	1184	1075	1110	7	3
40	1.8	796	712	742	7	4
20	1.2	410	346	374	10	7

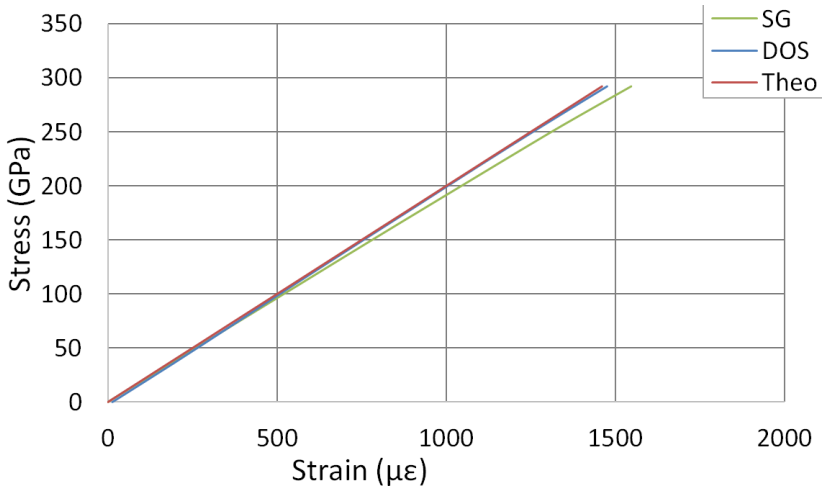

Figure 4.13: Stress-strain profile for rebar tensile test # 1

Both the strain gauges and DOS achieved values for the modulus of elasticity within a good margin of error as seen by the slopes of the lines in Figure 4.13. The overall results for the modulus of elasticity can be found compiled in Table 4-7. The results, as captured by the conventional strain gauges, only varied by roughly 5 percent from the theoretical value of the modulus elasticity of the studied No. 6 Grade 60 rebar. DOS achieved even higher quality results with

negligible differences between theoretical and experimental values of the modulus of elasticity.

Table 4-7: Rebar tensile test results

Test #	1	2	3	Av.	CV (%)
E_{THEO} (GPa)	200.0	200.0	200.0	200.0	-
E_{SG} (GPa)	189.4	190.5	190.4	190.1	0.3
E_{DOS} (GPa)	200.6	200.9	200.7	200.7	0.1
SG % diff.	5.3	4.8	4.8	5.0	-
DOS % diff.	0.3	0.5	0.3	0.4	-

Overall, the tensile tests performed on the rebar achieved all of the objectives outlined at the beginning of Section 4.5. Both the DOS and strain gauge instrumentation were found to be working to a good degree of confidence and the properties of the rebar were validated. The results attained by the DOS technique also proved to be much closer to the expected/theoretical values of the modulus of elasticity of the rebar than the strain gauge results.

4.6 Relevance to Research

This chapter introduced the materials at the center of the laboratory investigation. These four materials are: concrete, cementitious grout, resin grout, and steel reinforced bars. Each material was tested in the RMCC structures laboratory in order to derive basic material properties. The tests included uniaxial compressive strength, splitting tensile strength, and tensile tests. Overall, the material property values attained for all materials to be used within the pull-out testing scheme agreed well with values seen in the literature. These material properties are important as they will be used within the numerical modelling covered in Chapter 6 and in the analysis of results in Chapter 7.

5 LABORATORY TESTING PROGRAM

5.1 Introduction

Extensive laboratory work was carried out at the RMCC Structures Laboratory in order to analyse the response and performance of fully grouted rock bolts through a series of pull-out tests. This chapter covers the procedures followed to prepare all fourteen (14) specimens tested. The development of the pull-out testing rig is covered in detail along with the monitoring program designed to capture the response of the support member. The monitoring program includes all of the instrumentation used along with the ensuing data acquisition management. The pull-out test specimens were subjected to axial loads under slow displacement controlled loading conditions. Complete details of the testing program and procedure is also described.

5.2 Preparation of Pull-out Test Specimens

No. 6 Grade 60 rebars of varying lengths were prepared by instrumenting them with Rayleigh DOS in order to conduct the pull-out tests. This was done according to the methodology outlined by Forbes (2015). All steel bars were modified with 2.5 mm by 2.5 mm diametrically opposing grooves as shown in Figure 5.1. This corresponds to an overall reduction of the cross sectional area of the rebar of 4 percent. These slots provided more than enough space for the application of the optical fibre. The modified rebars have a theoretical altered yield and tensile strengths of 117.3 kN and 183.1 kN respectively.

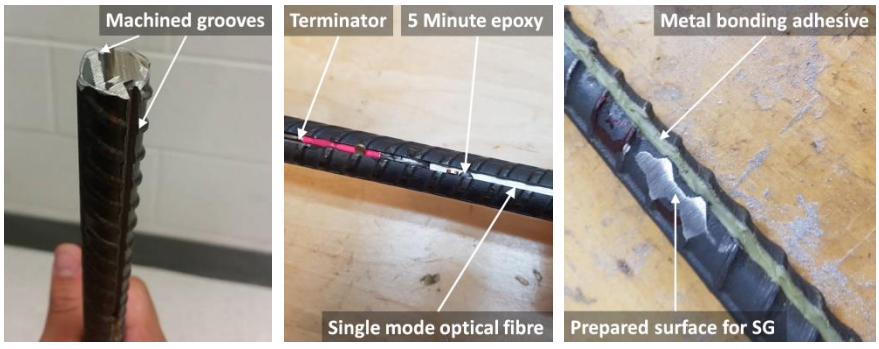

Figure 5.1: Left; Machined grooves on No. 6 Grade 60 rebar. Center; Fibre alignment in machined grooves. Right; Encapsulated rebar grooves

Prior to coupling the fibre optic sensor to the surface of the steel bar, the sensor had to be prepared. The sensors were made up of a single mode optical fibre, a terminator end, and a connector end. All sensors were composed of a Corning SMF 28e+ single mode optical fibre. The fibre was installed as a bare optical fibre (*i.e.* with a core, cladding, and buffer layer) in order to ensure optimum coupling between the steel surface and the fibre itself. A lucent connector (LC) was used in order to connect the fibre optic sensor to the Luna ODiSI-B unit. This was done by cutting optical patch cords to the desired length, and splicing them with the single mode optical fibre. Both of these components can be seen in Figure 5.2. The SMF 28e+ fibre was spliced to the optical patch cords by using an INNO Instrument View 5 Fusion Splicer and an optical cleaver in order to cut the optical fibre for alignment.

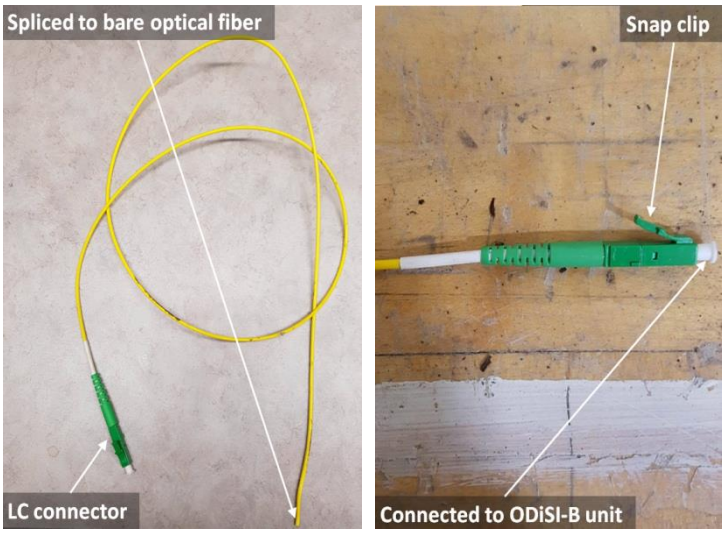

Figure 5.2: Left; Optical patch cord. Right; LC connector

Once the optical sensor was ready to be coupled to the steel bar, the machined grooves had to be properly prepared for instrumentation. This proceeded by surface abrading the grooves with 220 grit sandpaper and cleaning them with acetone. The fibre was then placed within the prepared grooves. Using a 5 minute epoxy resin, slight tension was applied to the fibre in order to enable it to measure any compression changes (as seen in Figure 5.1). The sensor was looped at the toe end of the rebar through a machined out slot. This looped section of the fibre was additionally protected with the use of a heat shrink in order to provide rigidity to the loop. The fibre within the heat shrink was free to move such that there was no transfer of load along this region.

Once the optical sensor was positioned in the machined grooves, the precise location of the fibre along the alignment of the rebar was carefully logged according to the placement of the fibre along the grooves as seen in Figure 5.3. The compiled sensor specifications (as defined in the figure) can be found in Table 5-1.

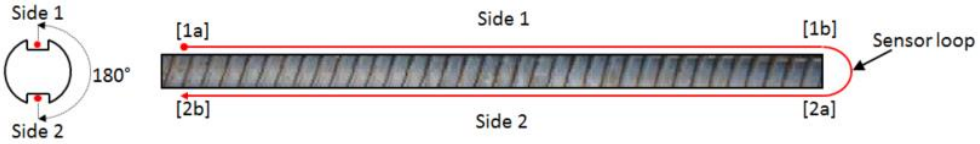

Figure 5.3: Fibre optic sensor configuration

Table 5-1: Fibre optic sensor specifications

Sensor ID #	Rebar length (mm)	1a (m)	1b (m)	2a (m)	2b (m)
1	923	0.000	0.960	1.380	2.290
2	878	0.000	1.030	2.340	1.360
3	960	0.040	0.220	End	0.400
4	960	0.130	0.410	End	0.590
5	933	0.800	0.980	End	1.120
6	950	0.135	0.818	End	1.012
7	945	0.110	0.375	0.720	0.445
8	950	0.085	0.615	1.218	0.688
9	1370	0.188	1.218	2.420	1.390
10	1280	0.340	1.350	2.440	1.430
11	860	0.170	0.395	0.562	0.784
12	860	0.135	0.265	0.440	0.570
13	950	0.145	0.812	1.650	0.984
14	1220	0.450	1.220	2.080	1.315

The grooves were completely encapsulated with the use of a proprietary metal bonding adhesive. This was carefully done in order to keep the adhesive from protruding past the rebar groove height, since this could adversely affect the response of the rebar. An example of an encapsulated rebar can be seen in Figure 5.1.

The test specimens were made out of 200 mm diameter concrete cylinders in order to simulate adequately the behaviour of the rock mass confinement on the grout and bolt *in situ*. Two separate batches of concrete, as covered in Section 4.2.1, were poured into 200 mm diameter Sonotubes. Different length concrete cylinders were cast in order to test specimens of different embedment lengths. The smallest concrete cylinder measured 100 mm, whereas the largest cylinder measured 1 m. The concrete cylinders were allowed a minimum of 28 days to cure in order to allow their optimum strength to develop (as per ASTM C192/192M – 16a).

Once the concrete cylinders cured, the Sonotube form was removed and the pre-cast boreholes in the concrete cylinders were roughened and rifled with the use of a rotary and percussive drill (with the exception of two specimens). The instrumented rebars were then grouted into the pre-cast boreholes in the concrete cylinders with the use of either a cementitious or a resin grout (as covered in Section 4.2). The cementitious grout was allowed an additional 28 days to cure prior to any testing taking place. On the other hand, the resin grout developed its strength over a much faster time – roughly 4 hours – as reported by the manufacturer (DSI, 2009). The pertinent specimen geometry can be seen in Figure 5.4, where A is the rebar length extending past the top of the concrete cylinder, B is the length of the concrete cylinder, and C is the length of rebar extending past the bottom of the cylinder. Details on the dimensions of all fifteen pull-out test specimens can be found in Table 5-2.

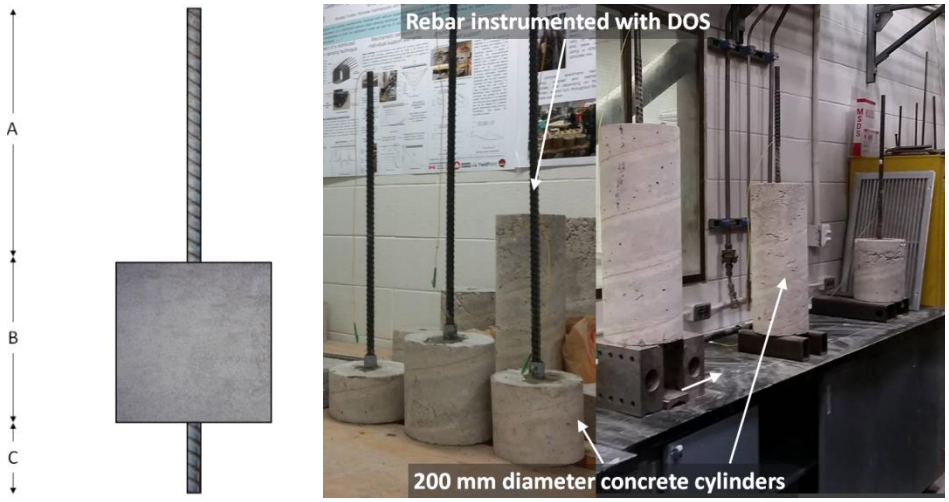

Figure 5.4: Pull-out test specimens

Table 5-2: Pull-out test specimen dimensions

Specimen	A (mm)	B (mm)	C (mm)
b	520	218	140
c	527	157	64
d	163	565	120
e	596	274	45
f	386	513	53
g	564	1005	0
h	295	1080	0
i	630	153	81
j	327	525	67
k	672	105	86
l	732	118	79
m	444	233	69
n	351	515	85
o	402	719	101

5.3 Pull-out Test Rig

Previous pull-out laboratory experimentations have used a variety of testing rig to hold the test specimens in place. The design of a test rig for this research began by analysing previously used testing rig. In this manner, the successes and failures of previous testing rig were incorporated in order to develop a test rigs adequate for the objectives of the thesis as outlined in Chapter 1.

5.3.1 Previous Pull-out Test Rig

The first testing setup popularly known for pull-out testing was the split-pull testing rig as used in tests performed by Fuller and Cox (1975). A split-pull testing rig is seen in Figure 5.5. Steel pipes were used to represent the rock mass surrounding the bolt and grout, providing confinement. A material testing system (MTS) was used to hold the specimen in place and apply pull-rate controlled loading. Although relatively good results were acquired with this setup, the gripping assembly provided extra confinement to the system at the grips, adversely affecting the quality of results. Additionally, higher peak loads were attained than those seen in similar testing conditions in the field. This was mainly attributed to the prevention of rotation of the cable bolts, but also to the high confinement that the steel pipes provided to the grout and bolt. Using a variation of this setup, Goris (1990) was able to perform a set of tests where the behaviour of the system was represented by a load displacement curve. However, these results were seen to not be in accordance with the *in situ* behaviour of the bolts.

Overall, this split-pull testing rig provided valuable results on the behaviour of bolts (Fuller & Cox, 1975; Goris, 1990). To improve upon this setup, a split-push rig as seen in Figure 5.5 was designed by Reichert (1991). In this setup, the grout column and pipe arrangement are pushed off from the bolt. This setup was successfully utilized to study the effect of radial confinement and the behaviour of different sorts of bolts (Hyett, Bawden, & Reichert, 1992).

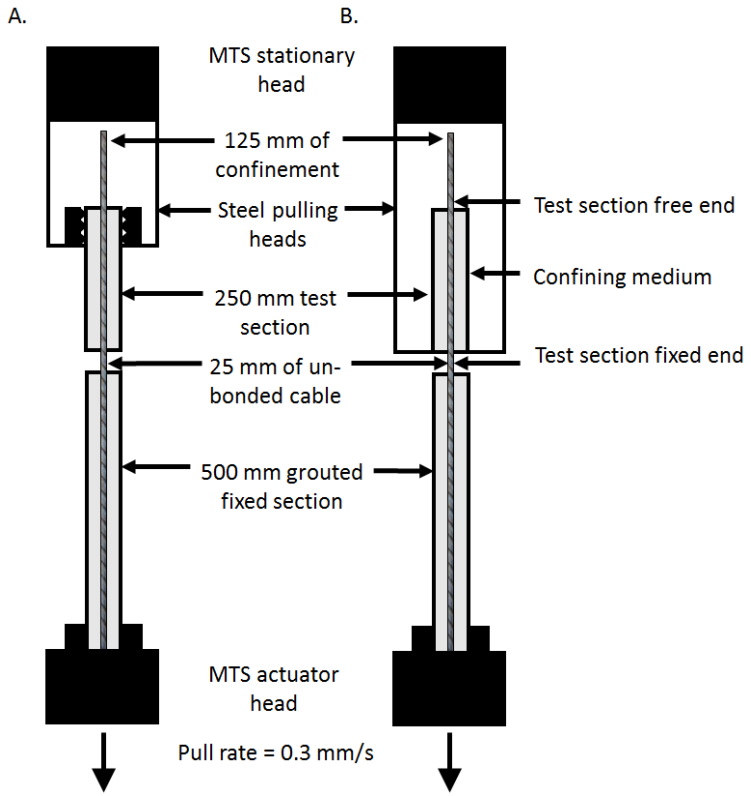

Figure 5.5: A; Split-pull test rig. B; Split-push testing rig (modified after Hyett, Bawden, & Reichart, 1992)

Split-pull/push testing setups were based on constant stiffness conditions provided by the material surrounding the bolt and grout. Accordingly in order to study constant normal pressure conditions, a Modified Hoek Cell (MHC) testing rig (Figure 5.6) was used. A constant radial pressure was applied to the outer surface area of the grout with the use of a MHC. By integrating a MHC within the split-push test rig, the effect of confining pressure and grout composition on the performance of bolts was further studied (Hyett, Bawden, Macsporran, & Moosavi, 1995).

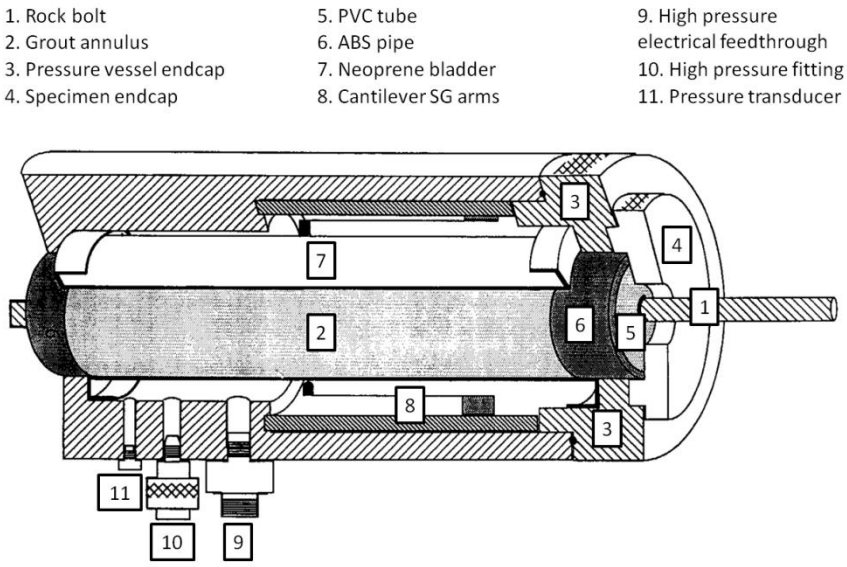

Figure 5.6: Modified Hoek cell testing rig (modified after Hyett, Bawden, Macsporran, & Moosavi, 1995)

In 1984, Stillborg used a different approach to test bolts under axial loading conditions. Concrete blocks were used to simulate the rock mass and provide confinement to the grout and bolt (Stillborg, 1984). In 1992, Benmokrane used a similar setup, by using concrete cylinders with a 200 mm diameter to simulate rock mass conditions. These concrete cylinders were used within a MTS, as shown in Figure 5.7. This testing setup had the following advantages: the blocks were believed to more closely model the properties of a rock mass, the blocks better represented the borehole roughness, and the blocks better represented the radial stiffness provided by a rock mass *in situ*.

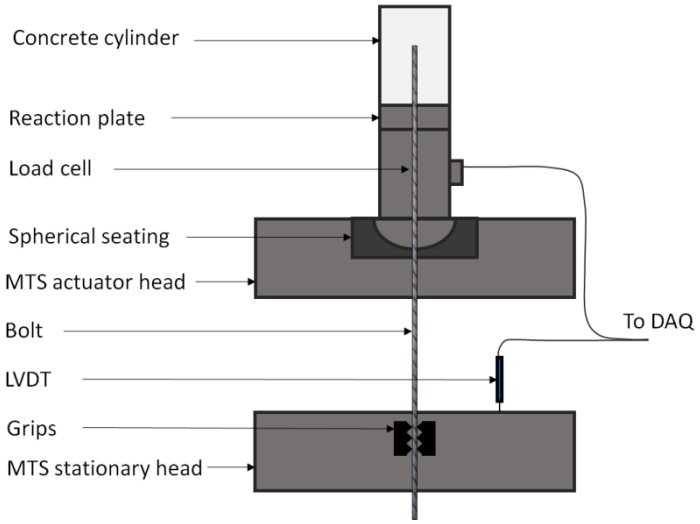

Figure 5.7: Concrete cylinder testing rig (modified after Benmokrane, Chennouf, & Mitri, 1995)

A final variation of pull-out testing rigs can be seen in Figure 5.8 in the form of laboratory short encapsulation performance test (SEPT). In this setup a thick walled steel cylinder is used in order to provide confining pressure to a sandstone core (Thomas, 2013). The bolt is then grouted into the sandstone core.

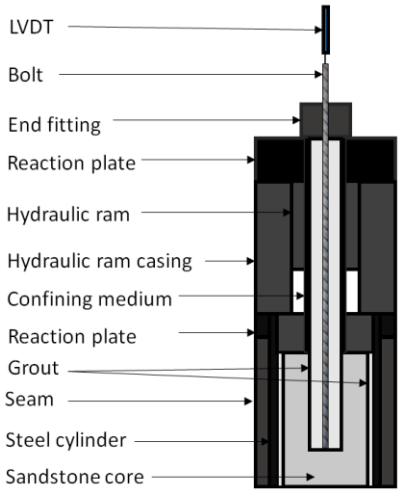

Figure 5.8: Laboratory SEPT rig (modified after Thomas, 2013)

5.3.2 Limitations of previous testing schemes

Previous laboratory investigations used a variation of one of the testing rigs highlighted herein. The most pressing issues and limitations associated with previous testing rigs can be summarized as:

1. Improper representation of the radial confinement present on a rock mass *in situ*;

2. Inability to simulate the interaction between the grout and rock;

3. Lack of control in loading of specimens due to used loading method (*e.g.* a hydraulic hand pump); and,

4. Difficulty in quantifying the effect that individual components in overly complex testing rigs may have on results.

5.3.3 Pull-out Test Rig of this Research Program

A schematic of the test rig designed for the purposes of the research at hand can be seen in Figure 5.9.

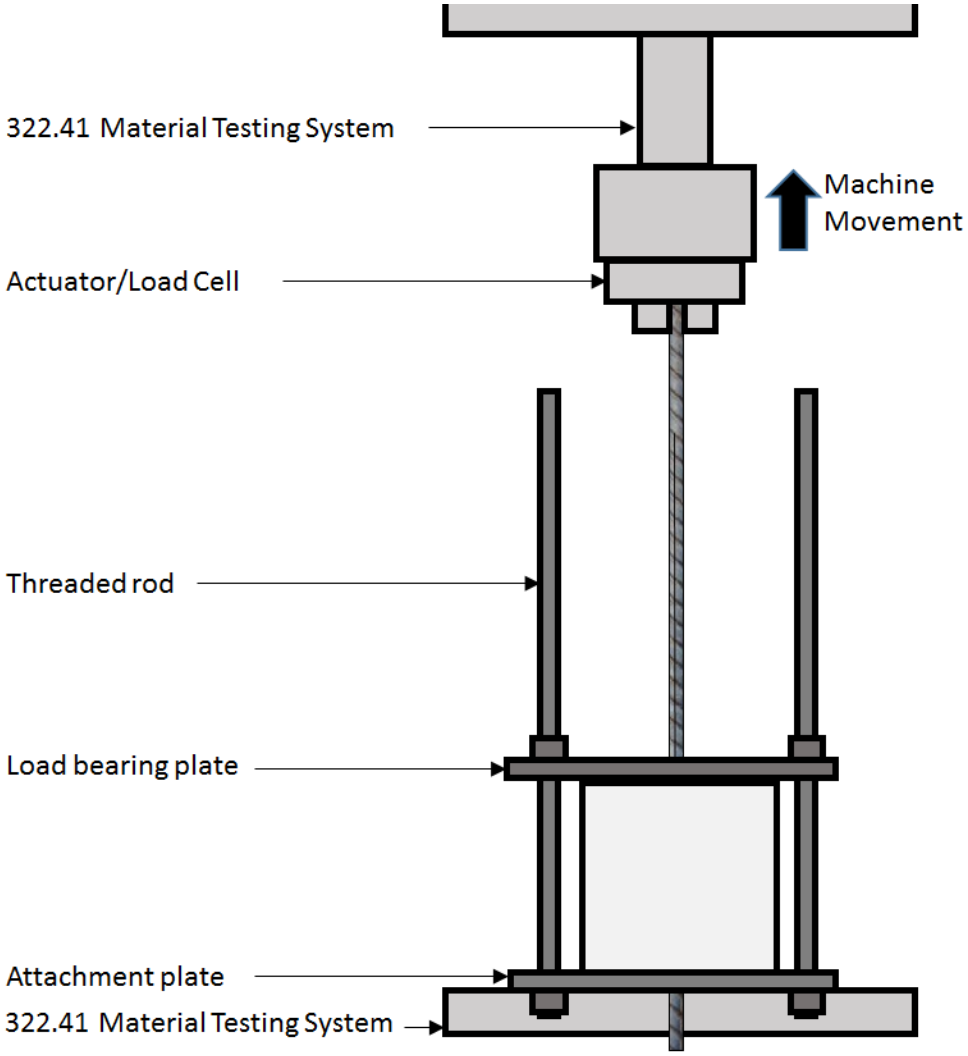

Figure 5.9: Pull-out test rig schematic

A 322.41 Material Testing System (MTS) was outfitted with an arrangement of two 1-inch (25.4 mm) steel plates and two 1-inch (25.4 mm) threaded rods in order to fix the test specimens in place. A steel plate is attached to the workbench of the MTS with the use of four 1-inch (25.4 mm) T-nuts and four ¾-inch (19 mm) 4-inch (101.2 mm) long bolts (Figure 5.10). This steel pate is called the attachment steel plate. The two threaded rods are adhered to the fixed attachment plate by screwing them into a nut between the MTS workbench and plate (the nut was welded to the bottom of the attachment plate). A second steel plate is used alongside two additional nuts to both fix the test specimen in place and bear all applied loads (*i.e.* the load bearing plate). By using this setup, expected loading conditions witnessed *in situ* (Figure 2.13) were adequately simulated.

Figure 5.10: Left: T-nut in MTS T-slot platen. Right: Fixed attachment steel plate

The entirety of the test rig can be seen in Figure 5.11. Compared to some previous test setups, this one contains minimal components. This means that there are fewer variables that could affect the accuracy of the results. The limiting element in this test rig is the collective capacity of the threaded rods. Individually, the threaded rods had a yield and tensile strength of 126 kN and 203 kN respectively. The collective yield and tensile strengths of the rig are therefore 250 kN and 405 kN respectively. Since the tensile strength of the tested rebar was lower than the yield strength of the test rig, loading was successfully kept within the working range of this test setup (*i.e.* $F < 250$ kN).

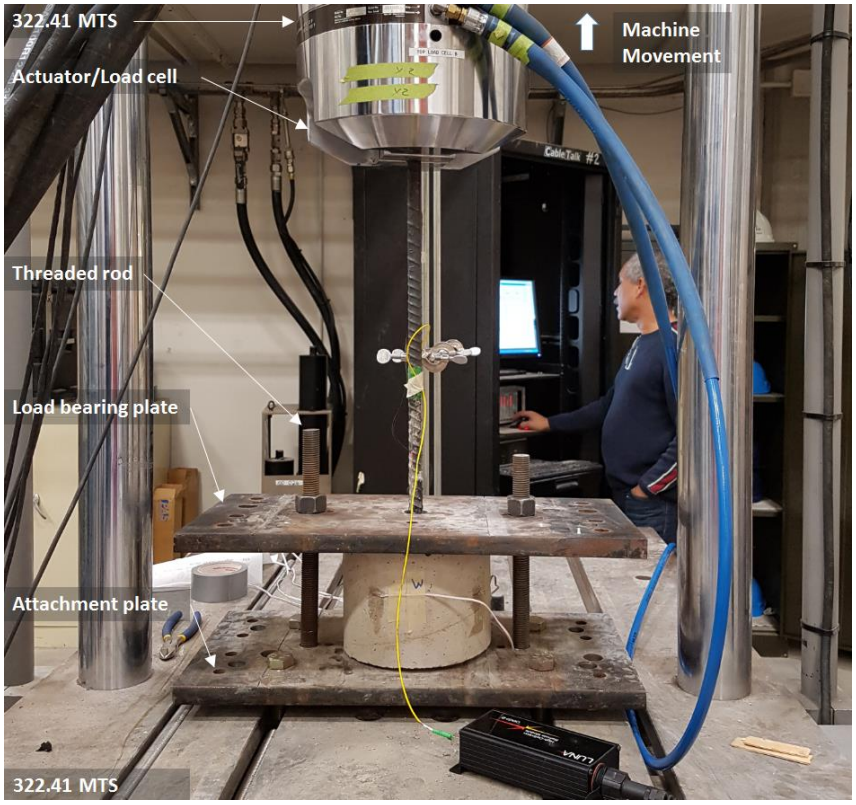

Figure 5.11: Pull-out test rig with specimen at RMCC Structures Laboratory

5.4 Pull-out Test Monitoring Program

For this research, the 322.41 MTS was used alongside a 500 kN load cell, a 250 mm actuator, and a MTS 647 Hydraulic Wedge (500 kN capacity). This allowed for an axial load to be applied in a controlled manner throughout testing, and offered an adequate loading range for the tests performed. The use of the MTS in this manner offered vast improvements over previous tests whereby a manual hydraulic pump was used in order to apply load.

Calibration for all used instrumentation was performed prior to testing. The instruments used in the testing were:

1. 500 kN Load cell;
2. 250 mm actuator;
3. 150 mm LVDT (*i.e.* top LVDT);

4. 250 mm LVDT (*i.e.* bottom LVDT);
5. Strain gauges; and
6. Rayleigh DOS Analyzer.

The instrumentation suite is shown in Figure 5.12 below.

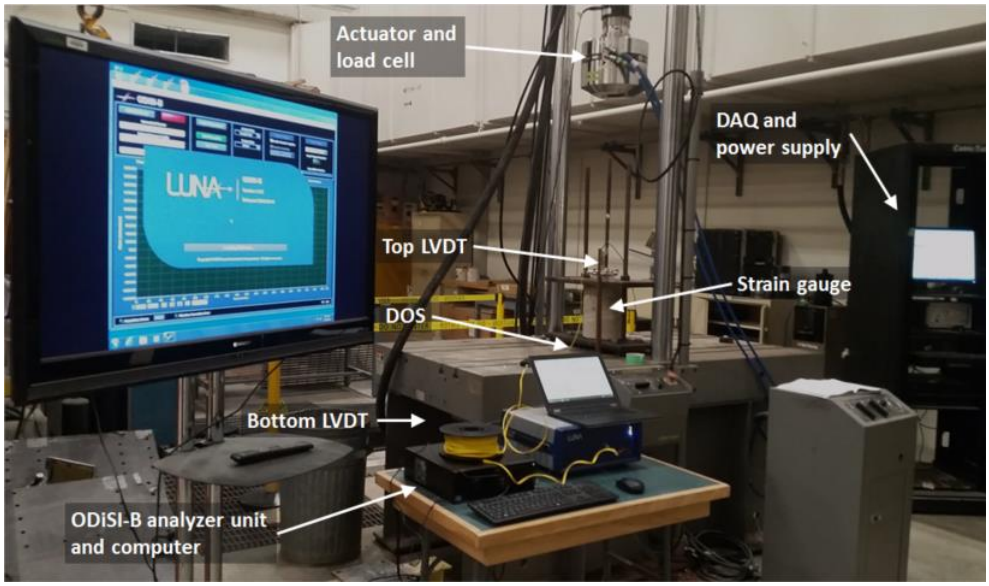

Figure 5.12: Monitoring program – Specimen Pull-out Testing

5.4.1 Actuator and Load Cell

The 500 kN load cell and 250 mm actuator measured the applied load and displacement directly. Output from the actuator is analogous to the applied axial displacement at top portion of the rebar. This measurement can be used alongside the load recorded by the load cell to characterize the load displacement behaviour of specimens. These instruments are calibrated on a scheduled basis in order to ensure accurate readings throughout.

5.4.2 Linear Variable Differential Transformers (LVDTs)

Two LVDTs were used throughout testing. The top LVDT was a Penny & Giles SLS190/150/L/50 with a mechanical stroke of 154 mm. The LVDT is rated by the manufacturer to have a virtually infinite resolution and hysteresis of 0.01 mm. This LVDT was setup to record any linear displacements that the load bearing plate experienced throughout the entire test sequence. This was done in an

attempt to measure any shifting that the testing rig may have experienced during testing. Accordingly, as seen in Figure 5.13, this LVDT was setup independently from the rig.

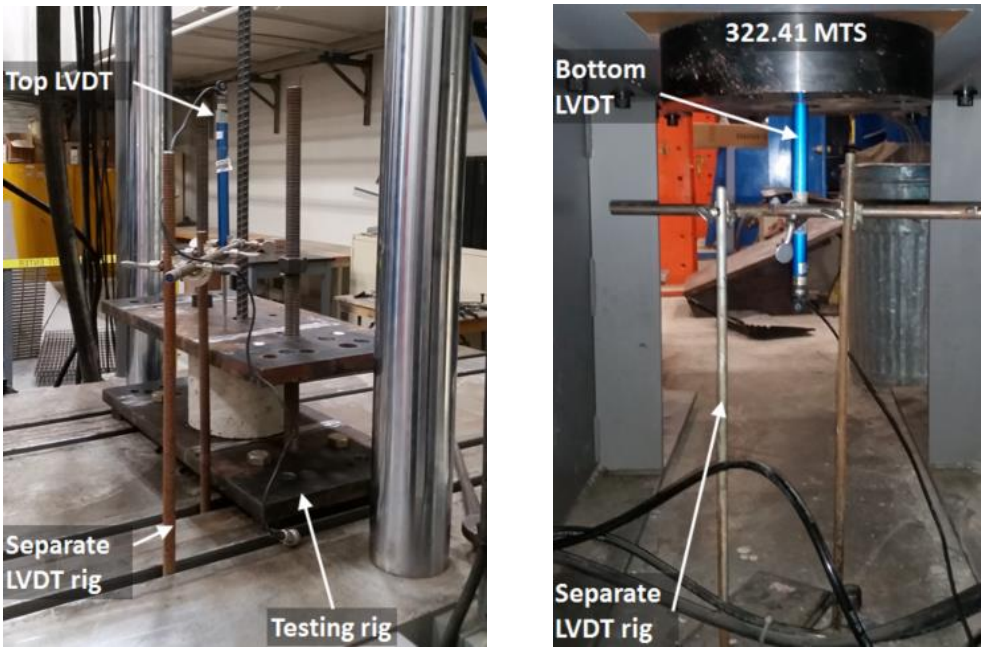

Figure 5.13: Left: Top LVDT setup; Right: Bottom LVDT setup

A second LVDT was coupled to the portion of the bolt that extends past the end of the concrete cylinder. The LVDT used here was a Penny & Giles SLS190/250/L/50 with a mechanical stroke of 254 mm. The LVDT is rated by the manufacturer to have an infinite resolution and hysteresis of 0.01 mm. This end of the bolt is placed within a through-hole in the MTS workbench. The LVDT is coupled with the toe end of the bolt as seen in Figure 5.13. This setup made it possible to monitor any movement at the toe end of the bolt.

Calibration for the LVDTs proceeded by using the pedestal micrometer calibration setup seen in Figure 5.14. The voltage generated by the LVDT was read at different displacements. As the LVDT behaved linearly throughout its working range, these displacements ranged from 0.0 mm to 10.0 mm. The points were correlated to appropriate linear displacement readings as measured by the pedestal micrometer. These points were logged into the Catman® AP DAQ software. To double check the accuracy of the LVDTs, once they were keyed into the DAQ

software, ASTM calibration blocks were used to assess the repeatability and accuracy of each individual LVDT.

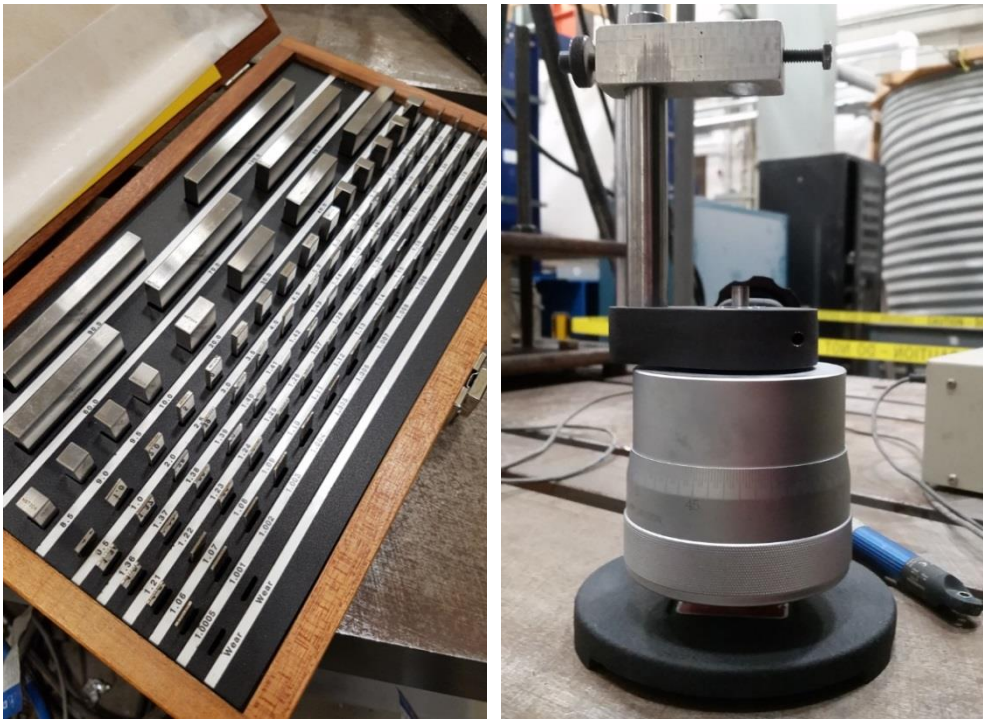

Figure 5.14: Left: Calibration blocks; Right: Pedestal micrometer used to calibrate the LVDTs

5.4.3 Strain Gauges

Showa Uniaxial strain electrical resistive strain gauges N11-FA-5-120-11 of 3 mm gauge length were coupled to the outside surface of the concrete cylinders (Figure 5.15). The strain gauges were centred along the embedded section of the bolt and perpendicular to the direction of applied load. A minimum of two strain gauges were used with all specimens – up to a maximum of four on some specimens. They were spaced equally around the circumference of the concrete cylinders. These strain gauges monitored the circumferential strain experienced by the concrete cylinder as the bolt was incrementally pulled out.

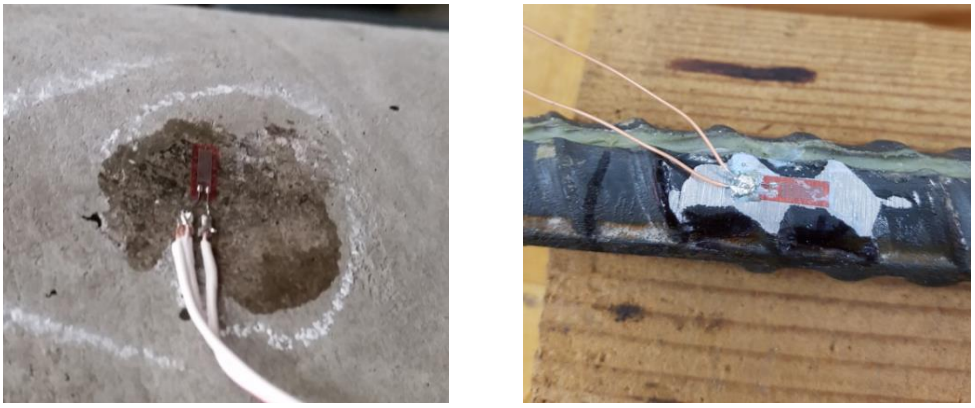

Figure 5.15: Left: Strain gauge mounted on concrete cylinder; Right: Strain gauge mounted on a bolt

Additionally, the rebar instrumented for the tensile tests (Chapter 4) used these 3 mm gauge length strain gauges. This rebar was used in a series of tests as a comparison and redundancy check of the results attained from the Rayleigh DOS. The strain gauges were mounted externally and lined up axially with the vector of applied load (Figure 5.15). Prior to testing, the resistance of all strain gauges was checked with the use of an ohmmeter. More details on the proper installation procedure for these strain gauges can be found in Section 4.5.1.

5.4.4 Distributed Optical Sensing (DOS)

An integral part of this research was the fibre optic sensing technology used to measure the axial deformation of the bolt. Rayleigh DOS was utilized to instrument all tested rock bolts (Section 5.2). This allowed the monitoring of strain virtually continuously along the alignment of tested rebars (Figure 5.16). Strain was captured at 0.625 mm intervals along the steel bar at an accuracy of 5 με.

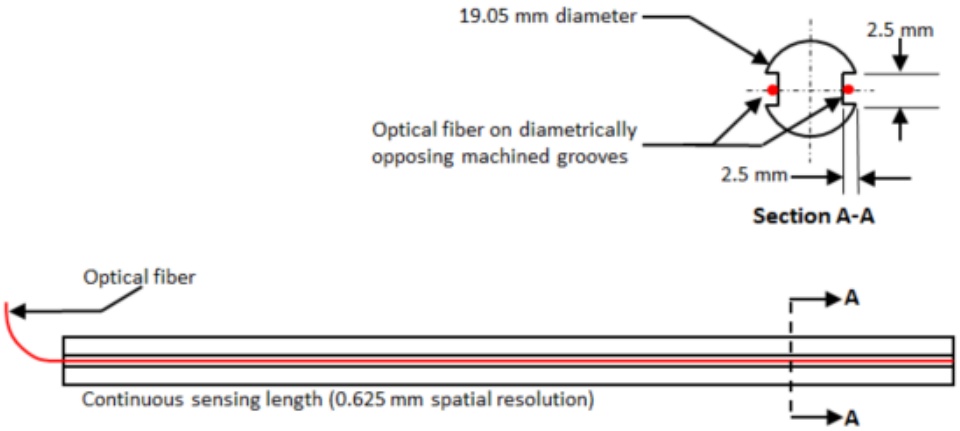

Figure 5.16: Instrumentation of bolts using DOS

5.4.5 Data Acquisition

To meet the transducer requirements of the instrumentation, two separate data acquisition systems (DAQ) were used. The optical fibre required an optical distributed sensor interrogator (ODiSI-B) unit whereas the rest of the instrumentation used the MGC Plus DAQ seen in Figure 5.17. The ODiSI-B unit uses manufacturer provided software from Luna Innovations and is capable of recording hundreds of sensing locations per meter on a single optical fibre up to a rate of 250 Hz. The maximum sensing range of the unit is 50 m and it is capable of measuring strains of upwards of 30,000 με (Luna Innovations Inc., 2016). The MGC Plus DAQ on the other hand is a very powerful DAQ that uses different electronic cards to allow connections of various different transducers. The LVDTs are connected to the back of the unit utilizing an AP 801 card that is capable of reading voltage changes from 8 separate transducers. The SGB1-8 electronic card illustrated in Figure 5.17 was used to connect the strain gauges to the DAQ. The MGC Plus communicates with a conventional desktop computer utilizing Catman® AP software. This software has an intuitive interface that made the calibration and setup of all instrumentation easy and efficient. All instruments were setup to record their respective parameters at a rate of 1 Hz.

Figure 5.17: Left: MGC Plus DAQ; Right: SGB1-8 card

5.5 Pull-out Test Program and Procedure

Testing proceeded by loading the specimens under displacement controlled conditions at a rate of 1 mm/min. Displacement controlled testing was selected over load controlled testing as it allowed controlled loading to continue past the point where initial non-critical failure occurred. Overall, two different testing groups were tested in the laboratory experimentation. A total of fifteen different tests were performed on a total set of fourteen specimens. For all tests, the rebar and grout extended the entire length of the borehole. In this manner, the specimen length was designed to be synonymous with the embedment length of all specimens.

5.5.1 Test Group A

The first series of tests were performed on samples with embedment lengths less than 500 mm. Loading progressed by applying load onto the samples past irreversible failure in order to capture the post-failure response of the support member. These tests focused specifically on analysing the response of the support member in the scenario where the bolt-grout interface was expected to fail. It is important to note that two of specimens prepared for these tests had borehole

annuli that were not properly roughened in order to analyse the effect that this would have on loading.

Table 5-3: Testing outline for group A

Test	DOS Sensor	Specimen	Specimen Length (mm)	Borehole Diameter (mm)	Borehole Prepared	Grout
1	012	l	100	31	Yes	C
2	011	m	200			
3	012	K	100			R
4	011	I	150	41		
5	007	e	250			C
6	002	b	200	31	No	
7	005	c	100			

Note: C = Cement-based grout. R = Resin-based grout

5.5.2 Test Group B

The final group of tests focused on analysing the response of specimens longer than 500 mm. As with the previous group of tests, testing proceeded by applying an axial load under displacement controlled loading past the point of irreversible failure. For these longer embedment length specimens, this failure was expected to be in the form of failure of the steel bar in tension. These tests were performed in order to attempt to capture the critical embedment length for these loading conditions, as well as the embedment length mobilized as loading progressed.

Table 5-4: Testing outline for group B

Test	DOS Sensor	Specimen	Specimen Length (mm)	Borehole Diameter (mm)	Borehole Prepared	Grout
1	008	f	500	31	Yes	C
2	014	o	700			
3	010	h	1000			
4	009	g				
5	005	j	500	41		
6	013	n		31		R
7	006	d	550	41		C

Note: C = Cement-based grout. R = Resin-based grout

5.6 Relevance to Research

The proper preparation of all testing specimens was an important consideration for this research program in order to attain consistent results. The procedures carefully followed to ensure this consistency were covered in detailed in this chapter. Additionally, the chapter covered the development of a testing rig that made possible the acquisition of reliable test data. Instrumentation was selected in order to improve previous attempts at capturing the mechanical response of axially-loaded rock bolts. This preparation made it possible for tests to be conducted with confidence and in an efficient manner. Furthermore, the test program and procedures were highlighted in the chapter.

6 NUMERICAL MODELLING

6.1 Introduction

Numerical modelling was performed as part of this research program using the commercially available software, RS2 (Phase2 9.0). Various permutations of numerical models were developed, duplicating the conditions experienced by the pull-out testing specimens tested in the RMCC Structures Laboratory (Table 5-4 and Table 5-5) were developed. The importance and relevance of numerical simulations is presented below. The necessity of improving the current state with regards to the current capabilities of modern numerical modelling software is showcased; mainly focussed on the idealizations that are present and the limitations of such numerical tools. The process followed in order to properly develop such numerical models is also included. Specific details pertaining to the numerical model(s) itself are covered including the model dimensions, restraints, material properties, and loading conditions. The numerical modelling results are presented in Chapter 7.

6.2 Numerical Modelling within GeoMechanics

As covered in Chapter 2, design engineers have various tools at their disposal in order to ensure that the design of ground support is adequate for each individual application. Analytical methods are extremely useful since they provide insight into potential behaviour due to construction techniques and failure mechanisms. However, the results attained from analytical solutions are limited as they are only accurate within the range of assumptions for which they were designed. Many of these assumptions include: elastic behaviour (*i.e.* constitutive relationships), homogeneous ground, isotropic ground, time independent behaviour, quasi-static loading as well as assumptions associated with input parameter of material strength interaction parameters. In spite of their practicality, the reality of the complex inhomogeneous and anisotropic ground within which fully grouted rock bolts are most commonly used, makes most simplistic analytical solutions inadequate for design considerations. Accordingly, numerical modelling provides much more flexibility and can help more discretely define rock bolt support design criteria. More specifically, in the geomechanics community, these numerical simulations have been increasingly used due to the advanced capabilities of computers. These models have become an essential consideration in understanding the behaviour of the ground, as affected by excavations or other geotechnical works. They make it possible to combine diverse geological

conditions with the mechanical behaviour of support members. These interactions between the ground and the support would otherwise be difficult to analyse.

The various numerical modelling solutions available can generally be classified into continuum and discontinuum (or discrete) methods. Continuum methods take into account the discontinuities in a medium implicitly whereas discontinuum methods account for these discontinuities explicitly. The need for either method generally depends on the size and scale of the discontinuities present in the ground with respect to the size and scale of the problem. This is depicted in Figure 6.1. Although the figure provides certain qualitative guidelines to follow, there is flexibility to the applicability of either method. Continuum approaches should be used for rock masses with no fractures or with many fractures – such that the behaviour of the ground can be approximated with the use of equivalent properties (*i.e.* such that these take into account the effect of the present discontinuities). Continuum solutions should therefore be used when no complete detachment of a section of the ground is expected or when the general behaviour is sought. Conversely, Discontinuum approaches should be saved for cases where the discontinuities present within the ground are more difficult to represent implicitly, or when the detachment of large blocks of the ground is expected to occur. However, due to the set-backs inherent with the different methods, the optimal solution is often found in utilizing a combination of continuum and discontinuum modelling methods in different regions of the model (*i.e.* a hybrid method).

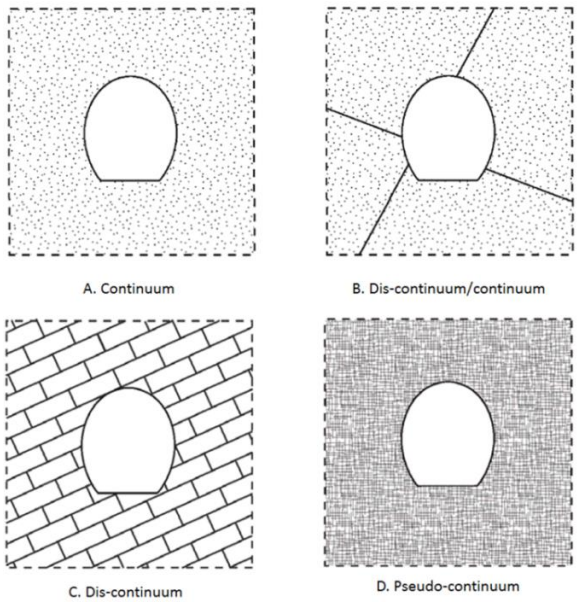

Figure 6.1: Continuum and discontinuum scenarios (as seen in Bobet, 2010)

The continuum numerical modelling methods available include:

1. Finite difference method (FDM);
2. Finite element method (FEM); and,
3. Boundary element method (BEM).

Discontinuum modelling solutions include:

1. Distinct element method (DEM);
2. Discontinuous deformation analysis (DDA); and,
3. Bonded particle model (BPM).

One of the most common numerical modelling methods is FEM since it makes it possible to represent geotechnical problems by using a finite number of defined components. In this scenario, the global behaviour is determined through a set of inter-relations between the individual components. A common example of the use of this method is a beam problem in structural engineering. The beam is represented by a discrete number of elements and the problem is generally easy to solve once the general framework has been constructed. However, in geotechnical applications, various ground characterization problems create a more complex scenario demanding infinitesimal elements, and differential equations to solve the behaviour of the system at various locations is necessary. In FEM, the problem is divided up into elements of smaller size and a standard shape (*e.g.* triangle, quadrilateral, etc.). These elements have a fixed number of nodes at the vertices and/or sides. This is regarded as discretizing the model. Polynomial equations are then used to help approximate the behaviour of the partial differential equations for each element and produce local algebraic equations to represent the behaviour of the elements. These local equations are arranged, using the relationships between nodes, into a global system of equations. This global system of equations is then solved by using boundary conditions. Overall, FEM is the most common numerical method in engineering today due to its flexibility in handling all sorts of materials. Many different commercial solutions that use FEM exist. These are user-friendly and are capable of handling extremely complex problems.

6.2.1 Numerical Modelling Limitations

Although numerical modelling provides a tool for engineers to design rock support, it is not with its limitations. The most pressing limitation of numerical modelling is the difficulty in simulating the conditions of the ground/rock. Rock is created through a complex natural geological process. This oftentimes creates a discontinuous, anisotropic, inhomogeneous, and inelastic material. The dynamic movement of the upper crust of the Earth causes these large rock masses to

constantly be under stress. Furthermore, rock is often porous meaning that fluids can travel within it. These make it difficult to numerically represent the ground. These rock characterization problems can be summarized into the following points (Jing, 2003):

1. *In situ* rock stress is not easy to characterize over the model region;

2. Rock properties measured in the lab may not represent values at a larger scale;

3. Rock properties cannot be measured directly in the field;

4. Rock properties may have to be estimated from empirical characterization techniques; and,

5. It is difficult in quantifying the uncertainty inherent with rock property estimates.

Although these rock characterization problems pose a challenge when using numerical models, the careful selection of input parameters can make it possible for these methods to provide dependable results. However, due to the inherent complexity of rock engineering problems, there remains an uncertainty with regards to the validity of these numerical models. Accordingly these models need to be validated in practice.

6.3 Pull-out Test Numerical Modelling

Ten (10) numerical models were created in order to study the response of axially loaded, fully grouted rock bolts. They were designed in such a way as to simulate the conditions of the test specimens designed, constructed and tested within the RMCC structures laboratory (Section 5.3.3).

6.3.1 RS2 Overview

In order to model the pull-out tests conducted as part of this investigation, the industry-standard numerical modelling software RS2 (Phase2 9.0) Excavation & Support Design Software from RocScience was used. RS2 is a 2-dimensional (2D) finite element stress analysis program specifically designed for underground and surface excavations. It can be used for both rock and soil applications and provides various material models for both. RS2 offers a wide range of support modelling options. More specifically for this investigation, it has the ability to

directly model rock bolts. The different types of bolts that can be modelled with the software include frictionally anchored rock bolts, mechanically anchored rock bolts, and fully grouted rock bolts. In the software, fully grouted rock bolts are modelled as a composition of linear elements as seen in Figure 6.2. The bolt is split up into elements according to where the member crosses the finite element mesh. The separate bolt elements act independently from one another and only affect other bolt elements indirectly through the influence that they have on the ground. Additionally, the strength and stiffness of the bolt-grout and grout-rock interfaces are not taken into account by the simulation since the bolt is assumed to remain fully bonded to the rock up until failure. In this manner, fully grouted bolts see failure in the model once the axial force acting on the bolt element exceeds the axial capacity of the bolt. At this point, the bolt element is assigned a residual capacity.

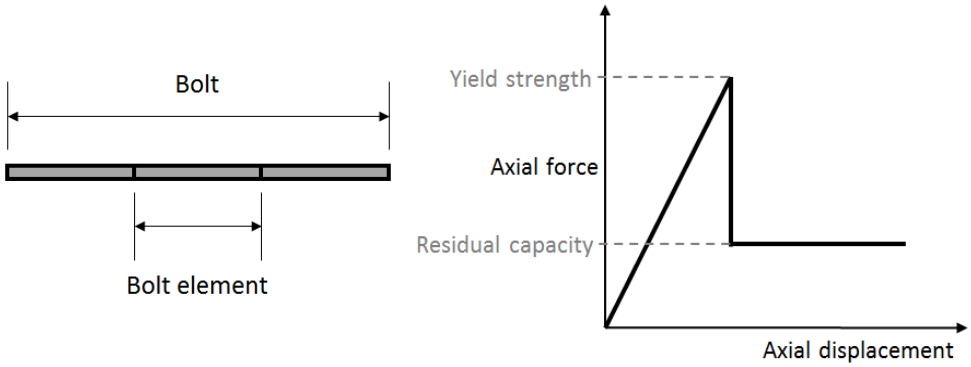

Figure 6.2: Left; Fully grouted rock bolt model. Right; Fully grouted rock bolt failure criteria (modified after RocScience Inc, 2016)

Although this bolt functionality in RS2 makes it possible initially estimate a bolt's pattern capability to support the ground, it vastly simplifies the mechanics associated with axially loading fully grouted rock bolts. The mechanisms directly associated with the interaction at the bolt-grout and grout-rock interfaces are of utmost importance to the success of the bolt, and these are completely ignored by the model. Accordingly, each component of the rock bolt support system was modelled as individual materials.

6.3.2 Modelling Procedure Rationale

In order to ensure good quality results in the modelling of the pull-out tests, a parametric sensitivity analysis was conducted. This began by constructing the most basic representation of the pull-out test and analysing how variations in

different properties affected the results. Once good results were achieved with this basic model, more complexity was added to the model. This process improved the model to a state where it could properly represent the experimental pull-out tests conducted in the lab. Results attained from the instrumentation were then used to calibrate joint properties. Overall, the development of the pull-out test model followed the steps shown in Figure 6.3.

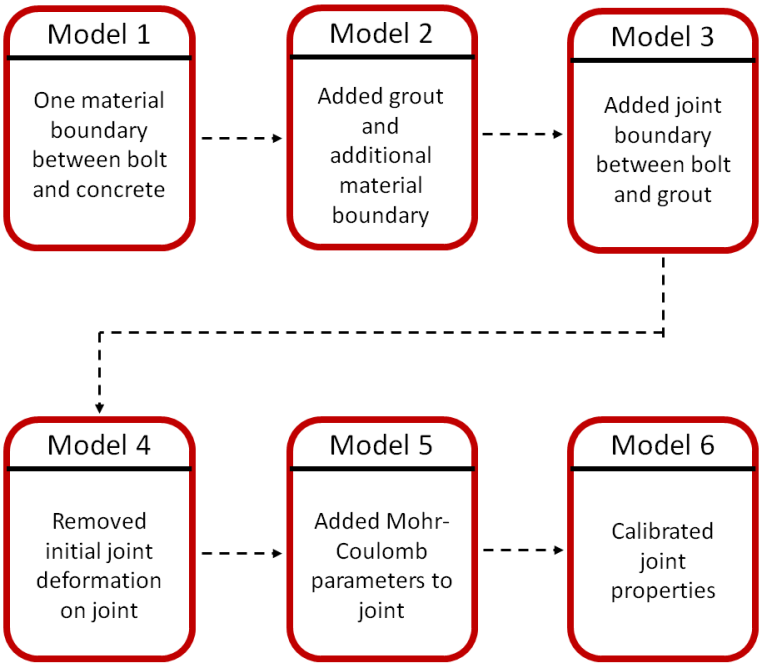

Figure 6.3: Numerical model development used in this study

6.3.3 Model Overview

An axisymmetric model was created in order to simulate the axial response of fully grouted rock bolts. This was selected over plane strain analysis as it portrayed more accurate results in the parametric sensitivity analysis. The effect of the interactions at the interfaces was modelled with the use of joints in RS2. In the software, a joint simply represents an interface along which movement can take place. Each joint can be assigned individual strength and stiffness properties. They are included in the software in order to represent structural discontinuities, and more importantly, interfaces between the support and the ground. The different

interfaces were modelled explicitly by defining joint boundaries between different materials. The final schematic of the model can be seen in Figure 6.4.

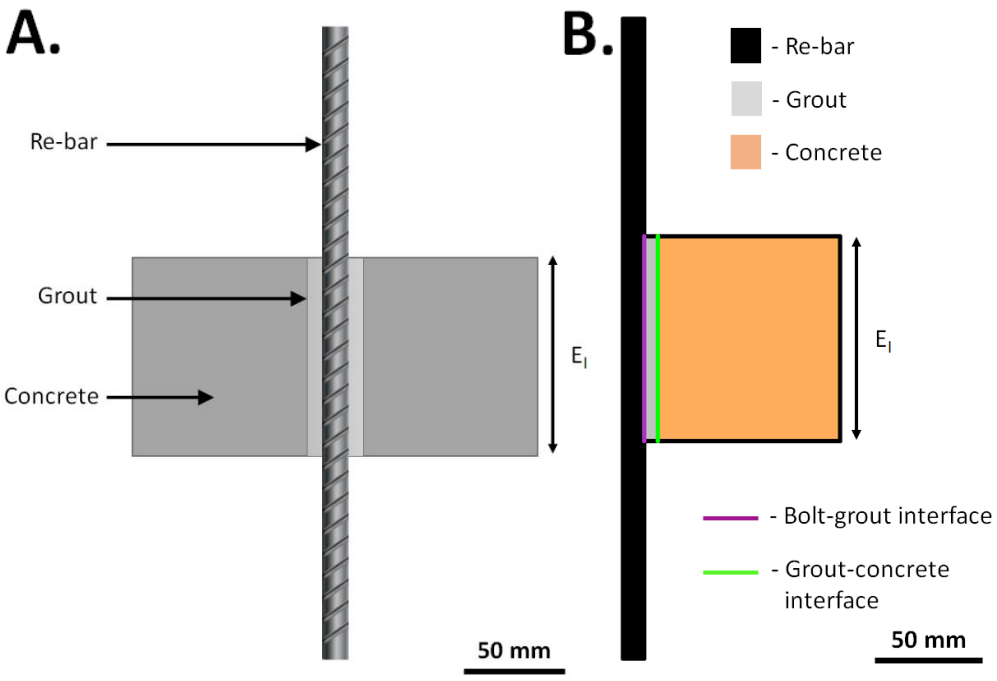

Figure 6.4: A; Experimental pull-out test set up. B; Numerical model pull-out test set up

As can be seen in the figure, all dimensions were matched to those of experimental pull-out tests. The radii used for the different materials can be found in Table 6-1. Two different grout radii were used to simulate the different grout annuli covered in experimental testing. Furthermore, several permutations of the model were created by varying the embedment lengths (E_l), as well as modelling the rebar ribs. These were modelled according to the dimensions prescribed in Table 4-2 (Figure 6.5). Table 6-2 is a list of the numerical models developed.

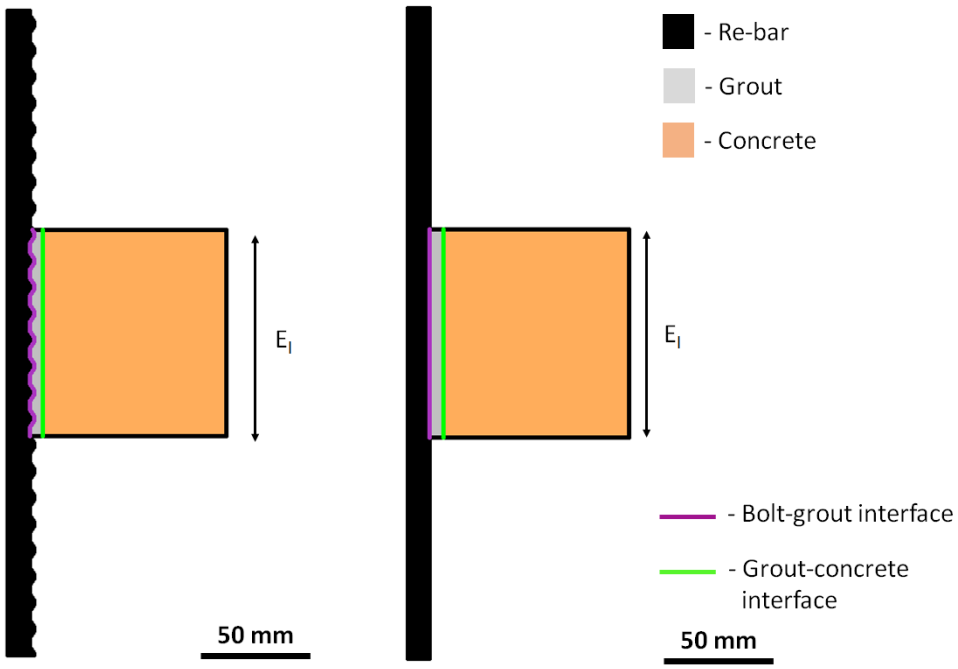

Figure 6.5: Numerical model set up. A; No ribs modeled. B; Ribs modeled

Table 6-1: Model dimensions

Material	Radius (mm)
Bolt	9.5
Grout	15.5
	20.5
Concrete	100.0

Table 6-2: Numerical models developed

Model	Embedment length (mm)	Borehole diameter (mm)	Modelled ribs
1	100	31	No
2			Yes
3	200		No
4			Yes
5	500		No
6			Yes
7	1000		No
8			Yes
9	500	41	No
10			Yes

6.3.4 Model Restraints

An important consideration with the development of the pull-out numerical model was the restraints used to simulate the test loading conditions. The restraints used for the model consisted of rollers along the left side of the bolt simulating axisymmetric conditions necessary for the model. These rollers allow movement only in the direction of the applied load. They ended prior to the cusp at the end of the bolt. Both ends of the bolt were allowed to move freely so that load could be properly applied at the top end of the bolt, and slip could properly take place at the lower end of the bolt. Additional rollers were used on the concrete and grout surfaces. These began just beyond the point where the bolt and grout first intersect and continued all the way to the end of the concrete surface. These rollers only allowed the material to model dilation. This constrain set up can be seen in Figure 6.6. It made it possible for the model to simulate the restraints placed on the experimental pull-out specimens by the load bearing plate and attachment plate as seen in Figure 5.9.

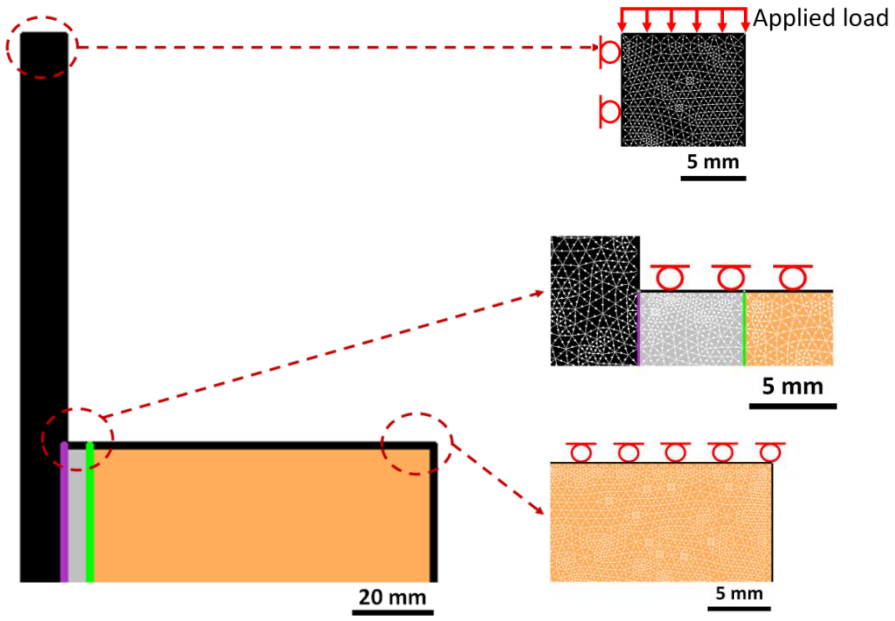

Figure 6.6: Numerical model restraints and loading conditions

The model was discretized into a graded mesh as can be seen in Figure 6.6. The mesh elements were six (6) noded triangles and the default number of nodes on the external was 90. The mesh quality was checked to ensure that no elements had vast differences in the length of the triangle sides. Overall, the mesh sensitivity study performed found no issues with any of the elements in the mesh.

Additionally, in order to simulate the initial confinement provided by the host concrete cylinder and grout to the bolt, as well as the confinement provided vertically to the concrete cylinder, a constant field stress of 10 MPa was applied across the model. This value was selected as calibrated with models 1, 5, and 7 in Table 6-2. It is important to note that in RS2 compression is regarded as being positive. This is a common convention throughout the geomechanics community.

6.3.5 Material Properties

The Mohr-Coulomb failure criterion was used in terms of the various materials in the model. This required a materials cohesion (C), friction angle (ϕ) and tensile strength obtained from the material tests covered in Chapter 4, as well as from accepted values in the literature (*i.e.* friction angles). There is no initial element loading except on the bolt where field stress and body force loading were applied. Body force loading simply represented the self-weight of individual elements as derived through the unit weight of the material whereas the field stress

was derived from the applied constant field stress. This was conducted in order to induce the initial confinement that the bolt experienced due to the grout and concrete prior to loading of the specimen. Furthermore, all materials were modelled elastically and were assumed to be isotropic. The material properties used for all materials can be found in Table 6-3.

Table 6-3: Numerical model material properties

Material	S_t (MPa)	Φ (°)	C (MPa)	v	E (MPa)
Bolt	620.0$^{\Delta}$	0$^{\Delta}$	310.0$^{\Delta}$	0.30$^{\Delta}$	200000$^{*,\Delta}$
Grout	1.8*	35^{+}	0.4^{+}	0.14*	8190*
Concrete	2.8*	35^{+}	1.0^{+}	0.14*	16000*

* According to values obtained from material tests performed as part of this investigation (Chapter 4)
$^{+}$ According to Ardiaca (2009)
$^{\Delta}$ According to ASTM615/615M – 16

The bolt-grout interface was modelled as a material boundary over which a joint was placed. The joint properties used (as calibrated with experimental testing results) can be found in Table 6-4. The use of a joint in this manner allowed the model to properly convey the interface between the support member and the grout. The joint end conditions were selected to be open. This denotes that the end of the joint boundary was represented by two nodes in the finite element mesh. The two nodes can move independently. Open joint end conditions were selected as the bolt-grout interface ends at a surface on both ends. Additionally, the joint was selected to have no initial joint deformation. The Mohr-Coulomb slip criterion was used in order to allow the bolt-grout interface to both behave elastically according to normal and shear joint stiffness, and to experience plastic slipping. Residual strength values were assigned in order to simulate the residual load bearing capacity present throughout the system after the peak strength envelope of the joint was exceeded. Additionally, the grout-concrete interface was modelled as a simple material boundary. This is due to the fact that within the restraints of the pull-out test set up, only the behaviour at the bolt-grout interface should affect results.

Table 6-4: Bolt-grout interface joint properties

Normal Stiffness (MPa/m)	Shear stiffness (MPa/m)	C (MPa)	$C_{residual}$ (MPa)	Φ (°)	$\Phi_{residual}$ (°)
120000	100000	Varies	0	0	50

6.3.6 Model Loading Conditions

The loading conditions applied in the numerical models can be seen in Figure 6.6. Since the response of the rock bolt is required at different applied loads, the model was divided into 31 different stages. At Stage 1 there is no applied load on the bolt. From Stage 2 on, a uniformly distributed load is applied to the top of the rebar normal to the surface of the steel. The load increases progressively through the stages up to a maximum value of 526 MN/m^2. This loading range was more than sufficient to study the response of the rock bolt as loading progressed prior to yielding of any of the materials (*i.e.* applied load < 120 kN to keep the steel rebar from yielding). Additionally, displacement controlled loading was not applied since the bolt, grout, and concrete were modelled elastically.

6.3.7 Model Validation

RS2 provides certain indicators to assess whether the model is stable and the results displayed are accurate and precise. In the solution process of the software, matrix formulations of algebraic equations are used to solve differential equations. The system of equations is then solved using Gaussian eliminations. The system was assessed in terms of equilibrium by the absolute energy criterion. The criterion stops iterations once the energy imbalance of the state of the model becomes a fraction of the energy imbalance of the model at the first iteration. Once this is satisfied, the model is considered to have converged and to provide accurate results. Furthermore, the initial geostatic stress state of the model was examined to reflect that of the applied constant field stress (Section 6.3.4). All models covered in Table 6-2 exhibited the appropriate stresses and displacements in this initial stress state and successfully converged. Accordingly, the results described by the models after this initial geostatic stress state were deemed be accurate.

6.4 Relevance to Research

This chapter covered the importance and relevance of the use of numerical modelling within the realm of geomechanics. More specifically, this chapter focussed on the application of a specific numerical modelling technique as it pertains to ground support elements. The numerical models were developed in order to validate their accuracy with respect to the experimental pull-out tests performed. The development of the numerical models for pull-out tests was covered, and an overview of the numerical model set up was also included. The numerical modelling results can be found in Chapter 7.

7 RESULTS AND DISCUSSION

7.1 Introduction

The compiled results of the rigorous testing scheme performed on fourteen (14) specimens in the RMCC Structures Laboratory are presented in Appendix B. These include samples of varying embedment lengths, grouting materials, and borehole diameters as per Table 5-4 and Table 5-5. This chapter covers selected results from these, in order to highlight the different loading and failure mechanisms captured in all of the tests. Initially, the different results attained with all of the instruments are presented. Afterwards, discussions of the trends witnessed throughout all of the tests are detailed. This includes a look at different loading trends, failure mechanisms, strain profile distributions, and numerical modelling results. Additionally, the effect of the variation of embedment length, grouting material, borehole preparation, and borehole diameter are covered. The results of material tests performed are not presented in this chapter as they are covered in detail in Chapter 4.

7.2 Results

For each pull-out test performed, data from the conventional instrumentation was graphed as a load-displacement curve. The load displacement curve for specimen *m* (Table 5-4) can be seen in Figure 7.1. The results exhibited in the figure represent the applied load as measured by the load cell directly. The axial displacement values, however, were determined from the data captured by the actuator, and the LVDT located at the top of the testing specimen/frame. The actuator measured the entirety of the applied axial displacement. This included any sorts of movements experienced by the testing rig as well as the elongation of the section of the bolt extending outside of the borehole annulus. Accordingly, any sorts of displacements captured by the top LVDT were removed from the applied axial displacement captured by the actuator, as this movement can be attributed to the 'shifting' experienced by the testing rig. Additionally, the elongation associated with the portion of the bolt extending outside of the borehole annulus was removed from the axial displacement readings. In this manner, the axial displacements in all load displacement curves attained with conventional instrumentation represent the behaviour of the system as captured at a single measurement point across the bolt alignment (i.e. at the borehole collar).

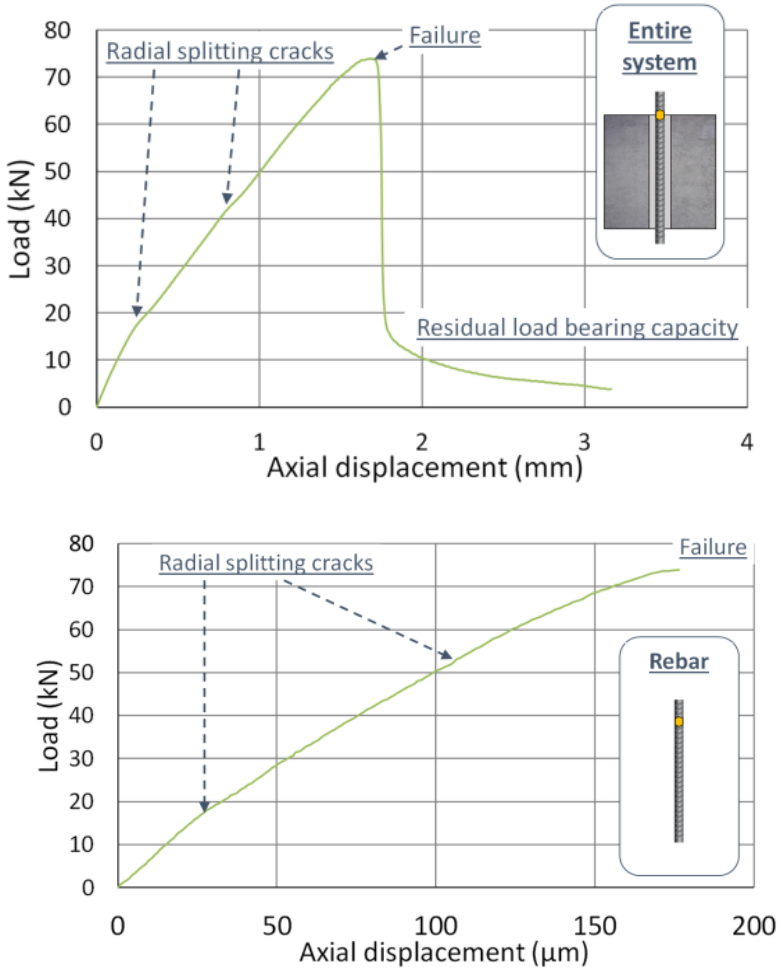

Figure 7.1: Load-displacement curves for specimen *m*. Left; Support system response (conventional instrumentation). Right; Rebar response (Rayleigh DOS)

The data attained from the application of Rayleigh DOS onto the bolt was utilized to derive a load displacement response for the rebar (i.e. the bolt). The displacement of the rebar at the borehole collar was calculated from the summation of the product of the strain (ε_y), as captured by DOS, and the spatial resolution of the readings (Δl) using Equation (7.1).

$$U_{x=E_l} = \sum_{x=0}^{x=E_l} \varepsilon_y * \Delta l \tag{7.1}$$

The ensuing load displacement curve can be seen in Figure 7.1. As can be seen in the figure, the load displacement curve derived with the use of DOS ambiguously resembles the response of the system captured with the use of conventional instrumentation. The initiation of radial splitting cracks is successfully manifested in the responses of both the optical fibre and the conventional instrumentation as a change in stiffness. This change in slope occurred at the same applied load in both load displacement curves. The major difference between the two load displacement curves is seen in the magnitude of the recorded axial displacements. Using conventional instrumentation, failure occurred at an axial displacement of 1.7 mm. On the other hand, Rayleigh DOS captured failure occurring at 176 μm. This 1.5 mm difference in axial displacement can be attributed to two main factors. First of all, the axial displacements derived using DOS do not take into account any slipping seen at the toe end of the bolt. As seen in Figure 7.2, at failure, roughly 1.5 mm of axial slip were observed. In this manner, most of the difference in the axial displacement results is taken into account. Any further discrepancies between the measurements arise due to any additional slipping that may have occurred due to the dilation that developed at the bolt-grout interface as radial splitting cracks began to take place. This sort of movement is not accounted for in the response of the optical fibre. Accordingly, the load-displacement curve attained using conventional instrumentation summarizes the response of the entire support system whereas the results attained with the optical fibre summarize the response of the bolt. The yellow squares of the system and rebar schematics in Figure 7.1 are representative of the location at which the response of the system and bolt is captured and expressed (*i.e.* at the borehole collar).

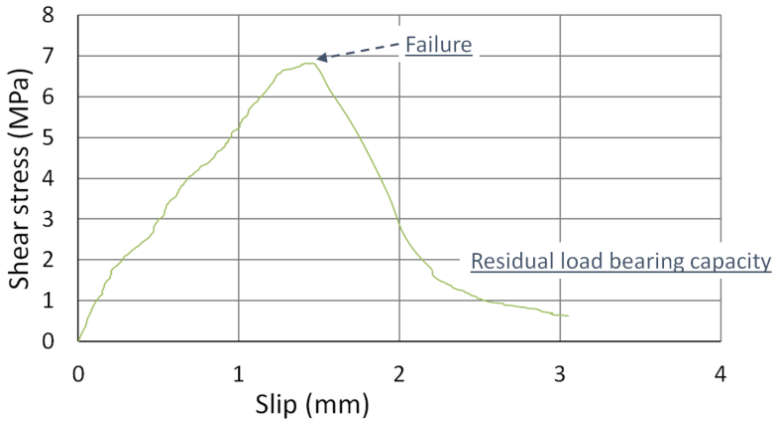

Figure 7.2: Shear stress – slip curve for specimen *m*

The shear stress slip curve of the system can be seen in Figure 7.2. The slip is measured by the bottom LVDT. On the other hand, the shear stress in the graph is calculated by dividing the applied load by the surface of the bolt-grout interface (which decreases as the bolt is pulled out). These results closely resemble the tri-linear slip model presented by Benmokrane, Chennouf, & Mitri (1995). The results, however, divert from the model in the third region of the graph where the shear stress decreases as slip increased.

The results attained from the application of Rayleigh DOS on the bolt can be seen in Figure 7.3. The results are presented as axial strain along the embedded region of the bolt. The arrow in the figure is included to help visualize the location of the strain readings within the specimen. For all ensuing strain profile figures, the 'Start at 0.0 m' location in the pull-out specimen schematic is the 0.00 m location of the strain readings in the graph.

It was generally found that it was difficult to apply a purely axial load onto the grouted bolt. This is due to the initial straightening and realignment that the bolt experiences as load is applied to it. This results in a component of bending associated with loading (*i.e.* not pure axial loading). Accordingly, in order to remove this component of bending experienced by the bolt, the average strain readings of the opposing lengths of the bolt were taken according to Equation (7.2). This is the strain that is depicted in all ensuing strain profile results.

$$\varepsilon_y = \frac{\varepsilon_y^{side\ 1} + \varepsilon_y^{side\ 2}}{2} \tag{7.2}$$

Additionally, although the specimen used in the test was initially expected to have an embedment length equal to the length of the concrete cylinder (*i.e.* 118 mm), an effective embedment length of 94 mm was achieved. This decrease in length can be attributed to a combination of factors including the sedimentation of the grout that occurred during curing, and the utilization of centering pieces to keep the rebar centered within the borehole annulus.

The results seen in Figure 7.3 correspond to the strain profile of the embedded section of the bolt as observed in the initial region of the load-displacement curve of the system (*i.e.* pre-failure region of the load displacement curve). The strain profiles are showcased at different applied loads. The strain is seen to generally decay away from the collar of the borehole to the end of the embedded section of the bolt. Furthermore, the jaggedness (*i.e.* the periodic disturbances) of the strain profiles correspond with the spacing of the bolt ribs – as the ribs cause the cross sectional area of the bolt to change. This is akin to the results described by Hyett, Forbes, & Spearing (2013). Along the section of the bolt that extended past the concrete cylinder, no strain was captured by the optical fibre. This is due to the fact that the load taken on by the bolt was successfully transferred from the bolt, to the grout and concrete cylinder, along the embedded region of the bolt.

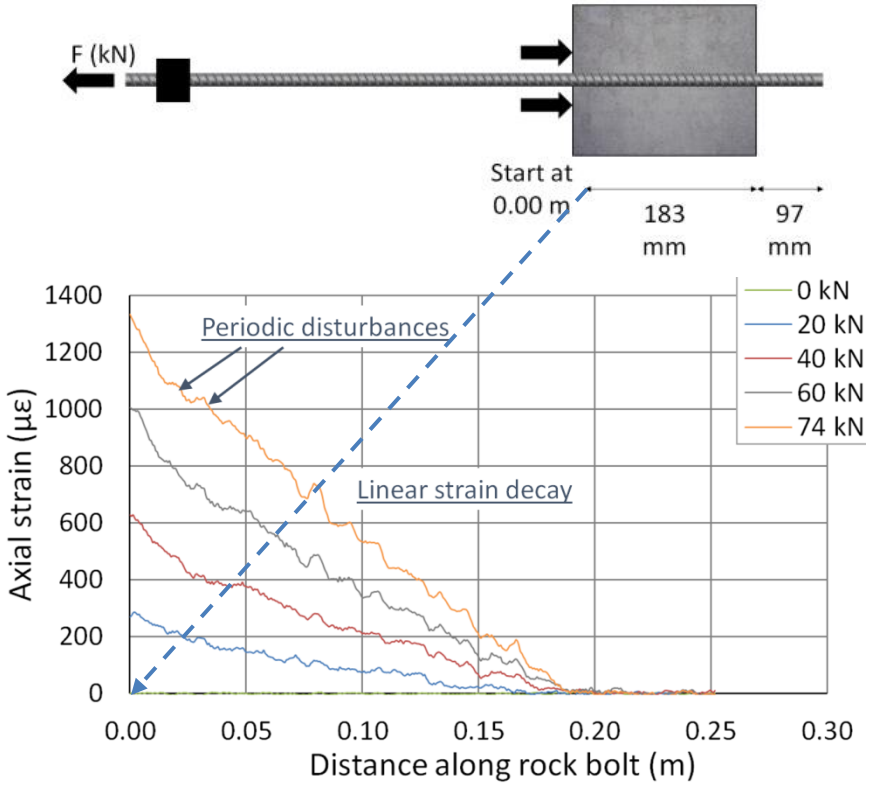

Figure 7.3: DOS strain profile results for specimen *m* (embedded bolt section only), pre failure

After all the tests were conducted, all concrete cylinders were carefully cut open in order to examine the state of the grout and bolt after loading. The post testing analysis of the grout and bolt performed on specimen *l* can be seen in Figure 7.4. The grout was adversely affected by the movement of the bolt along the grout surface as indicated by the observed grout break up and shearing. These sheared sections of grout were found built up in between the bolt ribs (*i.e.* grout residue in between ribs). These findings validate the 4 mm of slip captured by the bottom LVDT. This slipping induced the movement of the bolt across the grout as loading progressed. Overall, the results from the post testing forensics were used to validate the behaviours captured by both conventional instrumentation and Rayleigh DOS.

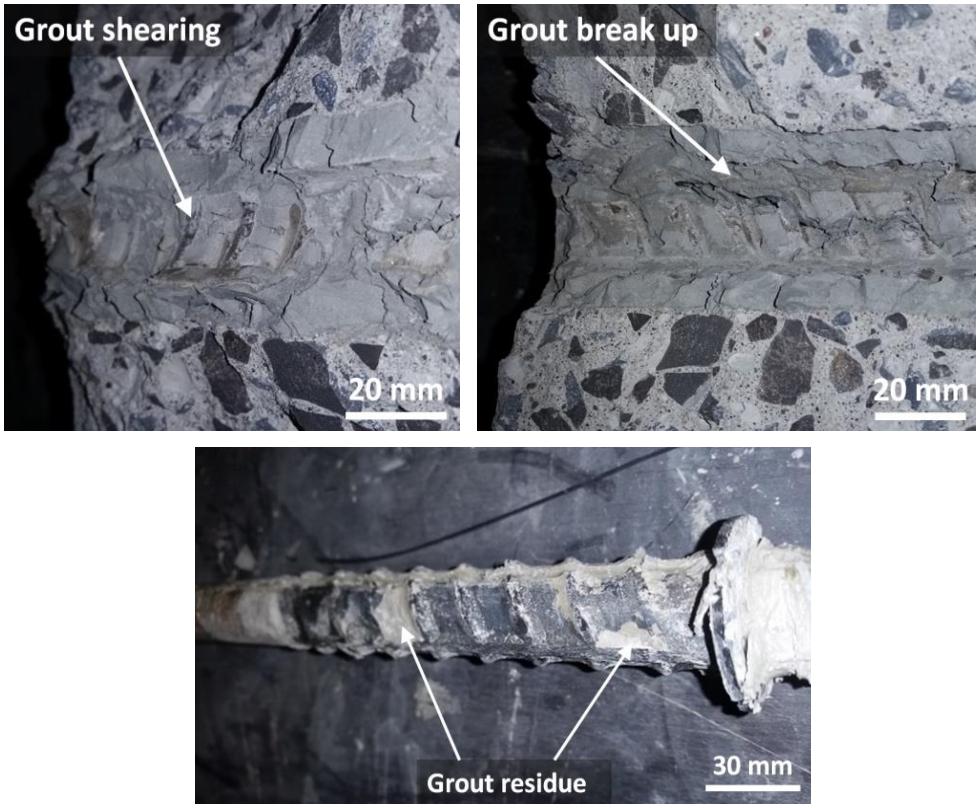

Figure 7.4: Specimen *l* post testing analysis

Five of the physical pull-out test specimens were modelled within the numerical modelling software RS2 (Phase 2.0 9.0) as per Table 6-2. The models developed for specimen *l*, both with and without ribs on the bolt profile, are shown in Figure 7.5. The strain profiles achieved with the numerical model generally agreed well with the results attained with DOS. On average, the physical pull-out test results attained lower values of strain along the bolt alignment than the numerical model developed with no ribs on the bolt (by around 20 %). These differences were magnified at higher applied loads. Additionally, the same model omitted the periodic disturbances seen in the response of the rock bolt.

The results captured within the numerical model with ribs on the bolt profile achieved lower values of strain than the rib-less model (13 % average). This quantifies the importance that the ribs on the bolt have on the load carrying capacity of the system. Additionally, the use of ribs in the model affected the strain profile results as can be seen by the periodic disturbances that occur along the bolt.

These results agree well with the general strain variations (*i.e.* periodic disturbances) captured with DOS. Additionally, the witnessed decay of the strain profile in the numerical models accurately portrays the linear behaviour seen in the physical testing.

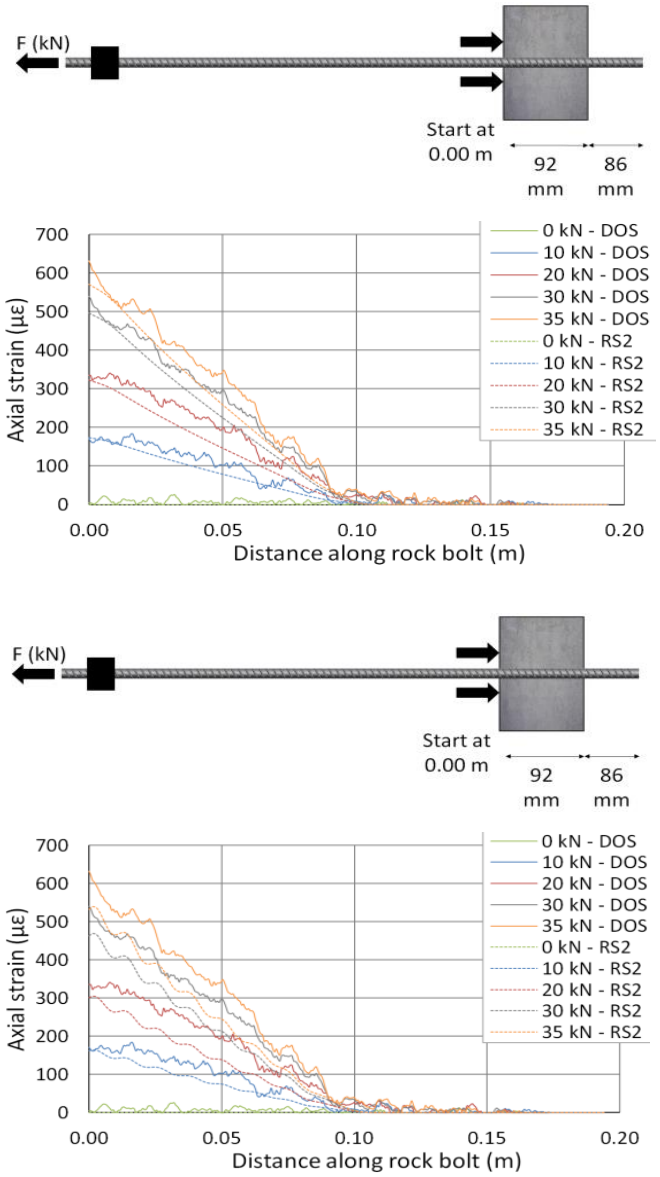

Figure 7.5: Numerical model strain profile results for specimen *l* (embedded bolt section only). Top; RS2 model with no ribs. Bottom; RS2 model with ribs

Rayleigh DOS was also able to capture the response of the bolt post non-critical failure of the system, as is shown for specimen *m* in Figure 7.6. For this test, a brittle failure mechanism caused the concrete to radially split along two visible regions of the concrete cylinder. The radial splitting of the concrete cylinder decreased the radial confinement provided to the bolt by the surrounding grout and concrete. Accordingly, the amount of contact that existed between the bolt and grout, post failure, was not enough to adequately mobilize the entire shear strength available at the interface (*i.e.* the bolt and grout decoupled). The flat region seen in the strain profile of the bolt is indicative of the region along the embedment length of the bolt that was no longer coupled to the grout. This section of the bolt was incapable of transferring load to the concrete through the grout. Accordingly, the residual load bearing capacity of this specific specimen was solely provided by the region of the bolt 0.1 m into the embedment length and further on.

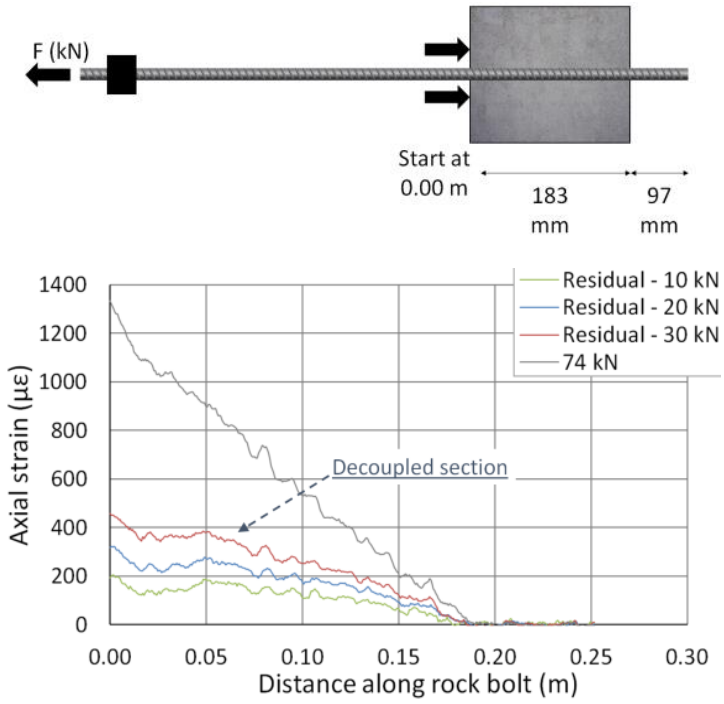

Figure 7.6: DOS strain profile results for specimen *m* post failure

Finally, the strain gauges bonded to the outside surface of the concrete cylinders captured circumferential strains on the outside of the specimens as shown in Figure 7.7 for specimen *l*. These results are representative of the dilation that occurred at the bolt-grout interface throughout all tests.

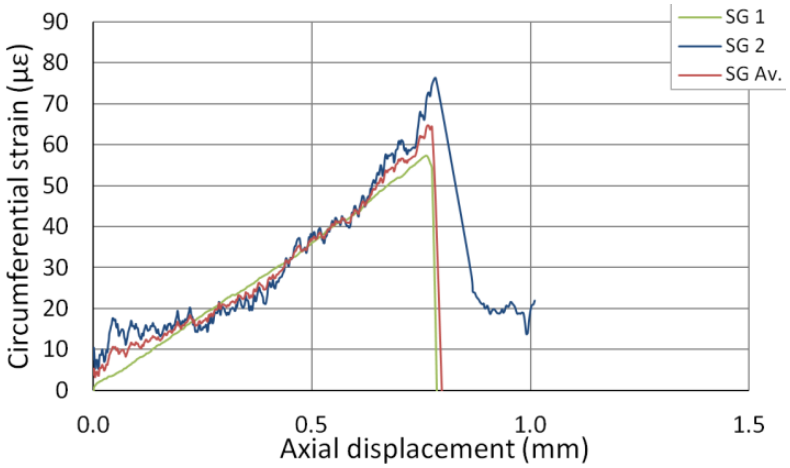

Figure 7.7: Specimen *l* strain gauge results

7.3 Discussion of Results

The results attained on the testing performed on all specimens yielded certain loading trends. Generally, three different behaviours were observed. These behaviours were generally governed by one of the three failure mechanisms shown in Figure 7.8:

A. Rebar tensile failure;
B. Radial splitting crack failure; and,
C. Bolt-grout interface failure.

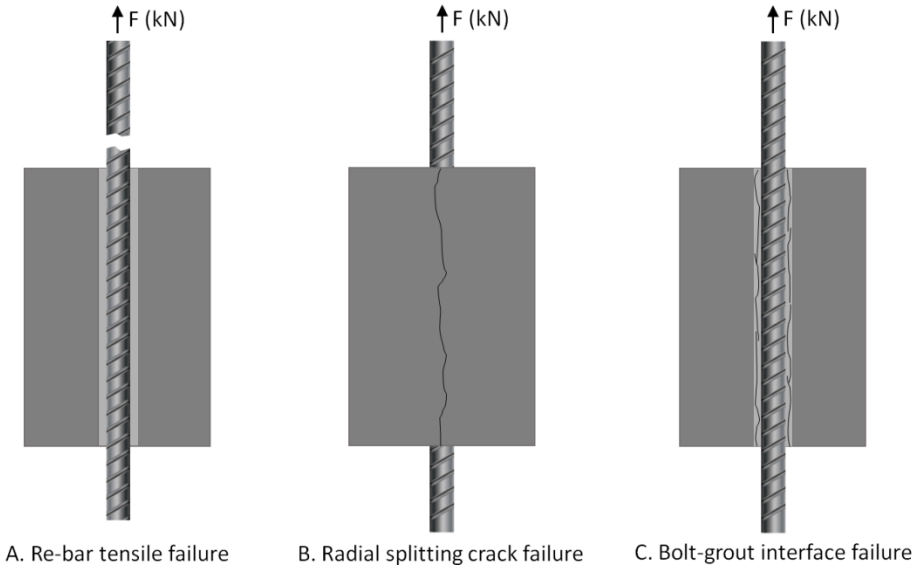

Figure 7.8: Global failure mechanisms

The first observed behaviour corresponded to samples of shorter embedment lengths where radial splitting of the concrete cylinder was the governing failure mechanism. For the first observed behaviour, loading can generally be broken up into three main regions as seen in Figure 7.9 (specimen *m* with 183 mm embedment length):

1. An initial quasi linear region of the load displacement curve of the system which occurred at low axial displacements. Along this region, the initiation of radial splitting cracks occurred which effectively helped decrease the stiffness of the system as loading progressed;

2. A peak load carrying capacity region of the graph where failure of the concrete cylinders occurred. This failure was brought about by the propagation of the radial splitting cracks within the grout and concrete; and,

3. A residual load bearing capacity region where the remaining shear resistance present at the bolt-grout interface, as provided by friction, decreased as the bolt was incrementally pulled out of the borehole.

Throughout the initial quasi linear region of the graph, the emergence of radial splitting cracks within the grout and concrete began at a load of 16.6 kN and axial displacement of 0.2 mm for specimen *m*. These cracks were clearly heard,

and are seen in the graph as a change in slope of the curve (*i.e.* decrease in the stiffness of the system). At a load of 42 kN and an axial displacement of 0.8 mm there is once again a change in slope which was likely the extension of these initial radial splitting cracks, or the development of additional ones. The ability of the system to maintain a linear curve past the onset of these cracks is evidence that the crack(s) did not continuously propagate as loading continued, but rather abruptly propagated at the prescribed loading increments. Different specimens behaved differently in this region as some saw the radial splitting cracks continuously propagate and accordingly the stiffness of the system decreased continuously.

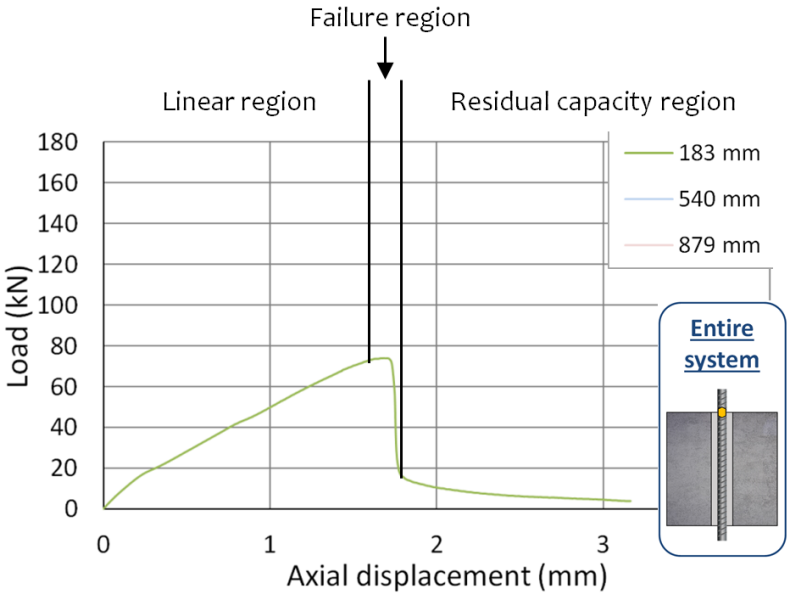

Figure 7.9: Load-displacement curves for specimen *m* (183 mm embedment length), support system response

The effects of these expanding radial splitting cracks were manifested as a sudden loss to the load carrying capacity of the system. Specimen *m* achieved a peak load bearing capacity of 73.9 kN at an axial displacement of 1.7 mm. At this point, two radial splitting cracks became visible on the outside of the concrete cylinder. This observed failure mode is akin to that detailed by Tepfers (1979). The development of these radial splitting cracks as loading progressed is detailed in Figure 7.10. The interaction between the bolt ribs and grout controlled the amount of slipping observed throughout loading. As the bolt ribs moved alongside the grout annulus, the bolt profile pushed outwards onto the grout and concrete cylinder annulus. The radial components of the force generated by this movement were balanced out by the confinement provided to the bolt, by the grout and

concrete cylinder. As the grout and concrete tensile strengths were exceeded, radial splitting cracks emerged at the bolt-grout interface. These radial splitting cracks continued to propagate until the concrete cylinders completely failed. This failure mechanism can be associated with the constant increase of circumferential strain – as recorded by the ers gauges (as seen in Figure 7.7).

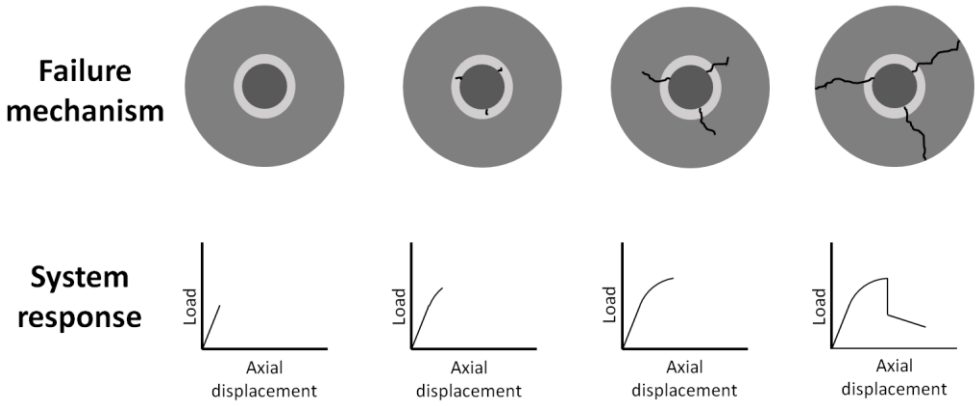

Figure 7.10: Radial splitting crack failure mechanism development (modified after Hyett *et al*., 1992

The radial splitting cracks induced a brittle failure along clearly visible regions of the concrete cylinder. Such a failure is shown in Figure 7.11 for specimen *i*. These cracks caused the load carrying capacity of the system to decrease substantially. This residual load bearing capacity continued to decrease as the bolt was incrementally pulled out of the annulus. However, this did not occur in a linear fashion as the dilation cracks, which had now fully propagated across the grout and concrete, likely continued to dilate as loading continued.

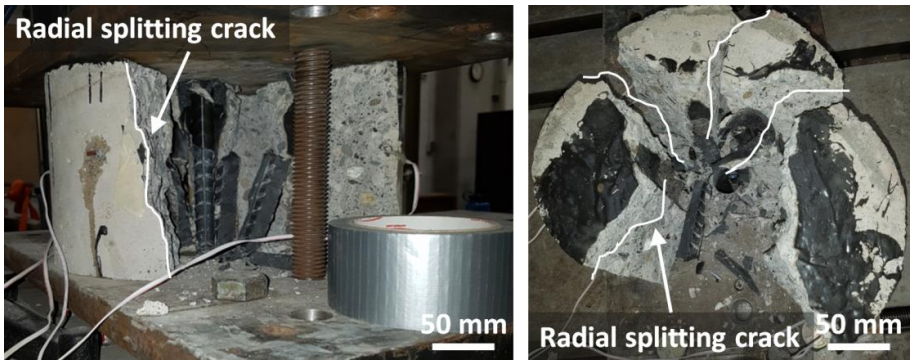

Figure 7.11: Specimen *i* radial splitting of concrete cylinder and grout

The damage developed at the bolt-grout interface throughout testing can be seen in Figure 7.12. It can be seen that once testing had concluded the bolt had completely detached from the grout annulus. Additionally, the grout had been sheared by the bolt moving across it. These results are indicative that considerable movement occurred at the bolt-grout interface; approximately 3 mm was captured by the instrumentation. Furthermore, the detachment of the bolt from the grout and the existence of grout residue between the bolt ribs indicate that a combination of the failure mechanisms seen in Figure 7.8 occurred.

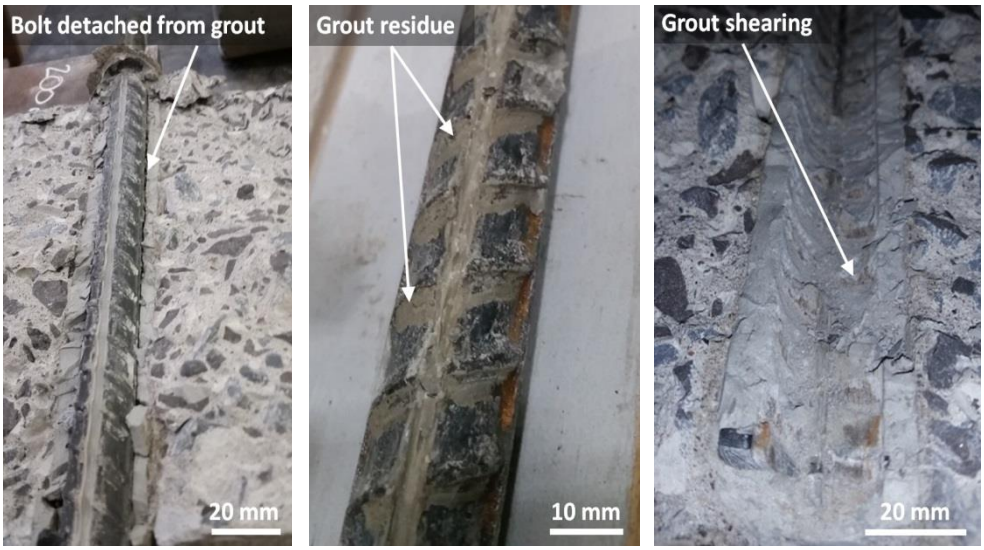

Figure 7.12: Specimen *m* post testing analysis

The second observed behaviour is associated with samples whereby the concrete cylinder remained intact and the bolt-grout interface failed. This was the case for specimen *o*, where a longer concrete cylinder length made it possible for the system to withstand the effects of radial splitting cracks. Here, the externally mounted strain gauges affected the effectiveness of the anchoring effect of the rebar ribs. Accordingly, this sample failed at the bolt-grout interface. This behaviour is hypothesized to be applicable for shorter embedment length samples where a high radial confinement exists in such a way that the effects of radial splitting cracks are mitigated. Three main regions are associated with this loading behaviour as seen in Figure 7.13 (specimen *o* with 540 mm embedment length):

1. An initial quasi linear region of the load displacement graph at low axial displacements;

2. A peak load region whereby the bolt-grout interface failed; and,

3. A residual load carrying capacity region where the shear resistance of the system decreases step-wise as the rebar ribs shear past the grout ridges.

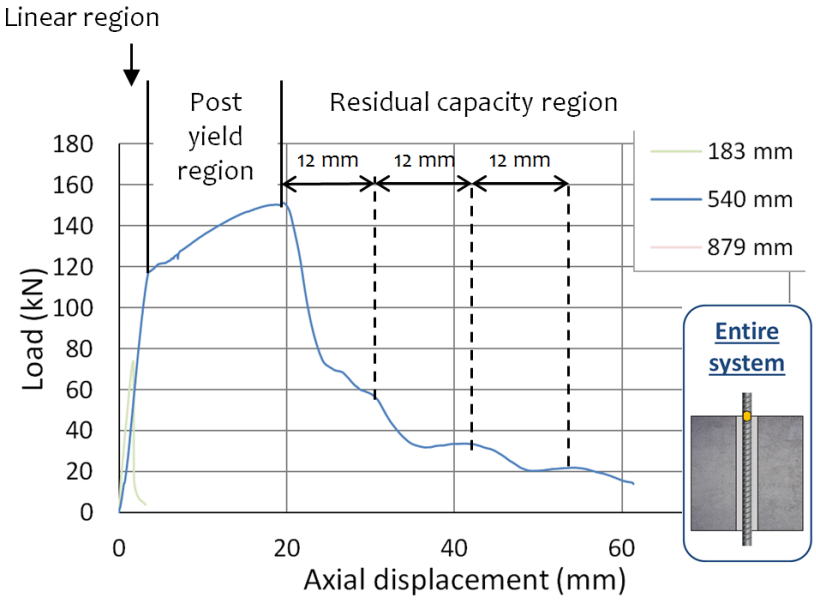

Figure 7.13: Load-displacement curves for specimen *o* (540 mm embedment length), support system response

The maximum load the system was able to withstand was 151.2 kN at an axial displacement of 19.7 mm. In the initial linear region of the load displacement curve, the load carrying capacity of the system increased linearly up to a value of 117.8 kN and 3.8 mm. At this point, the yielding of the steel bar caused the sudden loss of the stiffness of the system as a flatter curve continues past this point. A strain hardening region of the graph continues past this point, up to the peak load, where failure of the bolt-grout interface occurred in two distinct mechanisms as shown in Figure 7.14. In the cases where enough confinement is provided to the bolt-grout interface in order to prevent a volumetric increase at the interface, grout shearing occurs. On the other hand when not enough confinement exists, a volumetric increase at the bolt-grout interface will induce the movement of the bolt up and over the grout ridges (referred to as dilational slip).

After this point, the system exhibited some ductility, as it was able to maintain a residual load. However, after approximately 12 mm of axial displacement, this residual load carrying capacity drastically decreased (*i.e.* from 60 kN to under 40 kN). This pattern continued as loading progressed as can be seen in Figure 7.13. This behaviour of the system can be attributed to dilational slipping occurring at the bolt-grout interface (Figure 7.14). As the rebar ribs move past a specific section of the grout where good frictional resistance was achieved, the bolt slips up and over the grout ridges, and the load bearing capacity of the system decreases drastically. Once the rebar ribs are able to interlock again with the next series of ridges on the grout, the system achieves another relatively constant residual load bearing capacity. The residual load bearing capacity continued to decrease in steps as the bar was pulled out of the borehole. The spacing of the rebar ribs is the same as the length of these steps. These results are akin to those observed by Benmokrane *et al.* (1995) and Blanco Martin (2012).

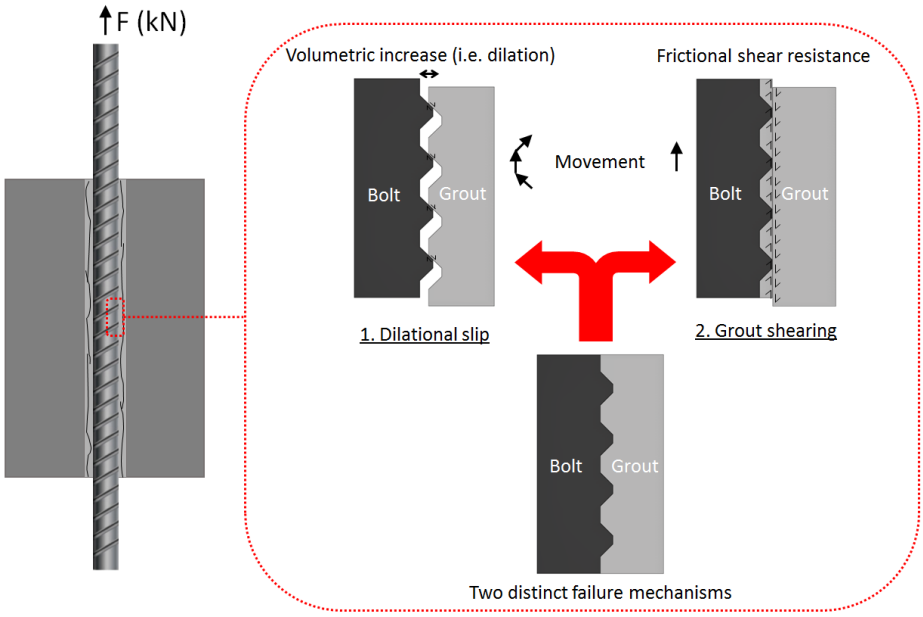

Figure 7.14: Bolt grout interface failure mechanisms

The post-testing forensic analysis performed on the bolt and grout is shown in Figure 7.15. Throughout the entire embedded length of the bolt, significant grout residue was found on the steel bar. There was a distinct gap seen between the bolt and grout surfaces, signifying that the two materials decoupled during testing. Furthermore, the grout ridges were almost completely flattened by the sliding of

the rebar ribs on the grout surface. These results are indicative of the significant amount of slip that was observed (*i.e.* mobilized failure mechanism) and that took place along the bolt-grout interface. Accordingly, failure occurred at the bolt-grout interface through a combination of the two distinct failure mechanism pictured in Figure 7.14. The bolt was pulled out along a cylindrical frictional surface. This failure mode is equivalent to that prescribed by Hyett (1992) for specimens that apply a relatively high radial confinement to the rock bolt during loading. However, the same concrete cylinder was used in all of the tests prescribed herein. Accordingly, this observed failure mode occurred due to the interaction between radial splitting cracks and the concrete cylinders. For shorter embedment lengths, the radial splitting cracks that started early on were able to propagate through the entire length of the concrete cylinder. However for the longer concrete cylinder used in this test, the wedging action created by the ribs was not enough to develop long enough radial splitting cracks to cause failure of the concrete cylinder. Accordingly, a different failure mechanism entirely was observed.

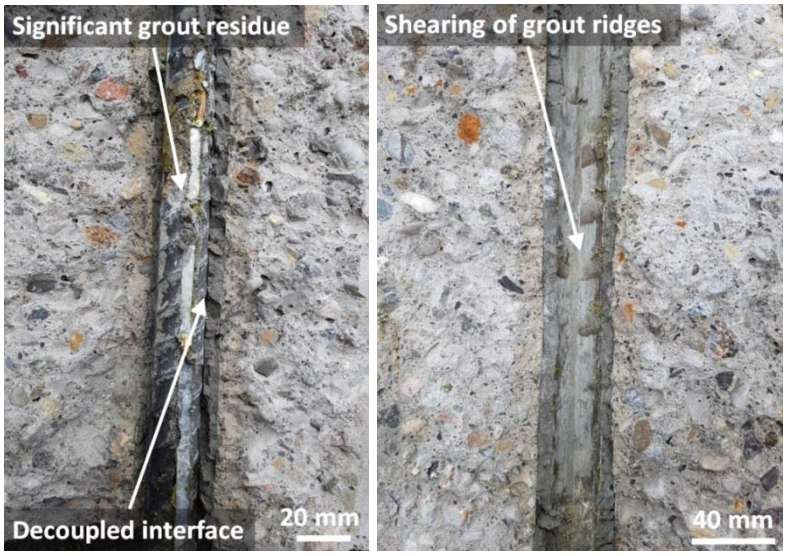

Figure 7.15: Specimen *o* post testing analysis

The final behaviour was observed within samples of longer embedment lengths, whereby failure occurred in the form of tensile failure of the bolt (*i.e.* the rebar). These specimens were able to utilize the full strength of the bolt. The three main loading regions associated with these specimens were (Figure 7.16):

1. An initial quasi linear region where the load carrying capacity of the system increased;

2. A non-linear region of the graph where the steel bar yielded and the stiffness of the system drastically dropped; and,

3. A peak load region of the graph where the rebar failed in tension.

Specimen *g* was able to withstand a load of 172.5 kN at an axial displacement of 39.6 mm. As loading commenced the system stiffness initially increased up to a point where the system stabilized and its stiffness became constant. The load displacement response of the bolt continued to be linear up to approximately 80 kN of applied load where there was a sudden shift in the axial displacement. This shift was manifested as a slight change in the stiffness of the system. The load carrying capacity of the system continued to increase up to roughly 118.4 kN. Once the specimen reached 118.4 kN at an axial displacement of 2.5 mm, the bolt yielded and a sudden decrease in the stiffness of the system occurred. Past this point, a strain hardening region of the graph began up to the point where the bolt failed as its tensile capacity was exceeded.

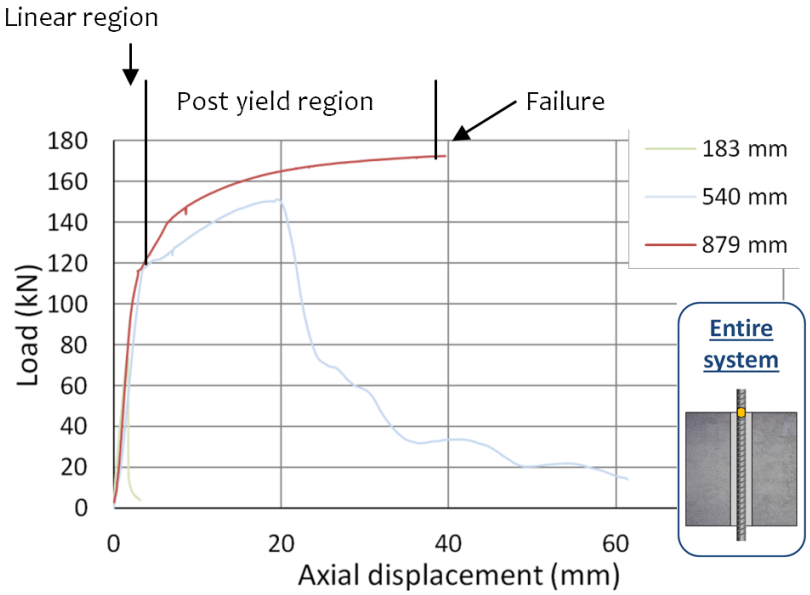

Figure 7.16: Load-displacement curves for specimen *g* (879 mm embedment length), support system response.

Taking a look at the sample post testing (Figure 7.17), there were no significant grout voids found throughout its length. Additionally, the grout was found to be intact and there was no grout residue on any sections of the bolt. All of these results are indicative that mechanical interlocking between the bolt ribs and the grout was the sole provider of shear resistance throughout loading.

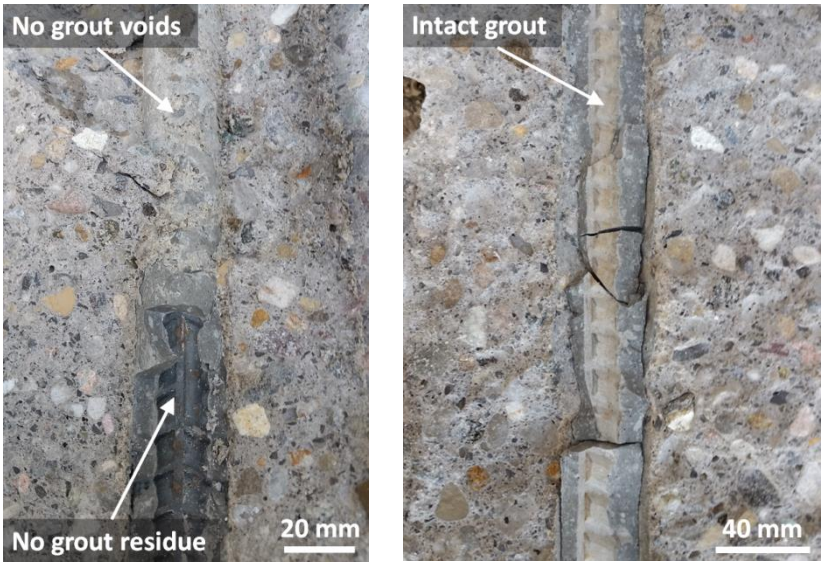

Figure 7.17: Specimen *h* post testing analysis

In a majority of the tests, there were clear differences in the in initial region of loading in the responses of the bolt and the system. This difference is shown in Figure 7.18 for specimen *k*. In the initial region of the response of the support system, there was selected difficulty in mobilizing the shear strength of the system. This is represented in the load-displacement curve of the system as a region with a relatively low axial stiffness. This was mainly attributed to the shifting of the bolt and grout within the annulus to a point where the bolt and grout were able to adequately interlock together. Accordingly, once the bolt and grout shifted into a position where they were properly coupled, the axial stiffness of the system increased. Conversely, where the system had an initial lower axial stiffness, the bolt demonstrated a stiffer response. This is due to the fact that the bolt had to take on the applied load that was not being properly transferred through the bolt-grout interface to the grout and concrete. Consequently, once the stiffness of the support system increased, the system was better able to transfer load from the bolt to the grout and rock. This caused the stiffness of the bolt to decrease. Past this

point, the stiffness values of the system and bolt increased linearly, unless radial splitting cracks emerged. In these cases, the response of the system was affected as shown in Figure 7.10.

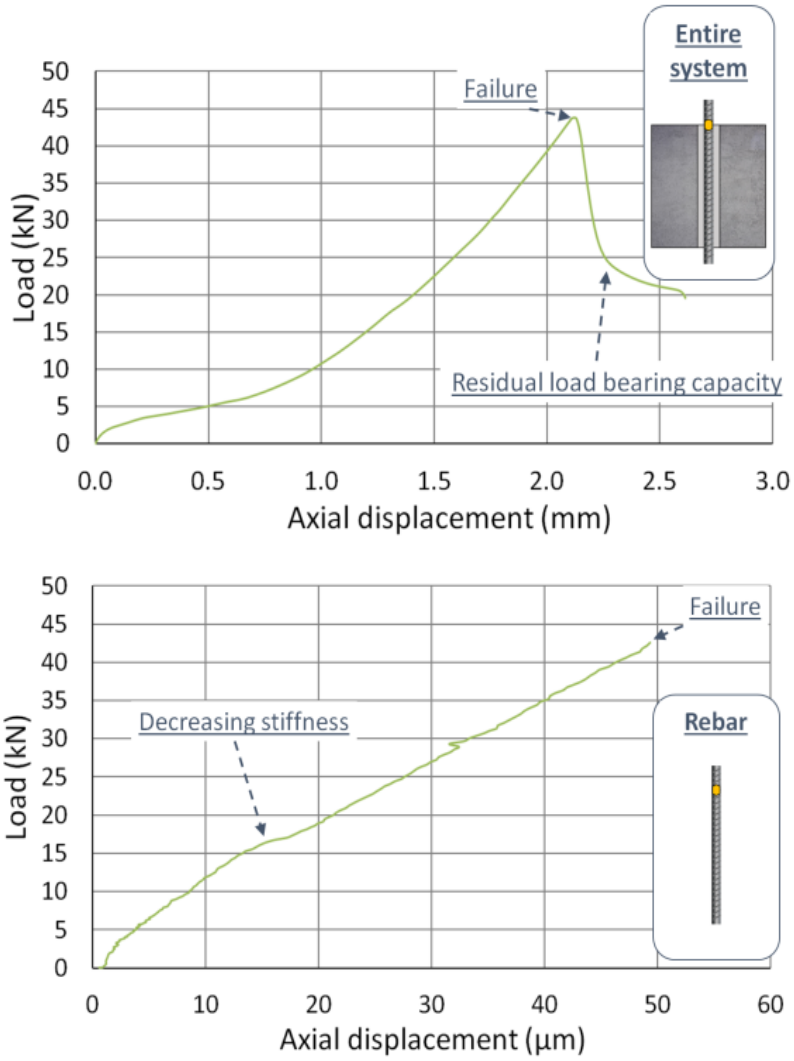

Figure 7.18: Load-displacement curve for specimen *k*. Left; Support system response. Right; Rebar response

Finally, it was generally found that the response of the support system is not reversible, as is indicated by the load displacement curves of specimen *e* (Figure 7.19). Testing of this specimen was unique in that an initial test was

performed on it elastically prior to testing until failure. As loading increased, the specimen began to lose its ability to sustain load due to the existence of radial splitting cracks. This is seen as a decrease in the axial stiffness of the system. The response of the bolt throughout this loading sequence mirrors the behaviour of the system as the bolt's stiffness is initially low. However, as the stiffness of the system decreased, the bolt stiffness increased. In the unloading region of the curves, the system experienced a different stiffness than when load was being added. This shows that the response of the system as a whole is irreversible. However, the response of the bolt is observed to be reversible as the bolt has relatively the same stiffness through the loading and unloading sequences. The locked in strain energy within the bolt account for the minimal deviations observed in its response as the load is removed.

Overall, this difference in the response of the system versus that of bolt exists due to the fact that as loading progresses, shifting of the grout may have occurred. Additionally, sections of the bolt may become decoupled from the grout. It is therefore difficult to have a reversible response of the entire support system as a whole. On the other hand, since the bolt was not loaded past its yield strength, the response of the individual support member is reversible; this is also due to the material properties of steel itself.

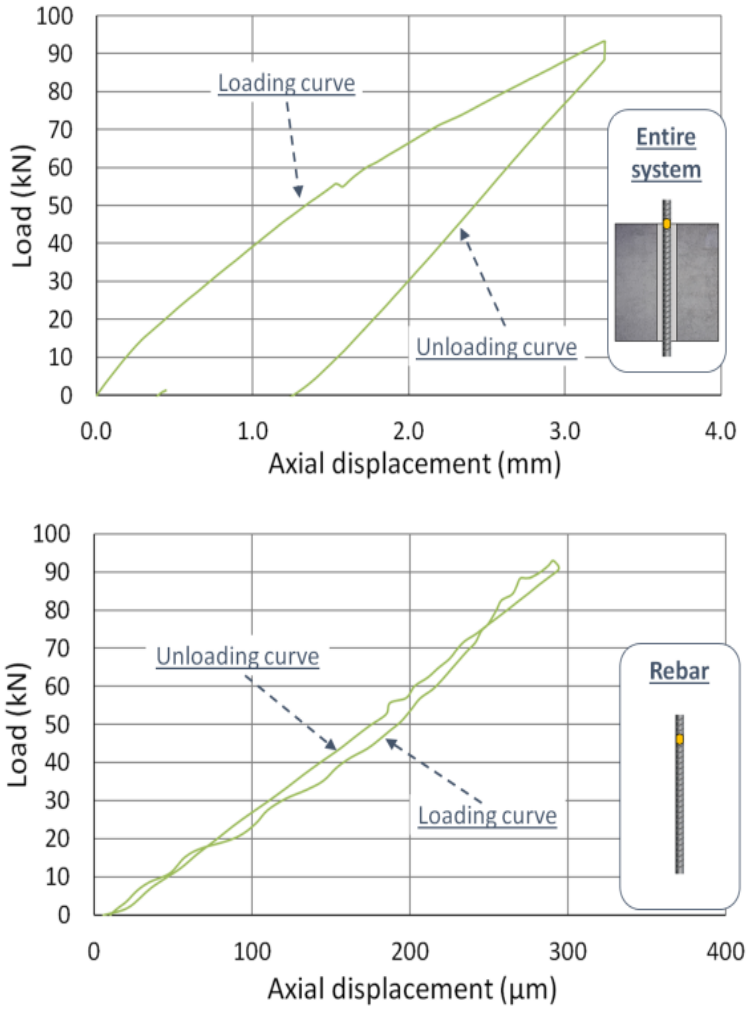

Figure 7.19: Load-displacement curve for specimen *e*, load-unload test. Top; Support system response. Bottom; Rebar response.

7.3.1 Rayleigh DOS

The response of the optical fibre saw some general trends throughout testing. The two behaviours observed in the strain profiles of the bolts are depicted in Figure 7.20. In the graph, the strain profiles are normalized within their embedment lengths. For the specimens where only the frictional component of shear resistance was mobilized, the strain profile linearly decayed within the

embedded region of the bolt. This opposed to the exponential decay form described by Farmer (1975), Li & Stillborg (1999), and Serbousek & Signer (1987) for fully grouted rock bolts. The results for shorter embedment lengths, however, closely resemble the linear decay behaviour predicted for frictionally anchored rock bolts. This was generally observed within specimens with embedment lengths smaller than 500 mm.

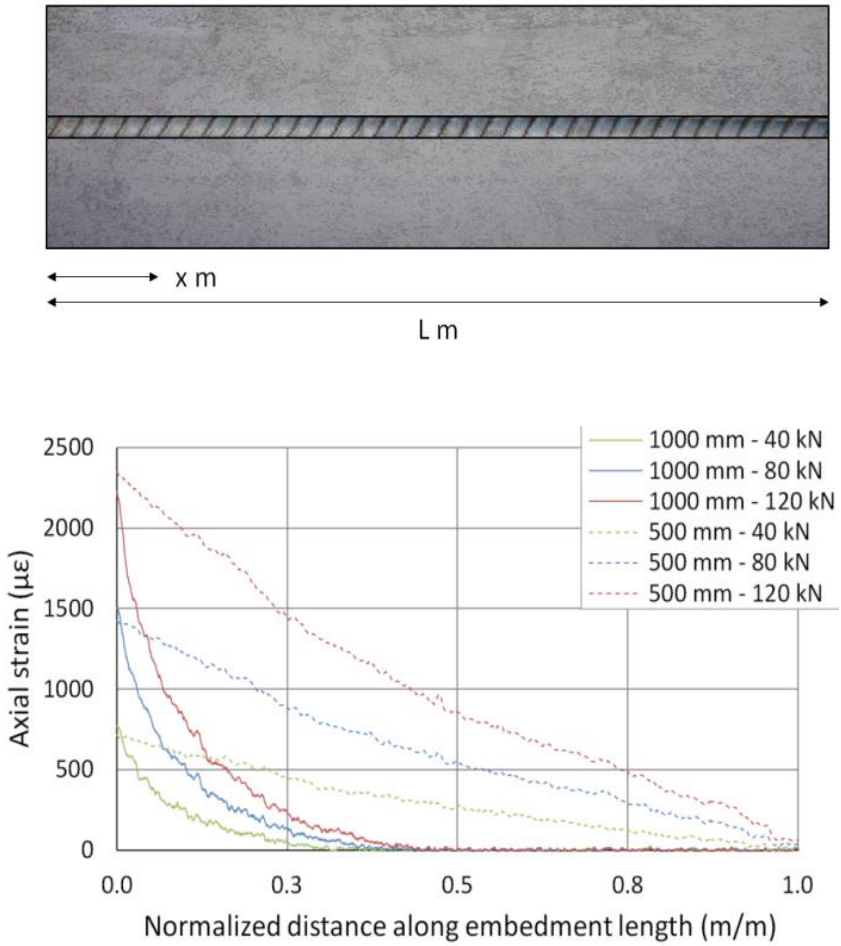

Figure 7.20: Typical DOS strain profile results along embedded bolt section

In the specimens where both the mechanical and frictional component of shear resistance were mobilized, the strain profiles decayed exponentially. This exponential decay form became more pronounced as the embedment length of the specimens increased. This was generally the observed behaviour for specimens

longer than 500 mm. These results are agreeable to the exponential decay behaviour described by Farmer (1975), Li & Stillborg (1999), and Serbousek & Signer (1987).

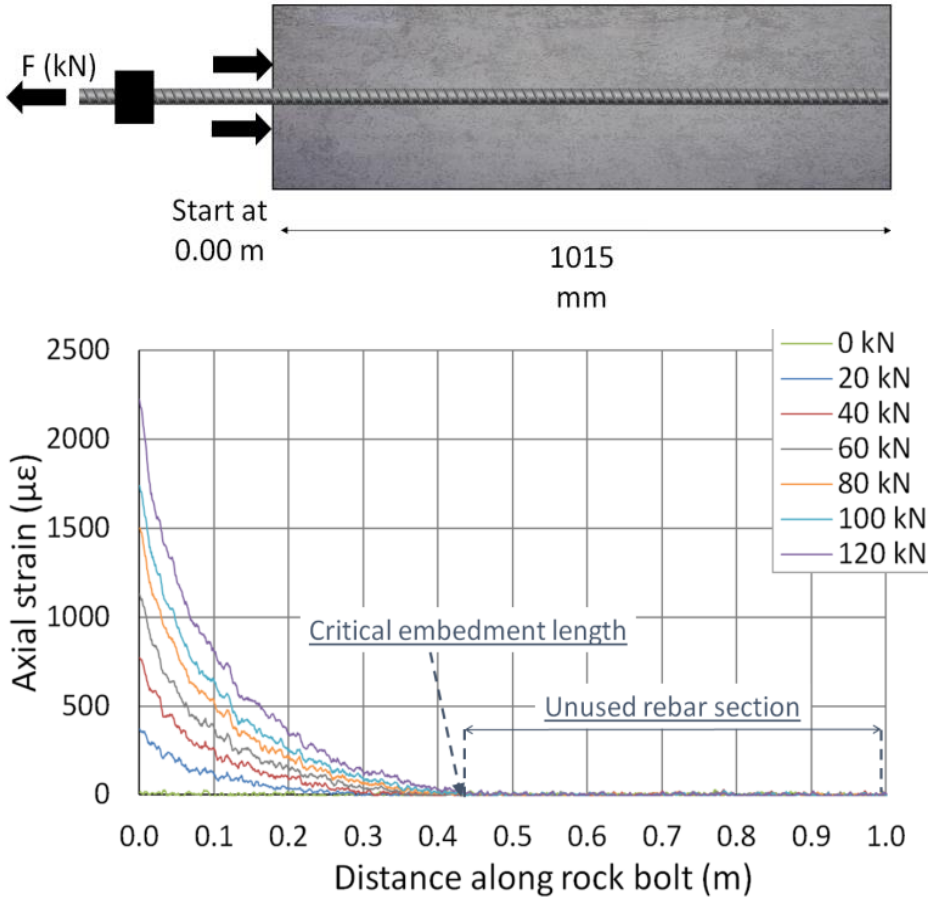

Figure 7.21: DOS strain profile results for specimen *h* (embedded bolt section only)

Specimen *h* had the steepest strain profiles throughout all of the tests. The specimen had an embedment length of 1015 mm. The strain profile distribution along the embedded section of the bolt can be seen in Figure 7.21. The strain profiles show a clearly defined exponential decay behaviour. Taking a look at the sample post testing, there were no significant grout voids found throughout its length. Additionally, the grout was found to be intact and there was no grout residue on any sections of the bolt. All of these results are indicative that

mechanical interlocking between the bolt ribs and the grout was the sole provider of shear resistance throughout loading. More importantly, however, it can be seen that the strain profiles did not mobilize the entire length of the embedded bolt. This is seen as the strain profiles decay to a strain value of zero at a distance of 430 mm through the embedment length, regardless of how much load was applied. This 430 mm length can therefore be regarded as the critical embedment length of the support system. The critical embedment length is the minimum bolt length necessary to use up the entire tensile capacity of the bolt. Knowing this length can help design engineers mitigate ground falls *in situ*.

The application of DOS onto the bolts made it possible to capture the attenuation of the decoupling front along the bolt as seen in Figure 7.6. Additionally, the capability of DOS to capture specific loading features at the microscopic scale, made it possible to capture loading mechanisms associated with quality control issues in the tests. The detailed strain profile distribution for specimen *e*, throughout both loading and unloading, can be seen in Figure 7.22. As mentioned before, this specimen had an initial test performed on it where the system was loaded and unloaded within the elastic range of the bolt. The shape of the strain profiles in the loading sequence portrayed an unexpected result. The strain decayed up to approximately 0.05 m along the embedment length, at which point the curve flattened. From 0.10 m onwards, the strain on the bolt continued to decay to the toe end of the bolt. This unexpected flat region (*i.e.* from 0.05 m to 0.10 m along the embedded region of the rebar) is attributed to a section along the bolt which was not properly bonded to the grout. This section of the bolt was therefore, incapable of properly transferring the axial load on the bolt to the grout and surrounding concrete. The behaviour of the bolt during the unloading sequence is likewise shown in Figure 7.22. As load was removed from the system, the region of the bolt closest to the toe end of the bolt was charged with transferring the entire load throughout the system. Conversely, the region closest to the borehole collar rapidly flattened and approached strain measurements of zero. It can therefore be stated that this region of the bolt did not transfer any load to the grout and concrete as unloading proceeded. Once the entire applied load was removed from the system, some built up tension remained along the bolt.

Overall, from 0.05 m to 0.10 m along the embedded region of the bolt, the existence of grout voids rends the system incapable of properly transferring load from the bolt to the grout and concrete. This behaviour captured by DOS was supported by the post-test forensics performed on the specimen that exposed a section of the grout that contained considerable grout voids (Figure 7.23). These grout voids effectively decrease the ability of the system to successfully transfer load from the bolt to the grout and concrete. This is a quality control issue that has been detected by the fibre optic technology.

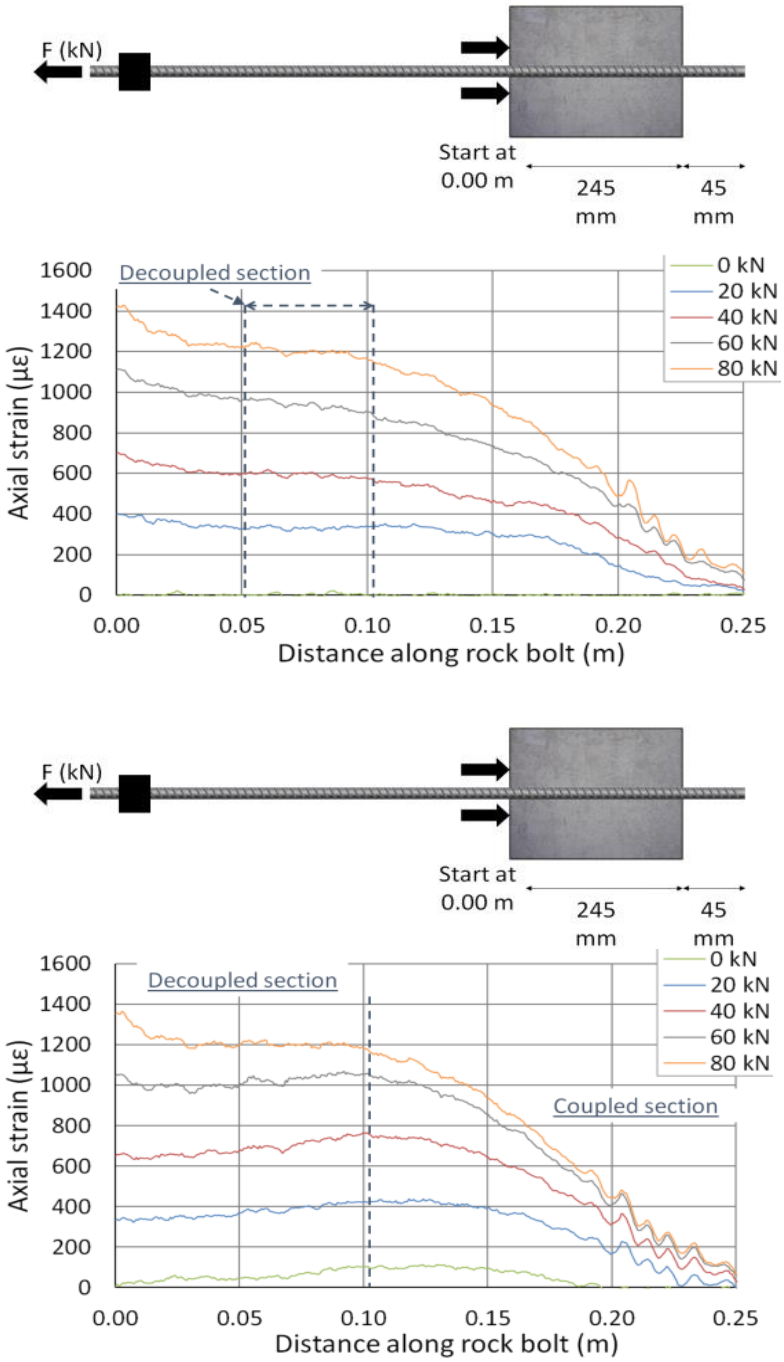

Figure 7.22: DOS strain profile results for specimen *e*, load-unload test (embedded bolt section only). Left; Loading. Right; Unloading.

Figure 7.23: Specimen *e* grout voids

7.3.2 Numerical Modelling

The numerical models developed within the constraints of RS2 generally achieved results that closely predicted the response of the bolt in the physical pull-out tests. This is shown in Figure 7.24, where the results of the numerical models developed for specimens *l* and *h* are compared to the physical tests. For specimen *l*, results predicted by the numerical model achieved lower values than the strain captured by DOS (by roughly 10 %). The variation seen in the strain profile of the bolt (*i.e.* periodic disturbances) was successfully predicted by the numerical model. Additionally, the numerical model predicted strain profiles that linearly decayed away from the borehole collar to the end of the embedded section of the bolt. Likewise, the numerical model developed for specimen *l* successfully predicted the response of the bolt to an accuracy of 3 %. Furthermore, the exponential decay experienced by the bolt in the physical tests was also successfully predicted by the numerical model. The critical embedment length observed in the physical tests was predicted to an accuracy of less than 10 %.

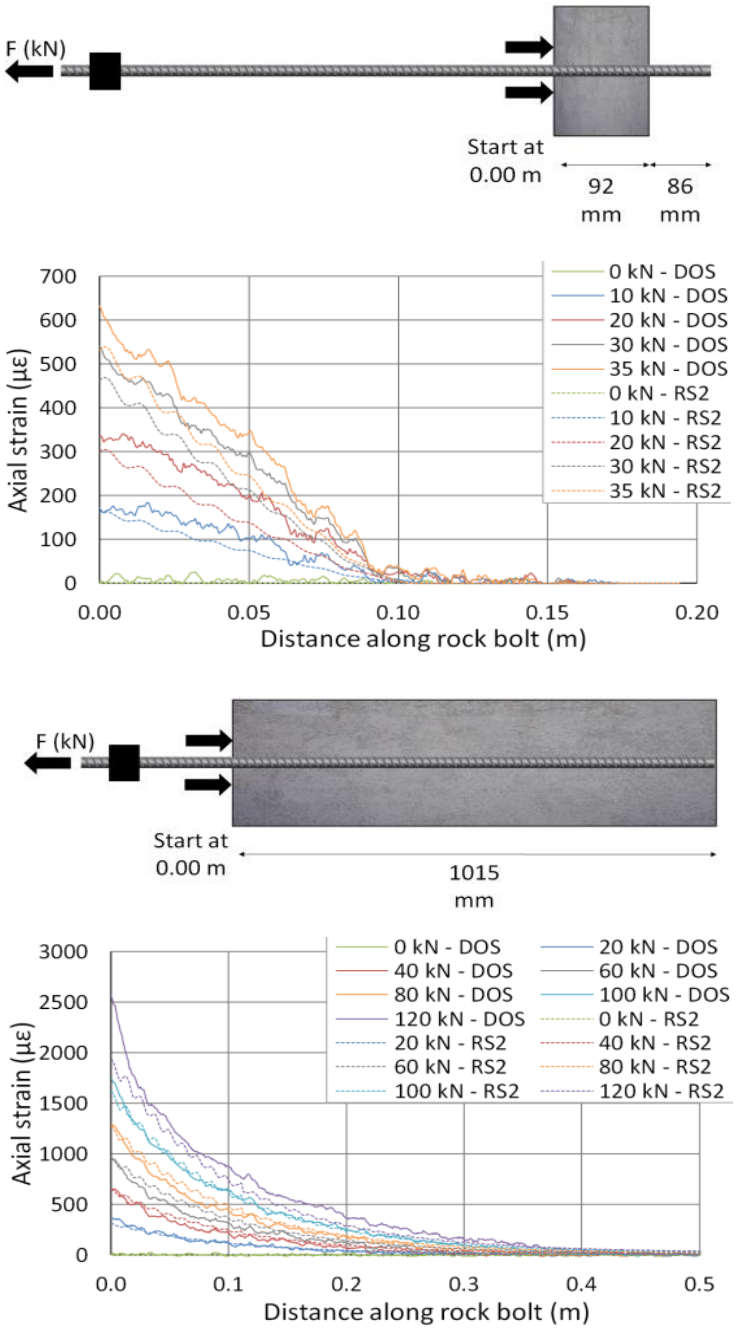

Figure 7.24: Numerical model strain profile results (embedded bolt section only). Top; Specimen *l*. Bottom; Specimen *h*

Although the numerical models successfully predicted the response of the bolt at shorter and longer embedment lengths, it was in between these lengths where RS2 had difficulty. This is shown in the strain profiles in Figure 7.25, where a specimen with an embedment length of 503 mm is shown (specimen *f*). Overall, the numerical model results appeared to divert from the results attained in the physical experimentation using DOS. The numerical model showed lower values of strain across the entire alignment of the bolt. The maximum difference in values was 70 %. The only similarities between the DOS strain profiles and that of the numerical modelling were seen at the borehole collar and toe end of the bolt. The strain values achieved at the borehole collar with the model were almost exact to those attained with DOS (around 2 % lower) at low applied loads. However, as loading increased, the difference between the values magnifies to as much as 15 % at an applied load of 120 kN. The only other similarity between the numerical model and experimental results is the amount of embedment length mobilized, as both the numerical models and the physical test results used up the entirety of the embedded section of the bolt to distribute the load throughout the system. Generally, the numerical models predicted a much steeper exponential decay of strain across the embedded region of the bolt than what was physically witnessed. This difference is attributed to the numerical modelling program over estimating the efficiency of load transfer throughout the system. The rheological model used to represent the bolt-grout interface inadequately represents the change from frictional resistance to mechanical interlocking as the embedment length increases.

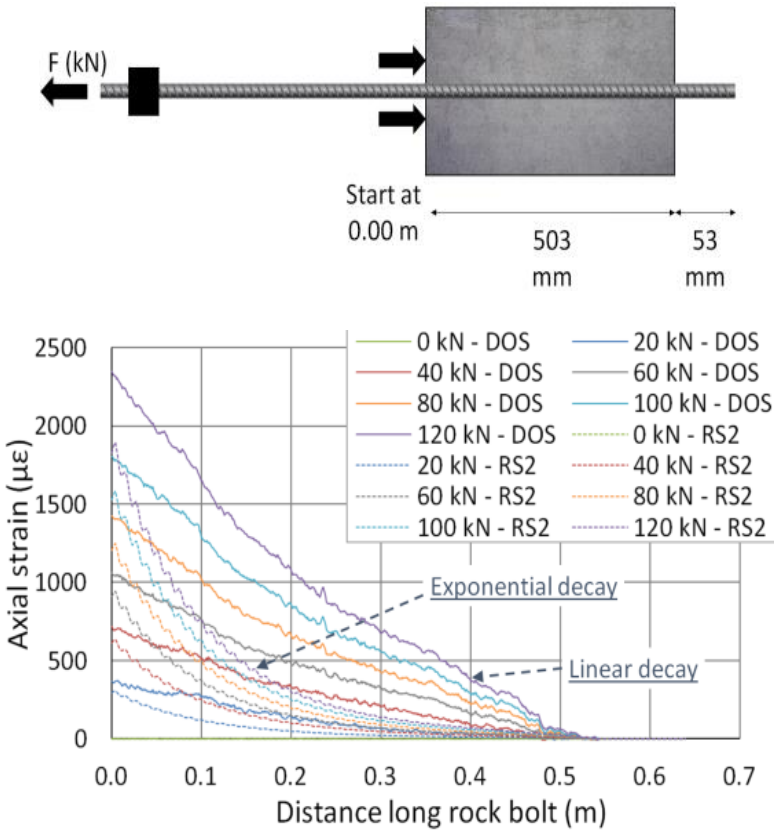

Figure 7.25: Numerical model strain profile results for specimen *f* (embedded bolt section only). Left; RS2 model with no ribs. Right; RS2 model with ribs

7.3.3 Resin Grout

The use of a resin-based grout instead of a cementitious grout generally attained higher load bearing capacities. This is shown in Figure 7.26, where the load displacement curves of two specimens that only differed in grouting material are shown. The cementitious grouted specimen was much stiffer than the resin grouted specimen. Additionally, the cementitious grouted specimen failed at roughly 40 kN whereas the resin grouted specimen failed at 44 kN. This increase in load bearing capacity witnessed with the use of resin-based grout is likely associated to the inherent stronger material properties of the resin in comparison to the cementitious grout, as covered in Chapter 4. No audible cracking sounds were

heard throughout loading of the resin samples. Accordingly, no radial splitting cracks developed within the grout or concrete up until failure of the system occurred. This is associated with the fact that the resin grout is stronger than the cementitious grout; therefore its tensile capacity was not reached at low applied loads. Accordingly, minimal dilation at the bolt-grout interface occurred. This lack of dilation made it possible for the mismatch between the grout and bolt ribs to efficiently transfer load from the bolt onto the grout and concrete. This built up load within the grout and concrete is what eventually caused the concrete cylinders of the resin samples to radially split.

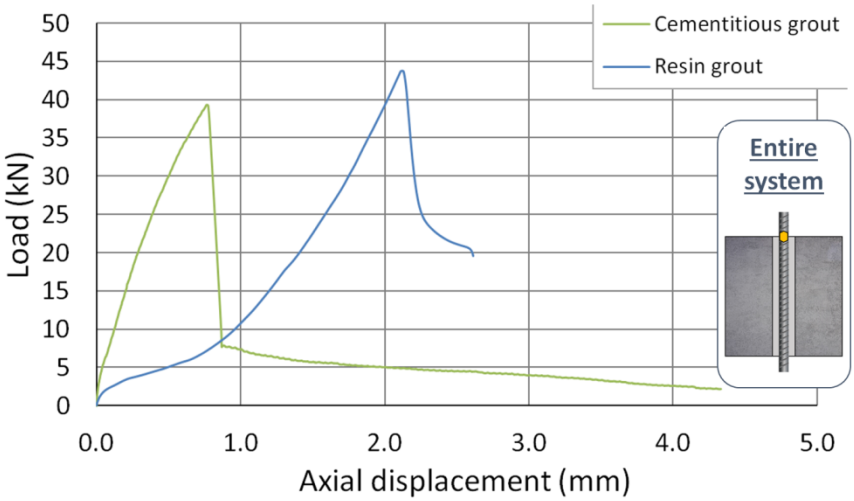

Figure 7.26: Load displacement curves for specimen *l* (cementitious grout) and specimen *k* (resin grout)

Additionally, it was noted that there were inherent difficulties in grouting the bolts with the use of the resin grout. The post testing analysis of specimen *n* proves this (Figure 7.27). Settling of the resin grout during curing caused a large portion of the bolt to remain decoupled after grouting was complete. The resin thinly encapsulated both the bolt and borehole annulus, leaving a gap in between the two surfaces. Accordingly, this encapsulation of the bolt and borehole wall led to a decrease in the effective embedment length of the specimen as seen in Figure 7.28.

Figure 7.27: Resin encapsulation of rebar and borehole wall

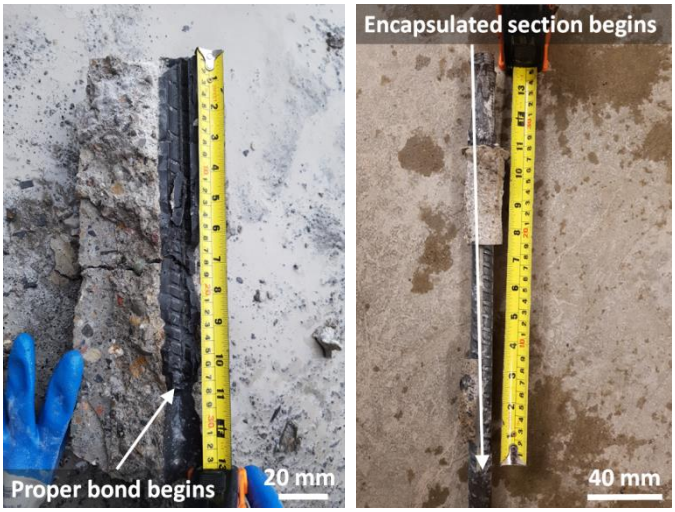

Figure 7.28: Effective embedment length of specimen *n*

7.3.4 Borehole Wall Preparation

All of the specimens tested had properly prepared borehole surfaces with the exception of two. As specimen *b* and *c* had improperly prepared borehole annulus, slipping at the toe end of the bolt began to take place almost as soon as loading commenced. As can be seen in Figure 7.29, the grout column of specimen *b* mobilized outside of the specimen borehole as loading continued. This is evidence that failure had occurred within the system at the grout-concrete interface. This failure is directly associated with the improper bonding surface present at the interface; a lesson learned onto itself. As the borehole was not properly prepared, there were not sufficient irregularities along the borehole annulus for the grout to move into and create an effective bond. In this regard, the borehole was a smooth surface as pictured in Figure 7.29. This meant that the entire load carrying capacity of the system was provided by the friction present at the grout-concrete interface. As soon as the shear strength of this surface was surpassed, a specific failure mechanism was initiated and the system was incapable of taking on further load as the frictional interface was incrementally and then fully mobilized. For specimen *c* (87 mm embedment length), the maximum load carrying capacity the system was able to withstand was 4.0 kN whereas specimen *b* (174 mm embedment length) was able to withstand 13 kN of load.

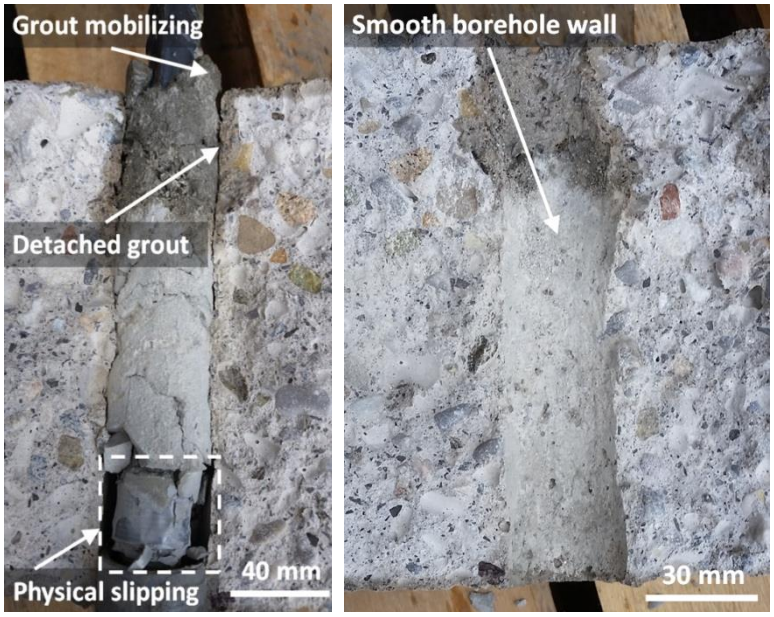

Figure 7.29: Specimen *b* post testing analysis

7.3.5 Borehole Diameter

It was generally found that utilizing a larger borehole diameter improved the load carrying capacity of the entire support system. Additionally, the response of the optical fibre attained a more pronounced exponential decay, in terms of the strain profiles, than samples with smaller diameter annuluses. This is seen in Figure 7.30. The specimen with a larger borehole diameter portrayed exponential decay of the strain profile whereas the specimen with the smaller diameter experienced a linear decay of the strain profiles. This indicates that there was more of a mechanical interlocking component of shear resistance present at the bolt-grout interfaces of specimens with larger boreholes. The larger borehole diameter specimens had a thicker grout layer surrounding the bolt. As such, the thicker grout made it possible for the system to withstand dilational cracks to a better degree than the tests performed on 31 mm diameter borehole concrete cylinders. Essentially, the radial splitting cracks had to propagate through a thicker grout layer. This enabled minimal dilation to take place at the bolt-grout interface which effectively maintained the bolt and grout coupled throughout loading. This made it possible for the mechanical interlocking component of shear resistance to be mobilized more effectively.

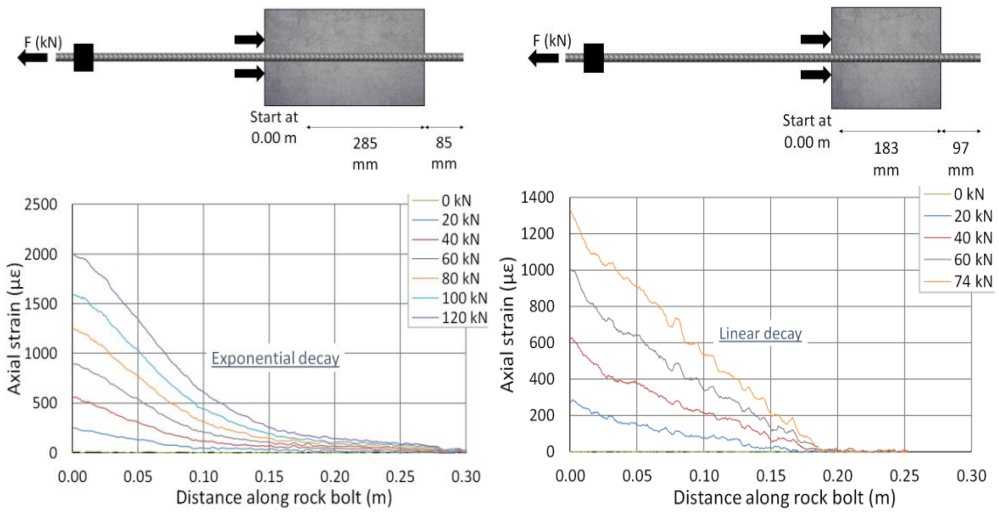

Figure 7.30: Detailed strain profile results (embedded bolt section only). Left; 41 mm borehole diameter. Right; 31 mm borehole diameter

7.3.6 Embedment Length

The embedment length of the specimens proved to be the factor that most significantly affected results. Generally, the load bearing capacity of the system increased as the embedment length increased. In addition, the increasing embedment length dominated the governing failure mechanism, as shorter embedment lengths had the concrete cylinder fail and the longer embedment length specimens had the steel bar fail in tension.

The axial stiffness of the support system as derived from the initial quasi linear region of the load displacement curve derived with conventional instrumentation, Rayleigh DOS, and the numerical models are seen in Table 7-1. The axial stiffness values from the DOS results are roughly 10 orders of magnitude larger than that of the results captured using conventional instrumentation. This result is expected as the conventional instrumentation captures the performance of all of the components within the support system working together whereas DOS simply captured the response of the bolt. Accordingly, the specimens modelled in RS2 had axial stiffness values in the same order of magnitude as those attained using DOS.

Table 7-1: Axial stiffness results for all tests

Test Group	Test	Embedment Length (mm)	Axial stiffness (kN/mm)				Normalized axial stiffness (kN/mm/m)			
			Conv. Instrumentation	DOS	RS2 - no ribs	RS2 - ribs	Conv. Instrumentation	DOS	RS2 - no ribs	RS2 - ribs
A	1	94	62	733	358	421	660	7798	3809	4479
	2	183	48	664	467	537	262	3628	2552	2934
	3	92	29	1063	-	-	315	11554	-	-
	4	78	21	978	-	-	269	12538	-	-
	5	245	54	386	482	569	220	1576	1967	2322
	6	174	-	868	-	-	-	4989	-	-
	7	87	-	834	-	-	-	9586	-	-
B	1	503	64	274	-	-	127	545	-	-
	2	540	35	157	493	558	65	291	913	1033
	3	1017	36	602	488	546	35	592	480	537
	4	879	33	219	-	-	38	249	-	-
	5	495	48	390	487	549	97	788	984	1109
	6	285	33	717	-	-	116	2516	-	-

There was little correlation between the axial stiffness values of the system, as captured by conventional instrumentation, and the embedment length of the specimens. However normalizing the axial stiffness values with respect to the embedment lengths changes this, as is seen in Figure 7.31. There seems to be an exponential decay correlation between this normalized stiffness and the embedment length. Taking a look at the axial stiffness values derived using DOS, it is clear that they generally tend to decrease as the embedment length increases. The normalized axial stiffness values portray the same exponential decay correlation with the embedment length of the specimens. These correlations are seen in Figure 7.32.

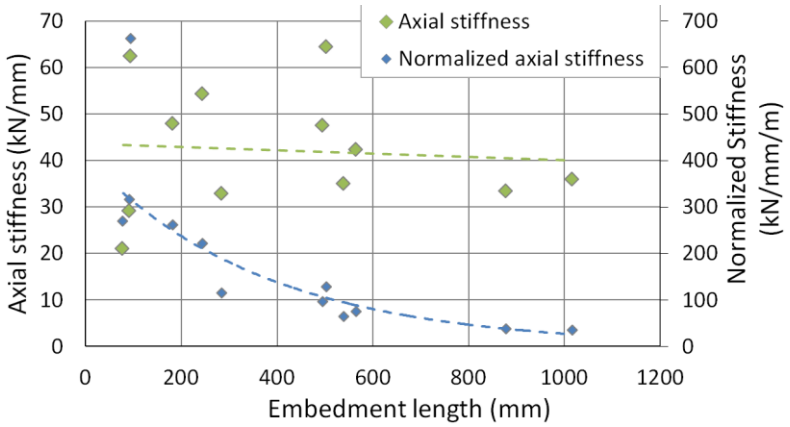

Figure 7.31: Axial stiffness results using conventional instrumentation

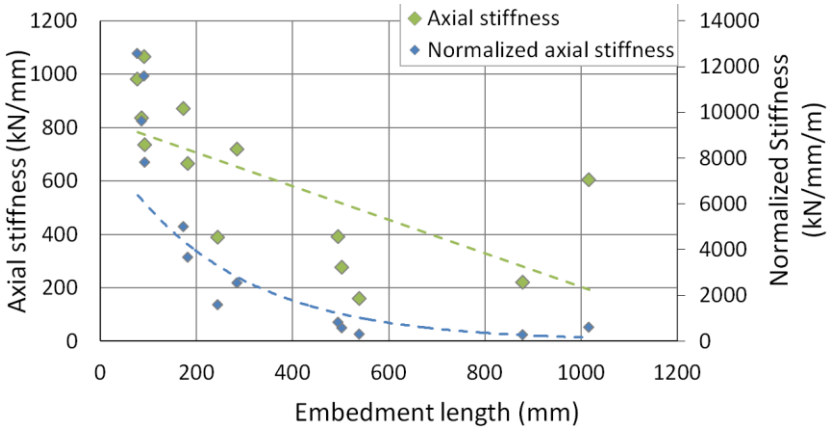

Figure 7.32: Axial stiffness results using Rayleigh DOS

7.4 Relevance to Research

This chapter presented a summary of the results attained from the laboratory pull-out tests performed within the RMCC structures laboratory. This included results captured with conventional instrumentation and Rayleigh DOS. Furthermore, the physical pull-out test results were compared to the numerical results.

8 Conclusions and Recommendations

8.1 Conclusion

A laboratory study was undertaken at the RMCC Structures Laboratory in order to analyse the response of axially loaded fully grouted rock bolts. 14 distinct specimens were tested under axial loading conditions with the use of Rayleigh DOS and conventional laboratory instrumentation. The results attained from this rigorous testing scheme have successfully addressed the spatial resolution limitations that were present in previous laboratory investigations. The use of the state of the art, strain measuring, distributed optical sensing technique alongside conventional laboratory instrumentation made it possible to study different loading mechanisms, failure mechanisms, and the effect of quality control issues on loading as associated to the support member. Overall, 3 different behaviours were observed throughout all of the specimens. These behaviours were governed by three distinct failure mechanisms. 10 numerical models were developed to replicate the axial loading conditions seen in the lab. These showed that the numerical modelling software has some limitations with respect to the rheological models used to simulate the interfaces. The importance of utilizing the adequate embedment length, as it pertains to the success of fully grouted rock bolts, was further highlighted. It was generally found that as the embedment length increases, the load bearing capacity of the support system increases. Conversely, as the embedment length increases, the stiffness of the system and bolt decreases exponentially. Accordingly, care must be taken when installing the support member *in situ*, as it is not always beneficial to simply use a longer embedment length. Design engineers should carefully study the predicted loading applied to the system as well as the amount of movement that is expected to make appropriate design decisions.

8.2 Major Contributions

The following are the major contributions of the author's research endeavour:

1. Continuous Strain Monitoring Technology Verified. Performed the first extensive testing campaign in order to study the response of axially loaded rock bolts with the use of a novel, state of the art strain measuring technology. 14 specimens were tested with the use of Rayleigh DOS. This optical technique made it possible to capture

complex support behaviour by continuously monitoring the strain profile along the length of rock bolt support members;

2. Quality Control. Verified the capability of the Rayleigh DOS technique to capture quality control issues associated with temporary support elements, accurately and consistently. The technique was able to capture the effect of grout inconsistencies, rebar ribs, and bolt-grout and grout-rock interface effects throughout all of the performed tests. This method can, therefore, be used for quality control purposes;
3. Suggested Improvements to Modelling Software. Successfully utilized the results attained from the optical technique to address the limitations of the industry standard numerical modelling software RS2 (Phase2.0). The 10 numerical models developed showcased the limitations of the available rheological models, and their inability to accurately model the bolt-grout interface interaction; and,
4. Critical Anchor Length Determination. Systematically determined the critical anchor length (*i.e.* critical embedment length) of the rock bolt support member under the loading conditions presented in this dissertation. This critical embedment length can used as a direct guideline by design engineers to minimize ground failures associated with the failure of rock bolts, as well as minimize project overhead costs seen with overdesign of the support member.

8.3 Future Recommendations

The results presented as part of this thesis have demonstrated the capability of the Rayleigh DOS technique to improve the insight that can be gained from laboratory investigations. It is therefore warranted that further work be done in the realm of temporary support elements with the use of this optical technique. The following recommendations are suggested:

1. It is recommended that laboratory investigations utilizing the optical technique are performed to study the response of other sorts of rock bolts under different loading conditions. The unparalleled spatial resolution provided by DOS should be utilized to further determine the specific support features and interaction parameters that are currently unknown in the industry;
2. It is recommended that a rigorous testing scheme be developed to further study the effect of radial confinement on the mechanistic

response of the bolt. Emphasis should be placed on the volumetric changes that occur at the different interfaces as these will affect the observed failure mechanism and the response of the support system;

3. It is recommended that multiple, similar tests be performed in order to compliment the results herein and provide further, statistically significant results, for similar test configurations;
4. It is recommended to develop the optical technique to capture the circumferential and lateral strains experienced by the concrete cylinder. This would give more insight into the effect and correlations seen with dilation at the different interfaces; and,
5. It is recommended to further use the results attained from future physical laboratory investigations to improve analytical and numerical techniques. It was shown as part of this investigation that although numerical models accurately predicted the response of the bolt in some areas, there still remain some significant differences in specific loading scenarios. Accordingly, future physical experimentation results should be back analysed to improve numerical and analytical models.

References

Ardiaca, D. H. (2009). Mohr-Coulomb parameters for modelling concrete structures. *Plaxis Bulletin 25*, pp. 12-15.

Azziz, N., & Webb, B. (2003). Study of load transfer capacity of bolts using short encapsulation push tests. *Coal Operators' Conference*, (pp. 72-80).

Bao, X., & Chen, L. (2012). Recent progress in distributed fiber optic sensors. *Sensors*, 8601-8639.

Barley, A. D., & Windsor, C. R. (2000, November). Recent advances in ground anchor and ground reinforcement technology with reference to the development of the art. *ISRM International Symposium.* International Society for Rock Mechanics.

Barnoski, M. K., Rourke, M. D., Jensen, S. M., & Melville, R. T. (1977). Optical time domain reflectometer. *Applied Optics*, 2375-2379.

Barrias, A., Casas, J. R., & Villalba, S. (2016). A Review of Distributed Optical Fiber Sensors for Civil Engineering Applications. *Sensors*, 748-813.

Barton, N. (2012). Defining NMT as part of the NATM SCL debate.

Barton, N., Lien, R., & Lunde, J. (1974). Engineering classification of rock masses for the design of tunnel support. In *Rock Mechanics* (pp. 189-239).

Bawden, W. F., & Lausch, P. (2000). The use of SMART cable bolt instruments toward the design and design optimization of underground rock support systems. *Proceedings of the 53rd Canadian Geotechnical Conference*, (pp. 315-323).

Benmokrane, B., Chennouf, A., & Mitri, H. S. (1995). Laboratory Evaluation of Cement-Based Grouts and Grouted Rock Anchors. *International Journal of Rock Mechanics & Mining Sciences, Vol. 32 (7)*, 633-642.

Bieniawski, Z. T. (1993). Classification of rock masses for engineering: The RMR system and future trends. In J. A. Hudson, *Comprehensive Rock Engineering* (pp. 553-573). New York: Pergamon Press.

Blanco Martin, L. (2012). *Theoretical and experimental study of fully grouted rockbolts and cablebolts under axial loads.* France: MINES-ParisTech.

Brady, B. H., & Brown, E. T. (2004). *Rock Mechanics for Underground Mining.* New York: Kluwer Academic Publishers.

Campbell, R., & Mould, R. J. (2005). Impacts of gloving and un-mixed resin in fully encapsulated roof bolts on geotechnical design assumptions and strata control in coal mines. *International Journal of Coal Geology, 64(1)*, 116-125.

Cao, C., Jan, N., Ren, T., & Naj, A. (2013). A study of rock bolting failure modes. *International Journal of Mining Science and Technology, 23(1)*, 79-88.

(2007). Chapter 3: Sensors. In H. Zumbahlen, *Basic linear design.* Analog Devices.

Cruz, D., Forbes, B., & Vlachopoulos, N. (2016). The Geo-Mechanical Response of Axially Loaded Rock Bolts using Fiber Optic Technology. *XV*

Colombian Geotechnical Congress & II International Specialized Conference of Soft Rocks.

Dakin, J. (1990). *The distributed fibre optic sensing handbook.* Springer-Verlag.

Deere, D. U., Hendron, A. J., Patton, F. D., & Cording, E. J. (1967). Design of surface and near surface construction in rock. *8th U.S. Symposium on Rock Mechanics: Failure and breakage of rock.* New York: Society of Mining Engineers, American Institute of Mining, Metallurgical, and Petroleum Engineers.

DSI. (2009). *Pourable resin grout.*

Dunham, R. (1976). Anchorage tests on strain-gauged resin bonded bolts. *Tunnels and Tunneling*, 73-76.

Fabjanczyk, M. W., & Tarrant, G. C. (1992). Load transfer mechanisms in reinforcing tendons. *11th International Conference on Ground Control in Mining*, (pp. 212-219). Wollongong, New South Wales, Australia.

Farmer, I. W. (1975). Stress Distribution along a Resin Grouted Rock Anchor. *Int. Journal of Rock Mechanics and Mining Sciences & Geomechanics*, 347-351.

FBGS. (2016). *FBGS.* Retrieved June 8, 2016, from FBG - FIBER BRAGG GRATING PRINCIPLE: http://www.fbgs.com/technology/fbg-principle/

Forbes, B. (2015). *The application of distributed optical sensing for monitoring support in underground excavations.* Kingston: Department of Geological Sciences & Geotechnical Engineering.

Forbes, B., Vlachopoulos, N., Oke, J., & Hyett, A. J. (2014). The Application of Distributed Optical Sensing for Monitoring Temporary Support Schemes. *GeoRegina.* Regina, SK: Canadian Geotechnical Society.

Freeman, T. J. (1978). The behaviour of fully-bonded rock bolts in the Kielder experimental tunnel. *Tunnels & Tunneling Internaional*, 10(5).

Fuller, P. G., & Cox, R. H. (1975). *Mechanics of load transfer from steel tendons to cement based grout.* Division of Applied Geomechanics, CSIRO.

Gifford, D. K., Soller, B. J., Wolfe , M. S., & Froggatt, M. E. (2005). Distributed fiber-optic temperature sensing using Rayleigh backscatter. *31st European Conference on Optical Communications*, (pp. 511-512). Glasgow, UK.

Glisic, B. (2013). Distributed fiber optic sensing technologies and applications - an overview. *American Concrete Institute Special Publication*, 1-18.

Goris, J. M. (1990). Laboratory evaluation of cable bolt supports. *92nd Annual General Meeting of the CIM.*

Haas, C. J. (1975). Shear resistance of rock bolts. *104th Annual Meeting of American Institute of Mining, Metallurgical and Petroleum Engineers*, (pp. 32-40).

Habel, W. R., & Krebber, K. (2011). Fiber-optic sensor applications in civil and geotechnical engineering. *Photonic Sensors*, 268-280.

He, L., An, X. M., & Zhao, Z. Y. (2015). Fully Grouted Rock Bolts: An Analytical Investigation. *Rock Mechanics and Rock Engineering, 48(3)*, 1181-1196.

Hill, K. O., Fujii, Y., Derwyn, C., & Kawasaki, B. S. (1978). Photosensitivity in Optical Fiber Waveguides: Application to Reflective Filter Waveguide. *Applied Physics Letters*, 647-649.

Hoek, E. (1994). Strength of rock and rock masses. *International Society of Rock Mechanics New Journal*, 4-16.

Hoek, E. (2007). *Practical Rock Engineering.* North Vancouver: Rocscience Inc.

Hoek, E., & Wood, D. F. (1987). Support in Underground Hard Rock Mines. *Underground Support Systems*, 1-6.

Hoek, E., Kaiser, P. K., & Bawden, W. F. (2000). *Support of underground excavations in hard rock.* CRC Press.

Horiguchi, T., & Tateda, M. (1989). BOTDA-Nondestructive measurement of single-mode optical fiber attenuation characteristics using Brillouin interaction. *Journal of lightwave technology*, 1170-1176.

Hyett, A. J., Bawden, W. F., & Reichert, R. D. (1992). The effect of rock mass confinement on the bond strength of fully grouted cable bolts. *International Journal of Rock Mechanics and Mining Sciences & Geomechanics, 29(5)*, 503-524.

Hyett, A. J., Bawden, W. F., Macsporran, G. R., & Moosavi, M. (1995). A constitutive law for bond failure of fully-grouted cable bolts using a modified Hoek cell. *International Jornaul of Rock Mechanics and Mining Sciences & Geomechanics, 32(1)*, 11-36.

Hyett, A. J., Forbes, B., & Spearing, S. (2013). Enlightening Bolts: Using Distributed Optical Sensing to Measure the Strain Profile along Fully Grouted Rock Bolts. *Proceedings of the 32nd International Conference on Ground Control in Mining*, (pp. 107-112). Morgantown, VW.

Jing, L. (2003). A review of techniques, advances and outstanding issues in numerical modelling for rock mechanics and rock engineering. *International Journal of Rock Mechanics & Mining Sciences*, 283-353.

Johnston, J. L., & Cox, D. J. (1993). *Instrumentation procedures for fully grouted rock bolts.* United States: Information Circular - United States, Bureau of Mines.

Kaiser, P. K., Yazici, S., & Nose, J. (1992). Effect of stress change on the bond strength of fully grouted cables. *International Journal of Rock Mechanics and Mining Sciences & Geomechanics, 29(3)*, 293-306.

Kikuchi, K., Naito, T., & Okoshi, T. (1988). Measurement of Raman scattering in single-mode optical fiber by optical time-domain reflectometry. *IEEE journal of quantum electronics*, 1973-1975.

Kilic, A., Yasar, E., & Celik, A. G. (2002). Effect of grout properties on the pull-out load capacity of fully grouted rock bolt. *Tunneling and Underground Space Technology, 17(4)*, 355-362.

Kurashima, T., Horiguchi, T., & Tateda, M. (1990). Distributed-temperature sensing using stimulated Brillouin scattering in optical silica fibers. *Optics Letters*, 1038-1040.

Kwon, I. B., Baik, S. J., Im, K., & Yu, J. W. (2002). Development of fiber optic BOTDA sensor for intrusion detection. *Sensors and Actuators*, 77-84.

Lanticq, V., Bourgeois, E., Magnien, P., Dieleman, L., Vinceslas, G., Sang, A., & Delepine-Lesoille, S. (2009). Soil-embedded optical fiber sensing cable interrogated by Brillouin optical time-domain reflectometry (B-OTDR) and optical frequency-domain reflectometry (OFDR) for embedded cavity detection and sinkhole warning system. *Measurement Science and Technology*, 034018.

Li, C. (2007). A Practical Problem with Threaded Rebar Bolts in Reinforcing Largely Deformed Rock Masses. *Rock Mechanics and Rock Engineering, 40*, 519-524.

Li, C., & Stillborg, B. (1999). Analytical models for rock bolts. *International Journal of Rock Mechanics and Mining Sciences*, 1013-1029.

López-Higuera, J. M. (1998). *Optical sensors.* Universidad de Cantabria.

López-Higuera, J. M., Cobo, L. R., Incera, A. Q., & Cobo, A. (2011). Fiber optic sensors in structural health monitoring. *Journal of Lightwave Technology*, 587-608.

Luna Innovations Inc. (2016, February 24). Retrieved from Optical Distributed Sensor Interrogator, User guide (Revision 3.0): http://lunainc.com/wp-content/uploads/2014/05/ODiSI-B-UGv3.0.pdf

Mark, C. (2000). Design of roof bolt systems. *New Technology for Coal Mine Roof Support, Proceedinds of the NIOSH Open Industry Briefing, NIOSH IC*, 23-42.

Mark, C., Compton, C. S., Oyler, D. C., & Dolinar, D. R. (2002). Anchorage pull testing for fully grouted roof bolts. *Proceedings of the 21st International Conference on Ground Control in Mining* (pp. 105-113). Morgantown, VW: West Virginia University.

Micron Optics Inc. (2016, March 13). *Sensing Instrumentation and Software: Enlight, User guide.* Retrieved from http://www.micronoptics.com/download/manual-pdf/

Mitri, H. (2011). Evaluation of Rock Support Performance through Instrumentation and Monitoring of Bolt Axial Load. *11th Underground Coal Operators' Conference* (pp. 136-140). University of Wollongong & the Australasian Institute of Mining and Metallurgy.

National Instruments. (2011, June 30). *Overview of Fiber Optic Sensing Technologies.* Retrieved June 16, 2016, from National Instruments: http://www.ni.com/white-paper/12953/en/

Peng, S. S., & Tang, D. Y. (1984). Roof bolting in underground mining: a state-of-the-art review. *International Journal of Mining Engineering, 2(1)*, 1-42.

Posey, J. R., Johnson, G. A., & Vohra, S. T. (2000). Strain sensing based on coherent Rayleigh scattering in an optical fibre. *Electronic Letters*, 1.

Reichert, R. D. (1991). *A laboratory and field investigation of the major factors influencing bond capacity of grouted cable bolts.* Kingston, Ontario, Canada: Master of Science Thesis, Queen's University.

Ren, F. F., Yang, Z. J., Chen, J. F., & Chen, W. W. (2010). An analytical analysis of the full-range behaviour of grouted rockbolts based on a tri-linear bond-slip model. *Construction and Building Materials, 24(3)*, 361-370.

RocScience. (2016). Bolt Formulation. In *Phase2 Theory*. Retrieved from RocScience.

Serbousek, M. O., & Signer, S. P. (1987). *Linear load transfer mechanics of fully grouted roof bolts.* US Dept. of the Interior, Bureau of Mines.

Signer, S. P. (1990). *Field verification of load-transfer mechanics of fully grouted roof bolts.* Pittsburgh: Bureau of Mines.

Soller, B. J., Wolfe, M., & Froggatt, M. E. (2005). Polarization resolved measurement of Rayleigh backscatter in fiber-optic components. *Optical Fiber Communication Conference and Exposition and The National Fiber Optic Engineers Conference.* Anaheim, CA.

Stillborg, B. (1984). Experimental investigation of steel cables for rock reinforcement in hard rock. Lele Tekniska Universitet.

Stillborg, B. (1986). *Professional Users Handbook for Rock Bolting.* Trans Tech Publications.

Stille, H. (1992). Keynote lecture: Rock support in theory and practice. *International Symposium on Rock Support (Rock Support in Mining and Underground Construction, SUdbury, Canada)*, (pp. 421-438).

Tepfers, R. (1979). Cracking of concrete cover along anchored deformed reinforcing bars. *Magazine of Concrete Research, 31(106)*, pp. 3-12.

Thévenaz, L., Facchini, M., Fellay, A., Robert, P., Inaudi, D., & Dardel, B. (1999). Monitoring of large structure using distributed Brillouin fibre sensing. *13th International Conference on Optical Fiber Sensors* (pp. 345-348). Society of Photo-Optical Instrumentation Engineers.

Thomas, R. (2013). The load transfer properties of post-groutable cable bolts used in the Australian coal industry. *4(15)*.

Tincelin, E., & Fine, J. (1991). *Memento du boulonnage.* Ecole des Mines de Paris.

Udd, E., & Spillman, W. B. (2011). *Fiber optic sensors.* Hoboken, New Jersey: John Wiley & Sons INC.

Venghaus, H. E. (2006). *Wavelength Filters in Fibre Optics.* Springer.

Vlachopoulos, N. (2009). *Back Analysis of a Tunelling Case Study in Weak Rock of the Alpine System in Northern Greece: Validation and Optimization of Design Analysis Based on Ground Characterization and Numerical Simulation.* Kingston, Canada: Department of Geology and Geological Engineering, Queen's University.

Windsor, C. R. (1997). Rock reinforcement systems. *International Journal of Rock Mechanics and Mining Sciences, 34(6)*, 919-951.

Windsor, C. R. (2004). A review of long, high capacity reinforcing systems used in rock engineering. *Proceedings of the 5th International Sumposiumon Ground Support* (pp. 17-41). Perth: CRC Press.

Windsor, C. R., & Thompson, A. G. (1993). Rock reinforcement - technology, testing, design and evaluation. *Comprehensive Rock Engineering*, 451-84.

APPENDIX A

Compiled Material Test Results

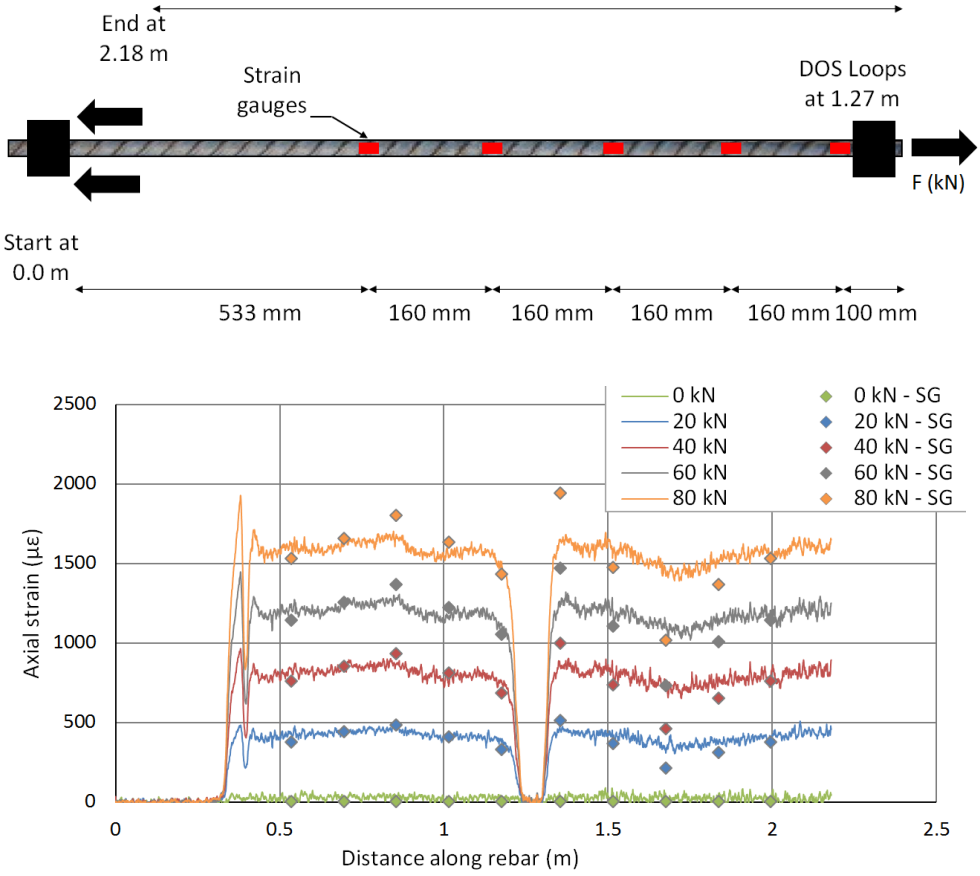

Figure A.1: Re-bar tensile test results for test # 2. Upper; Configuration. Lower; SG and DOS strain profile along re-bar length (SG results in diamonds)

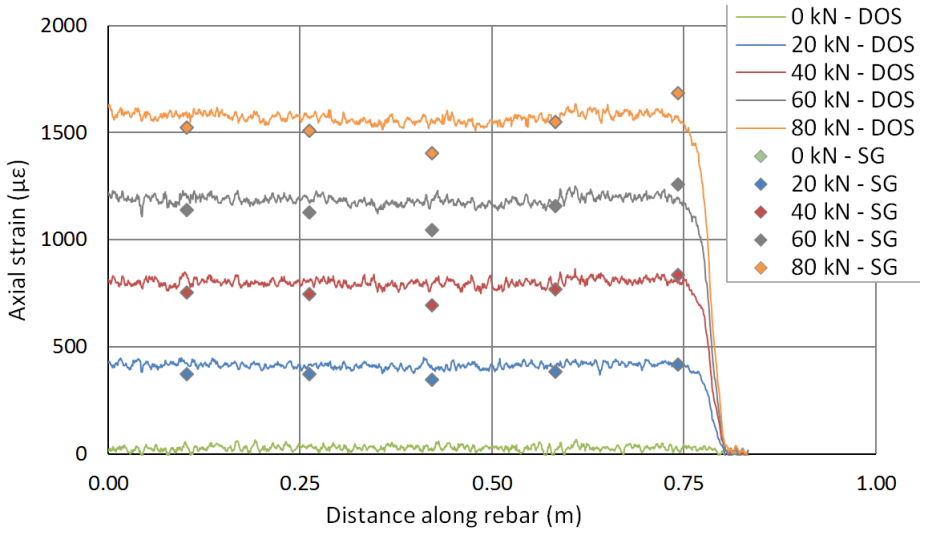

Figure A.2: SG and DOS strain profile final results for tensile test # 2 (SG results in diamonds)

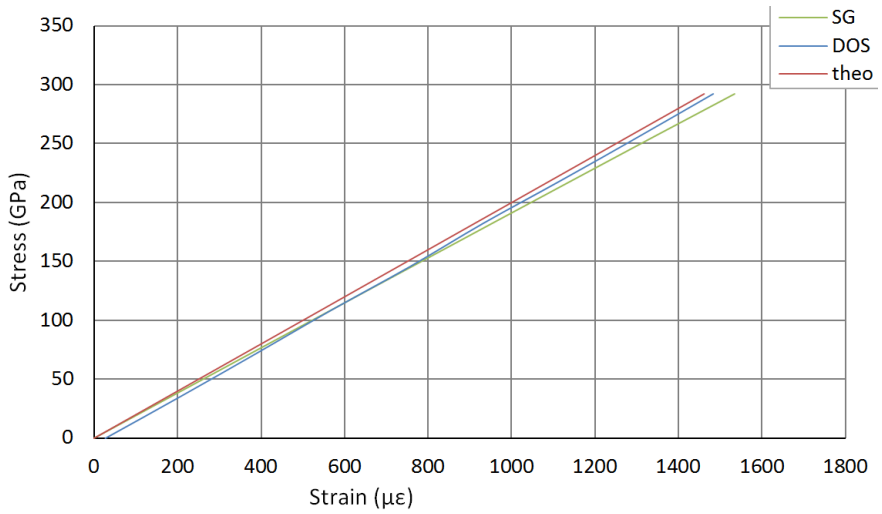

Figure A.3: Stress-strain results for tensile test # 2

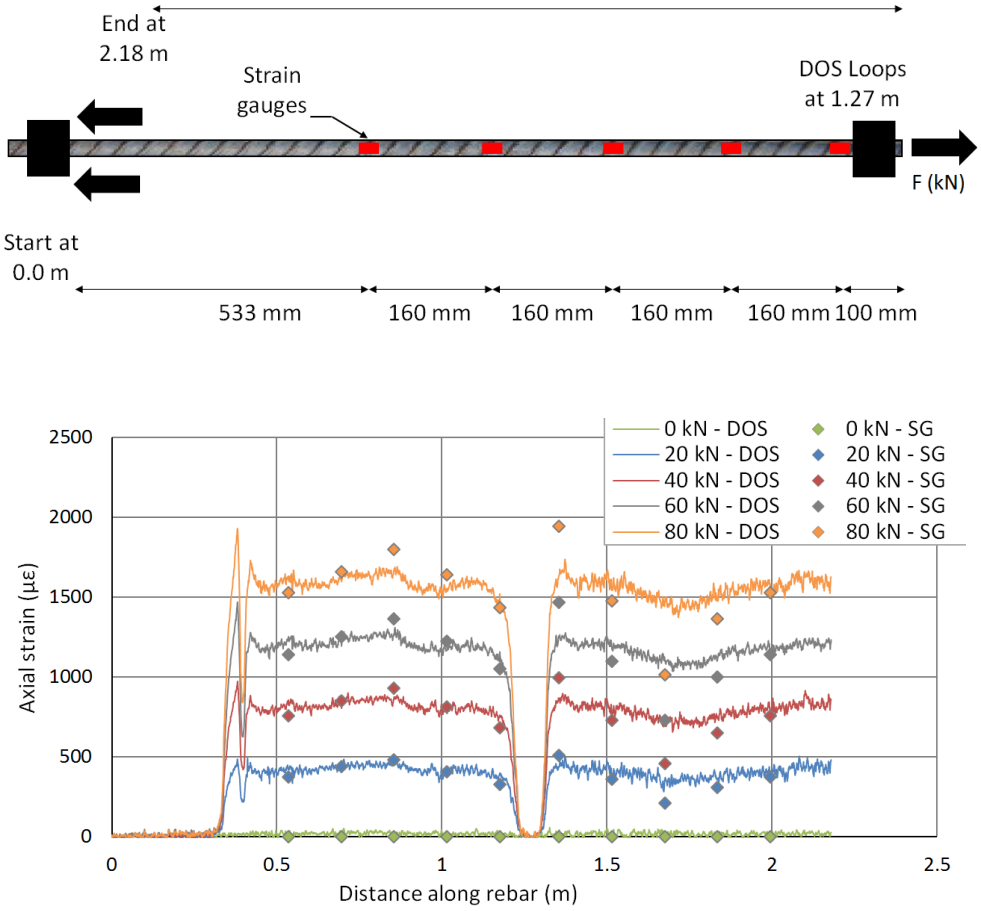

Figure A.4: Re-bar tensile test results for test # 3. Upper; Configuration. Lower; SG and DOS strain profile along re-bar length (SG results in diamonds)

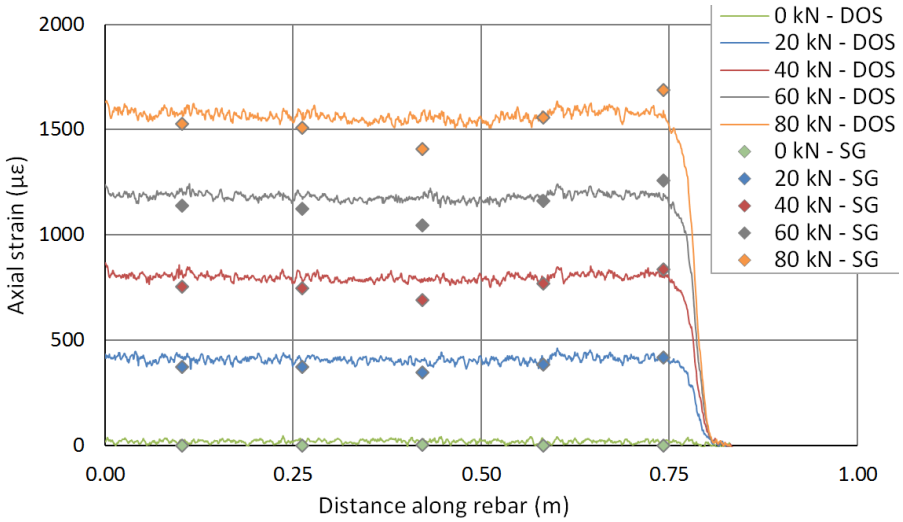

Figure A.5: SG and DOS strain profile final results for tensile test # 3 (SG results in diamonds)

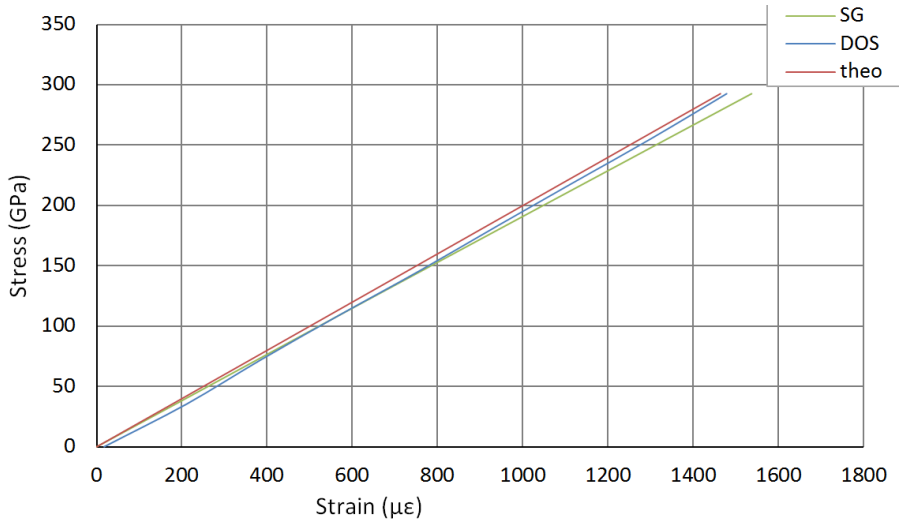

Figure A.6: Stress-strain results for tensile test # 3

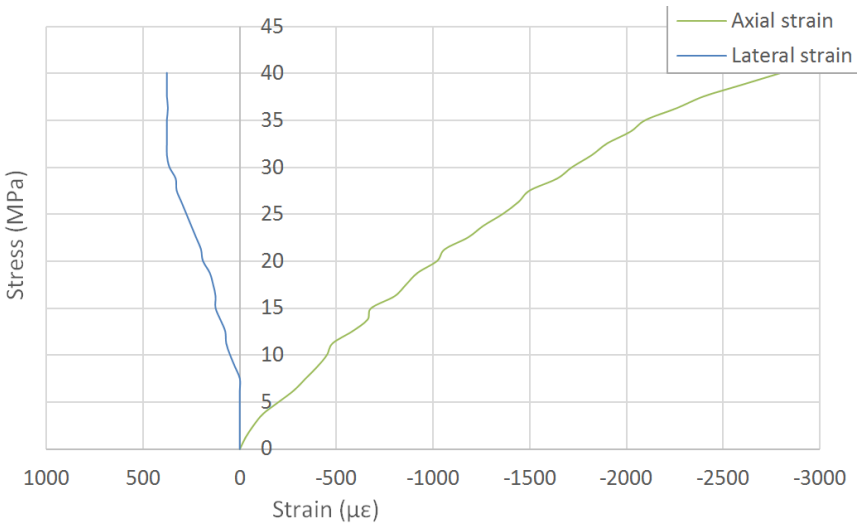

Figure A.7: Stress-strain results for concrete pour 1 test a (P1-a)

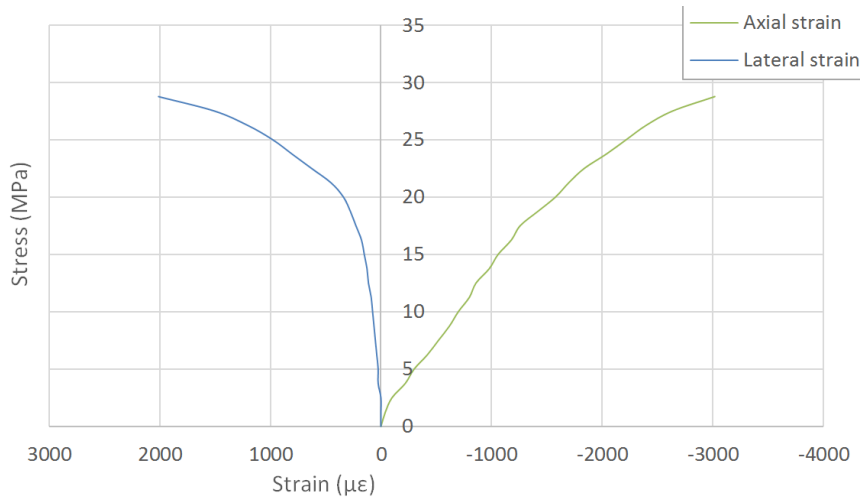

Figure A.8: Stress-strain results for concrete pour 2 test a (P2-a)

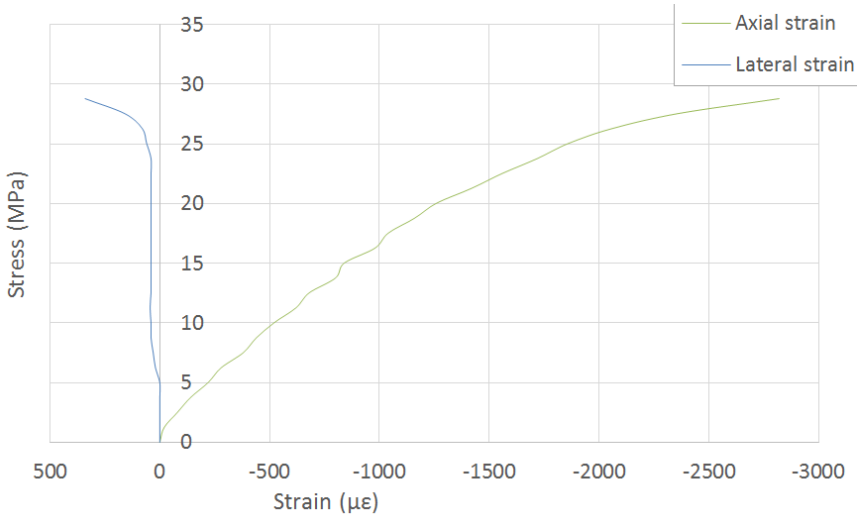

Figure A.9: Stress-strain results for concrete pour 2 test b (P2-b)

Table A-1: Preliminary material compression test results

Test specimen	Dia. (mm)	Mass (g)	Length (mm)	CSA (mm^2)	Max. Load (kN)	UCS (MPa)	E (MPa)	v
P1-a	100.3	3582.1	199.7	7906.5	161.4	20.4	16800	0.24
P1-b	101.0	3401.2	187.0	8011.8	203.6	25.4	-	-
P2-a	101.0	3576.7	191.0	8011.8	238.7	29.8	15900	0.14
P2-b	101.0	3516.1	189.8	8011.8	237.4	29.6	14300	0.14
CG-a	100.8	2911.1	189.7	7985.5	311.2	39.0	8200	0.14
CG-b	100.7	2870.9	187.8	7959.1	341.5	42.9	-	-
RG-a	100.1	2500.1	195.6	7875.0	300.5	35.0	7700	0.14

Table A-2: Preliminary material indirect tensile test results

Test specimen	Dia. (mm)	Mass (g)	Length (mm)	CSA (mm^2)	Max. Load (kN)	STS (MPa)
P1-c	100.5	3558.0	199.2	7938.0	82.5	2.6
P1-d	100.7	3450.2	189.5	7959.1	90.1	3.0
P2-c	100.8	3529.6	190.2	7985.5	95.7	3.2
P2-d	100.8	3484.7	188.2	7985.5	110.1	3.7
CG-c	100.7	2900.3	189.3	7959.1	54.9	1.8
RG-b	100.7	2900.3	189.3	7959.1	54.9	1.8

APPENDIX B

Compiled Pull-Out Test Results

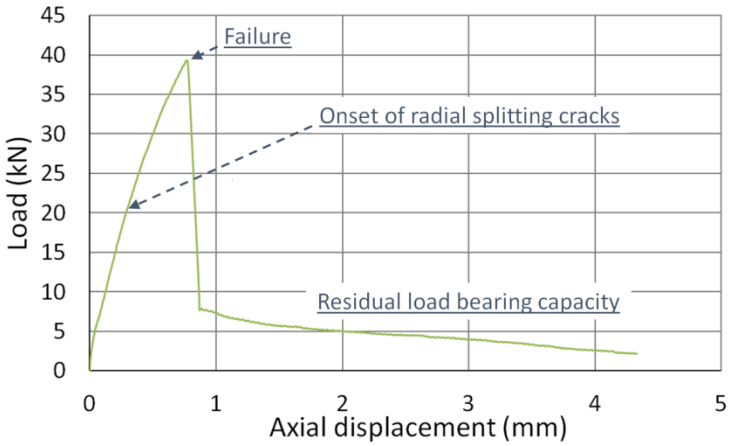

Figure B.1: Load displacement curve for specimen *l*

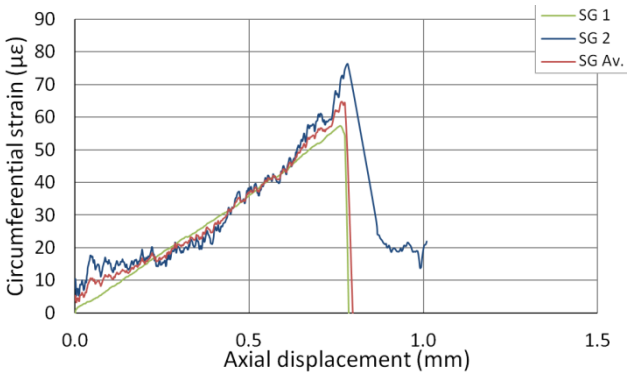

Figure B.2: Specimen *l* strain gauge results

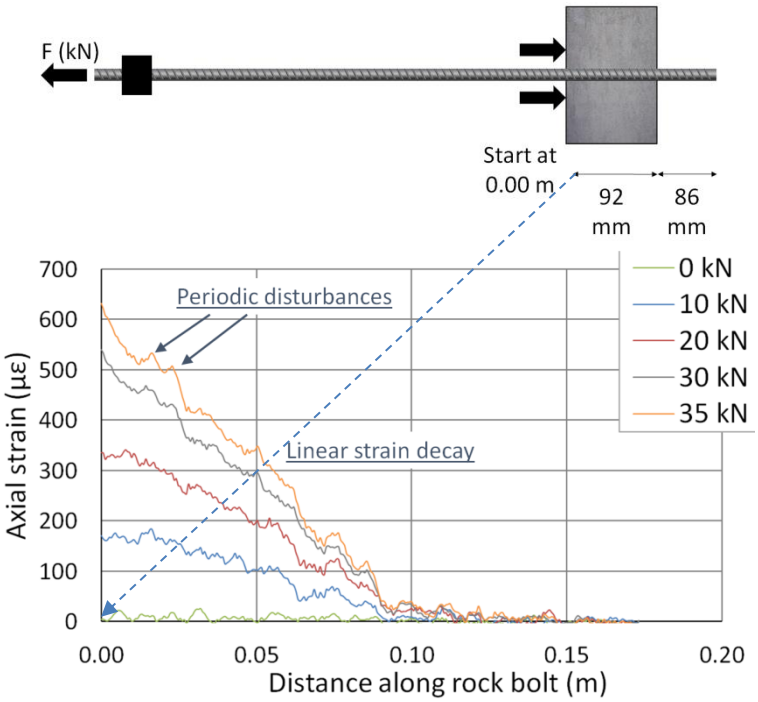

Figure B.3: Strain profile results for specimen *l* (embedded bolt section only)

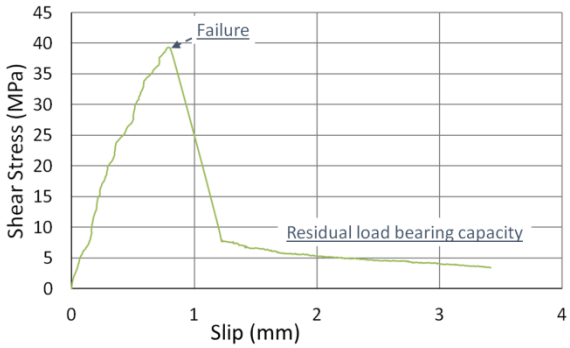

Figure B.4: Shear stress slip curve for specimen *l*

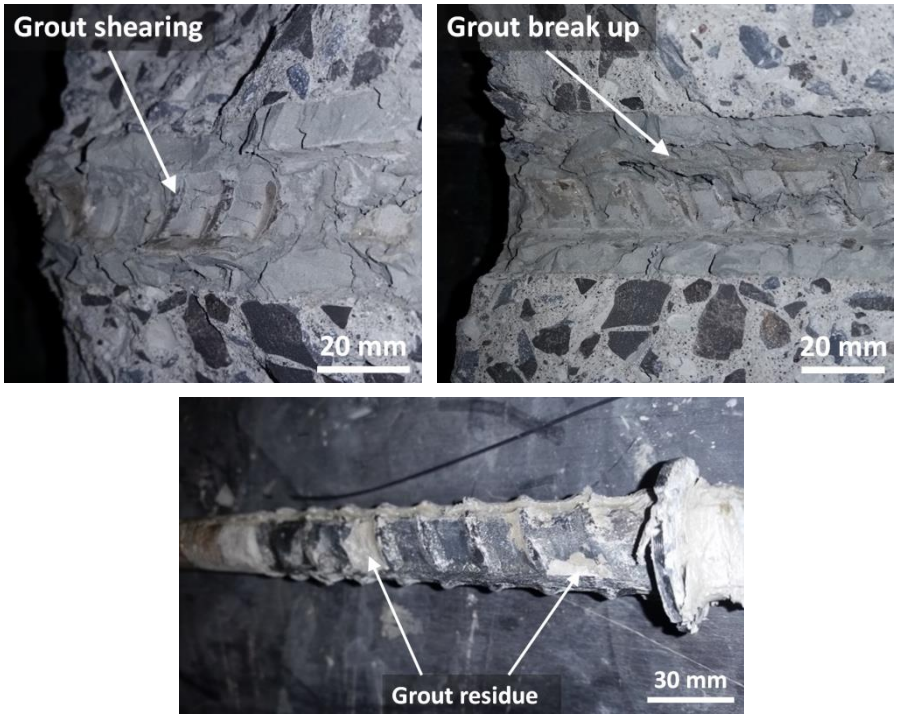

Figure B.5: Specimen *l* post testing analysis

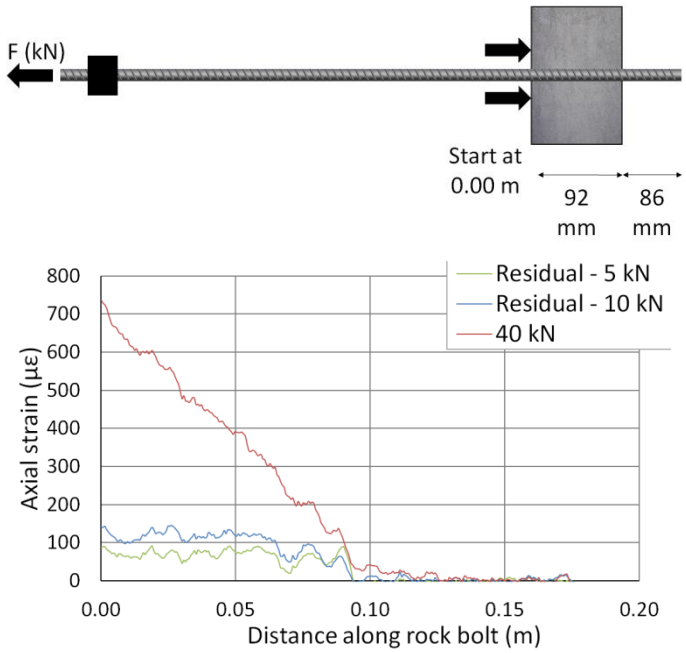

Figure B.6: Strain profile results for specimen *l* post failure (embedded bolt section only)

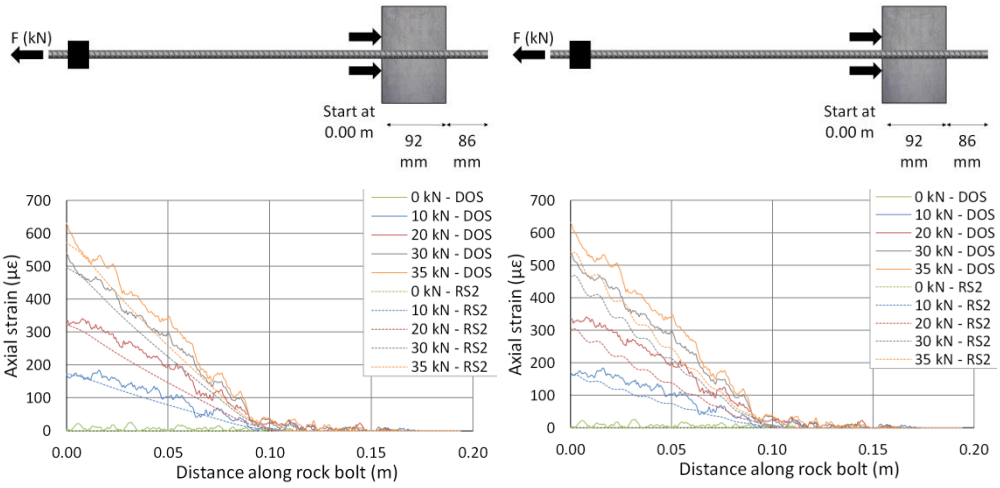

Figure B.7: Numerical model strain profile results for specimen *l* (embedded bolt section only). Left; RS2 model with no ribs. Right; RS2 model with ribs

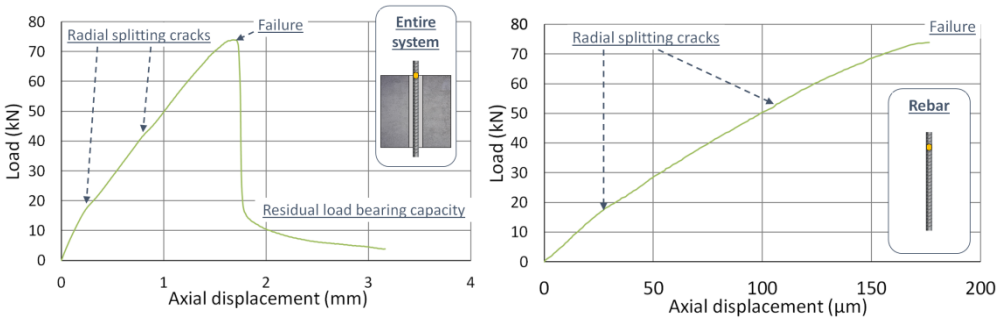

Figure B.8: Load-displacement curves for specimen *m*. Left; Support system response (conventional instrumentation). Right; Rebar response (Rayleigh DOS)

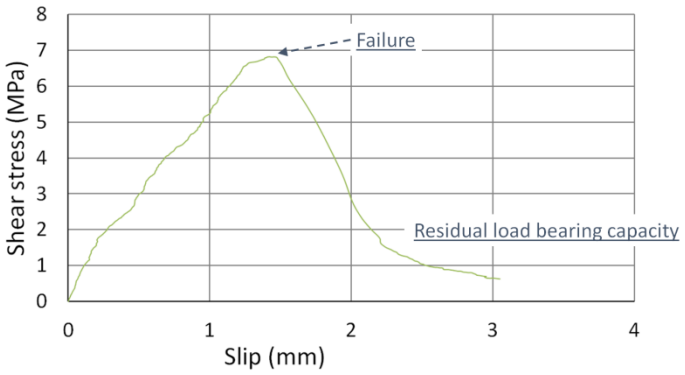

Figure B.9: Shear stress – slip curve for specimen *m*

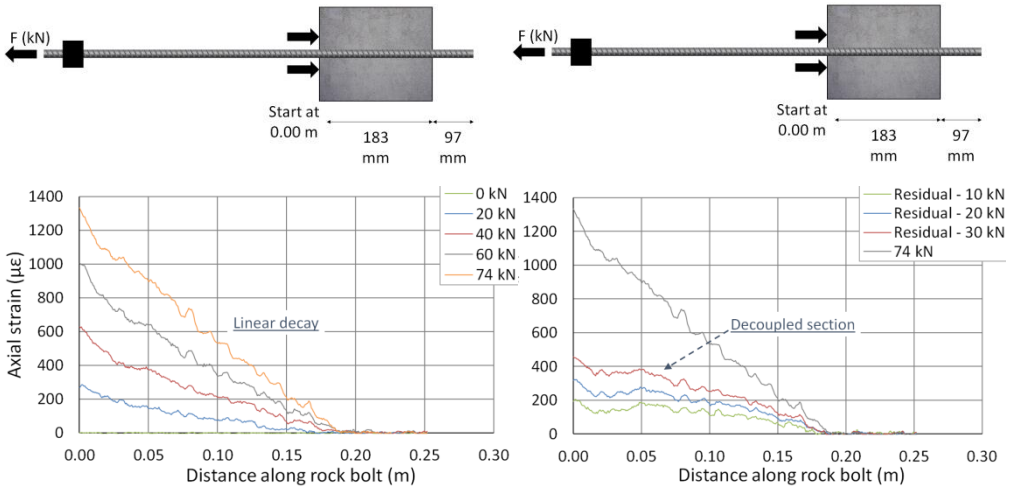

Figure B.10: DOS strain profile results for specimen *m* (embedded bolt section only). Left; Pre failure. Right; Post failure

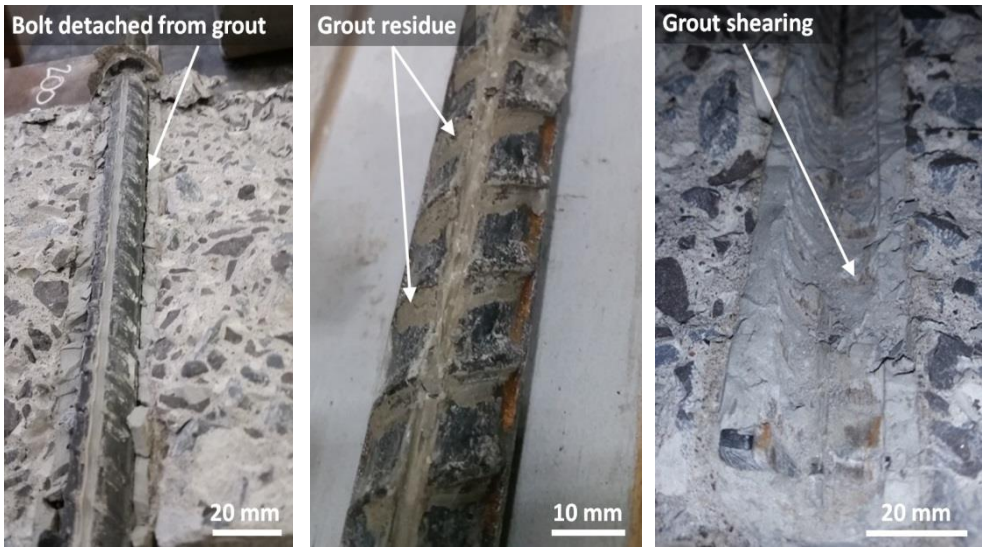

Figure B.11: Specimen *m* post testing analysis

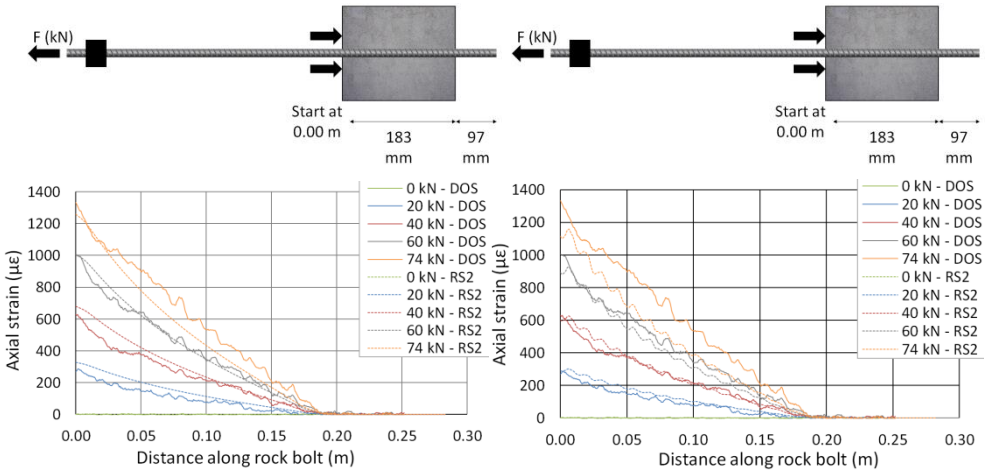

Figure B.12: Numerical model strain profile results for specimen *m* (embedded bolt section only). Left; RS2 model with no ribs. Right; RS2 model with ribs

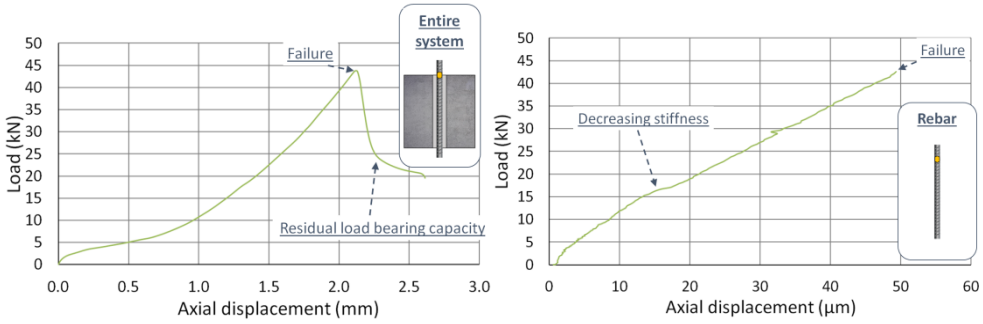

Figure B.13: Load-displacement curve for specimen *k*. Left; Support system response. Right; Rebar response

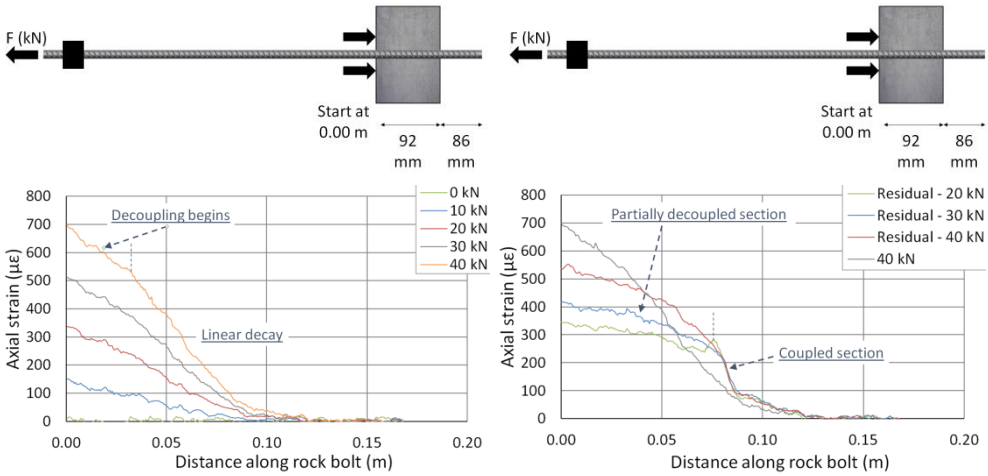

Figure B.14: DOS strain profile results for specimen *k* (embedded bolt section only). Left; Pre failure. Right; Post failure

Figure B.15: Specimen *k* post testing analysis

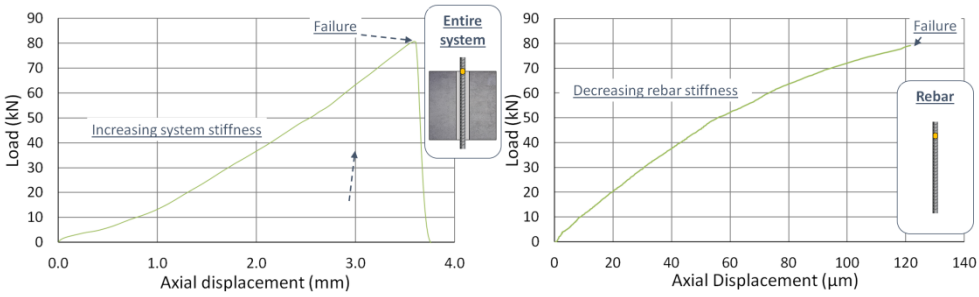

Figure B.16: Load-displacement curve for specimen *i*. Left; Support system response. Right; Rebar response

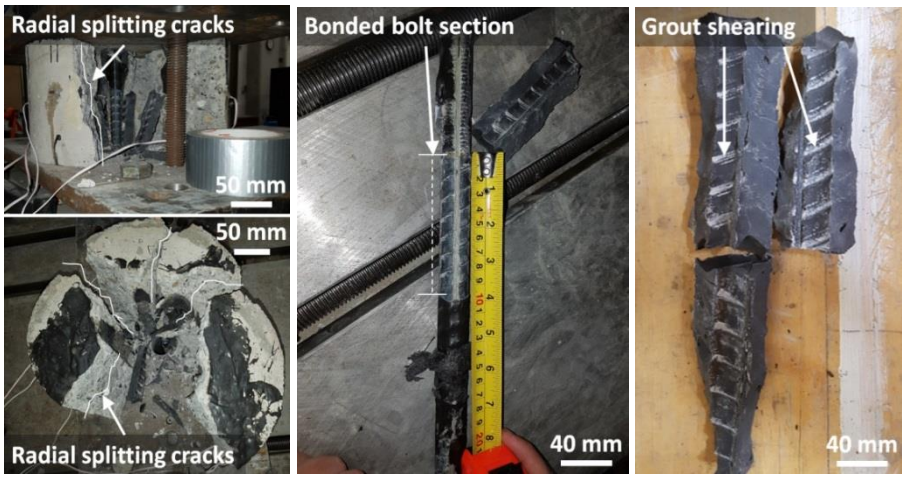

Figure B.17: Specimen *i* post testing analysis Left; Radial splitting of concrete cylinder and grout. Center; Bonded section of rebar. Right; Intact grout

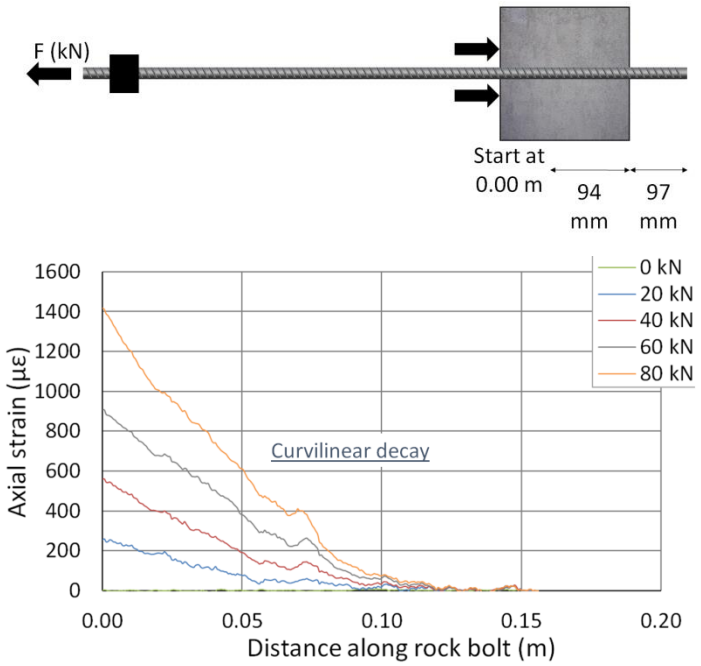

Figure B.18: DOS strain profile results for specimen *I* (embedded bolt section only)

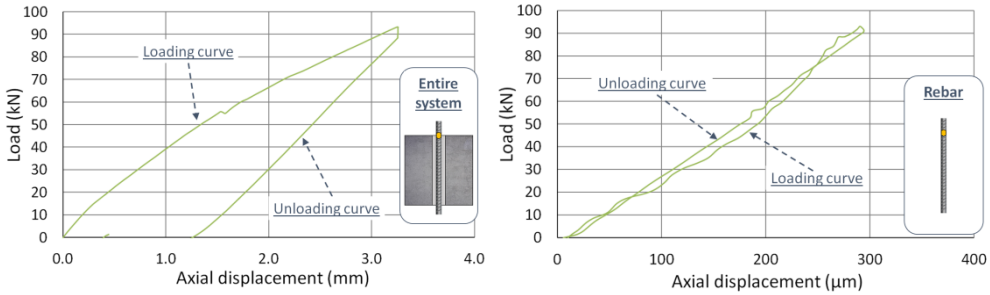

Figure B.19: Load-displacement curve for specimen *e*, load-unload test. Left; Support system response. Right; Rebar response

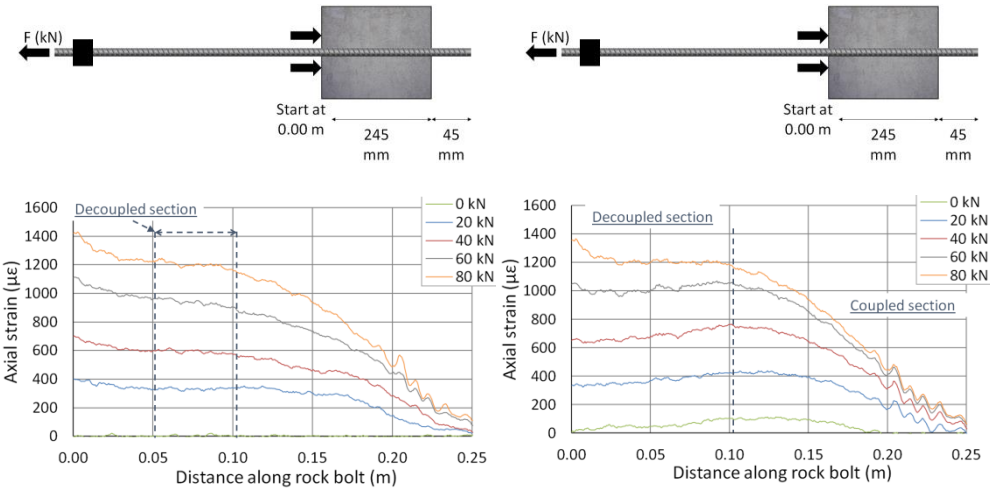

Figure B.20: DOS strain profile results for specimen *e*, load-unload test (embedded bolt section only). Left; Loading. Right; Unloading

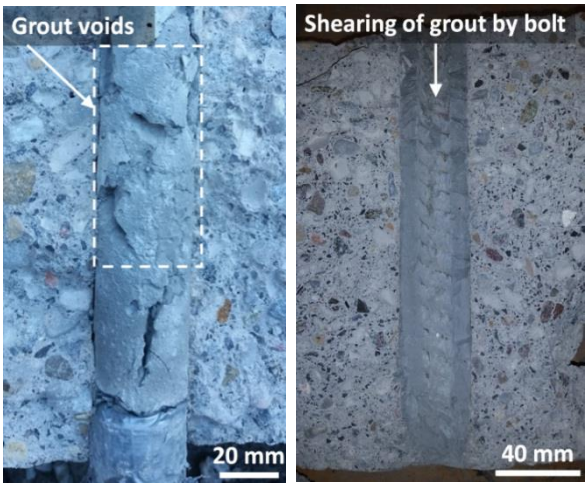

Figure B.21: Specimen *e* post testing analysis

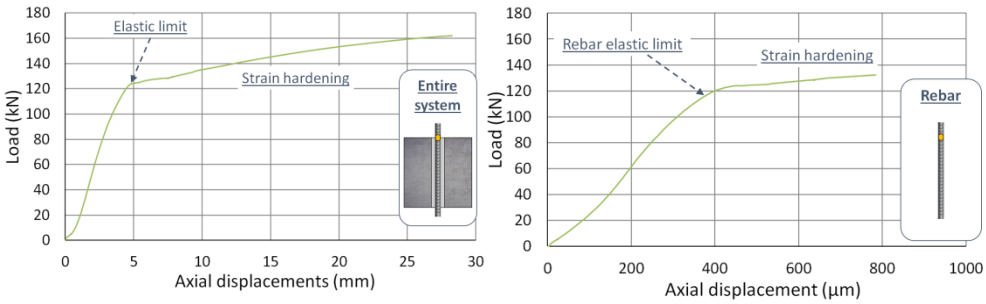

Figure B.22: Load-displacement curves for specimen *e*, loaded up to failure. Left; Support system response. Right; Rebar response

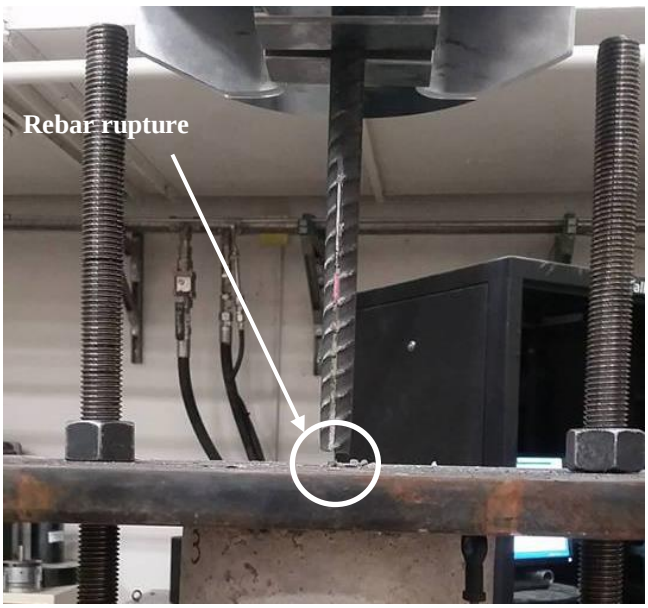

Figure B.23: Tensile failure of rebar in specimen *e* (Cruz, Forbes, & Vlachopoulos, 2016)

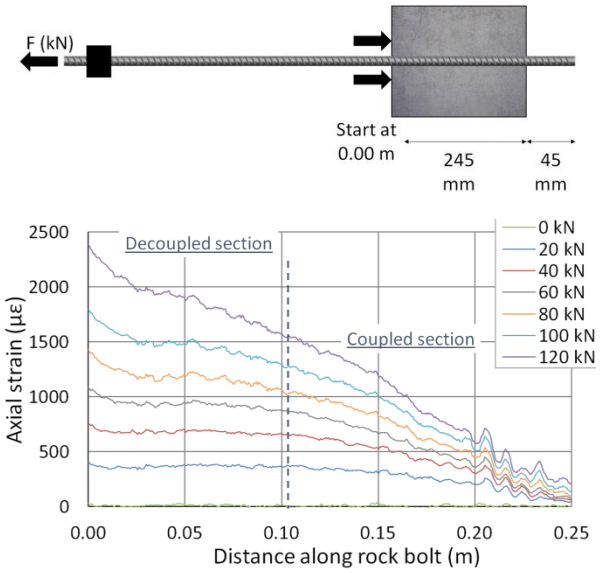

Figure B.24: DOS strain profile results for specimen *e*, loaded up to failure (embedded bolt section only)

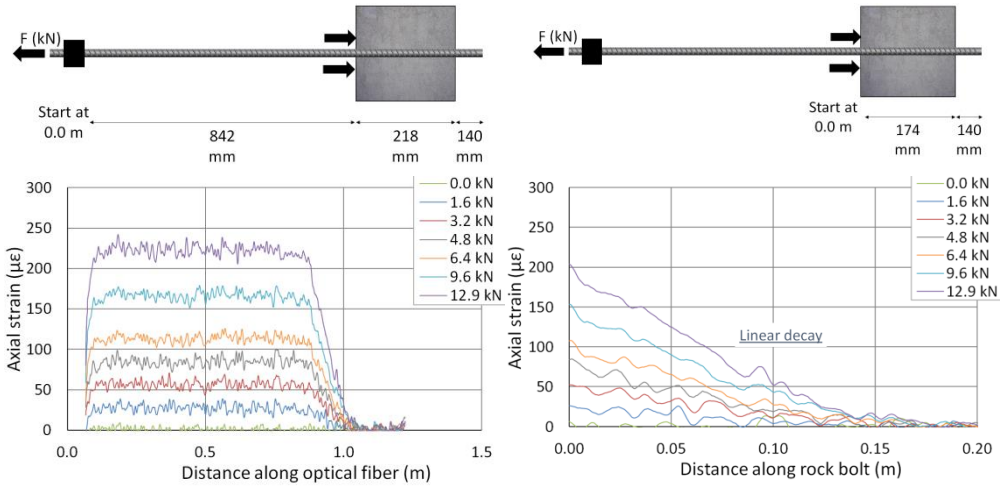

Figure B.25: Strain profile results for specimen *b*. Left; Results along entire bolt length. Right; Results along embedded bolt section

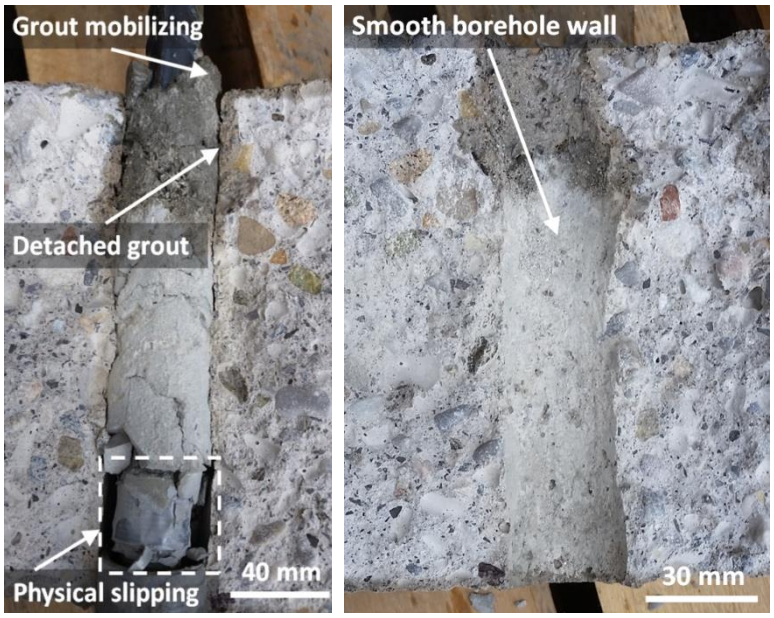

Figure B.26: Specimen *b* post testing analysis

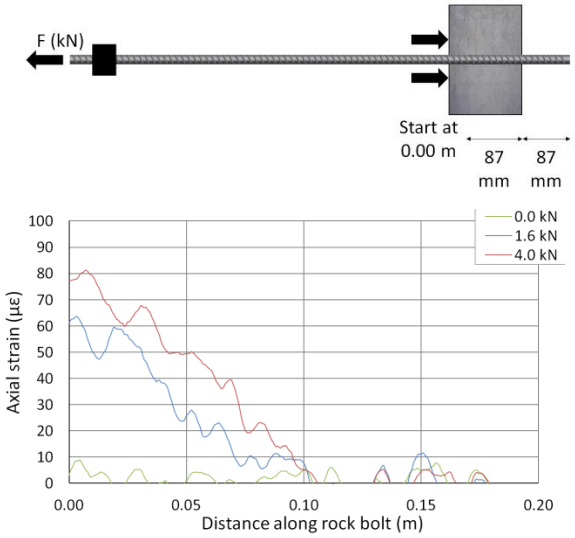

Figure B.27: Detailed strain profile along embedded region of rebar for specimen *c* (embedded bolt section only)

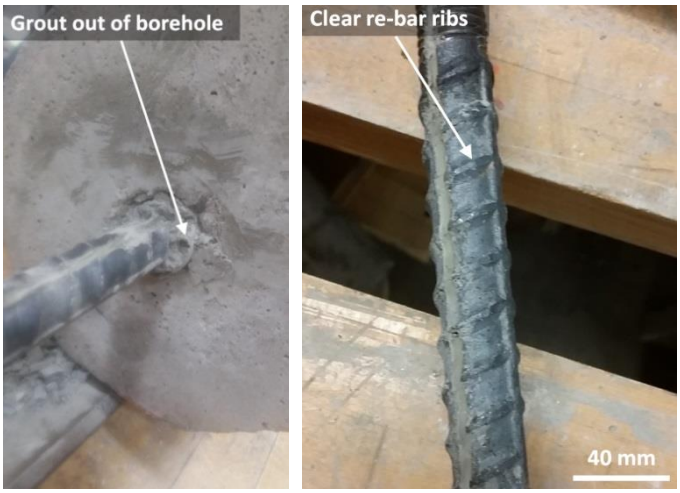

Figure B.28:: Specimen *c* post testing analysis

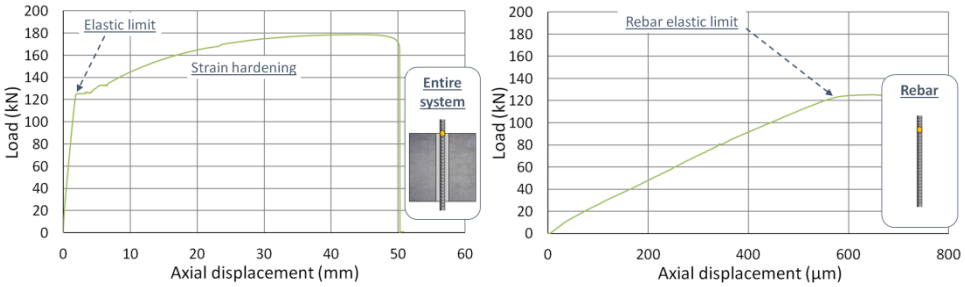

Figure B.29: Load-displacement curves for specimen *f*. Left; Support system response. Right; Rebar response

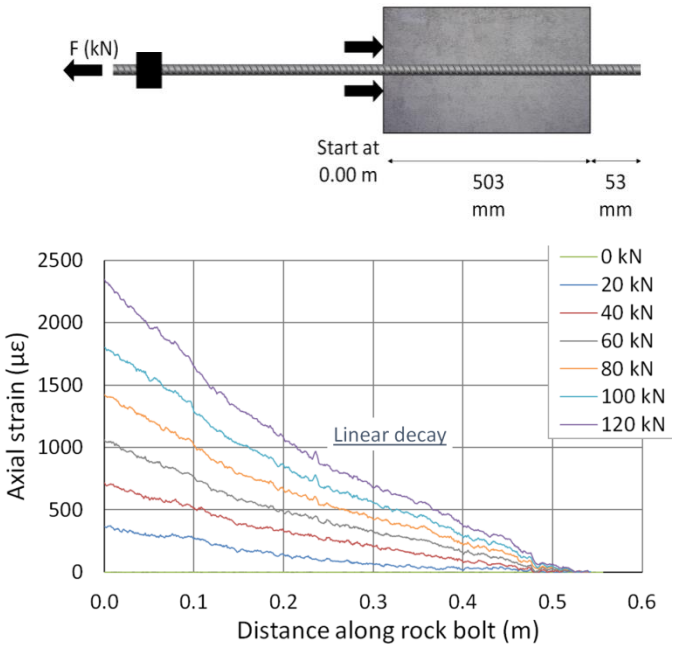

Figure B.30: Load-displacement curve for specimen *f* (embedded bolt section only). Left; Conventional instrumentation. Right; Rayleigh DOS

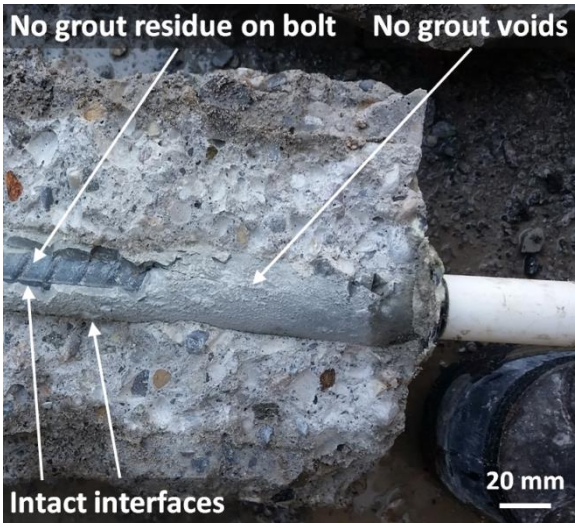

Figure B.31: Specimen *f* post testing analysis

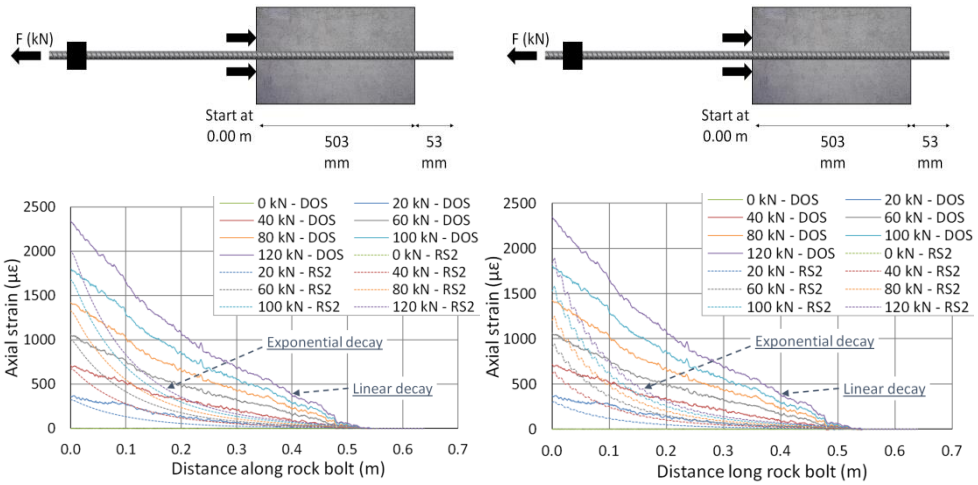

Figure B.32: Numerical model strain profile results for specimen *f* (embedded bolt section only). Left; RS2 model with no ribs. Right; RS2 model with ribs

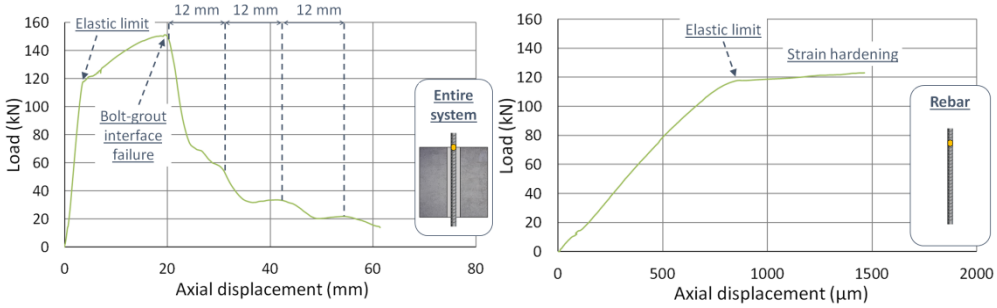

Figure B.33: Load-displacement curves for specimen *o*. Left; Support system response. Right; Rebar response

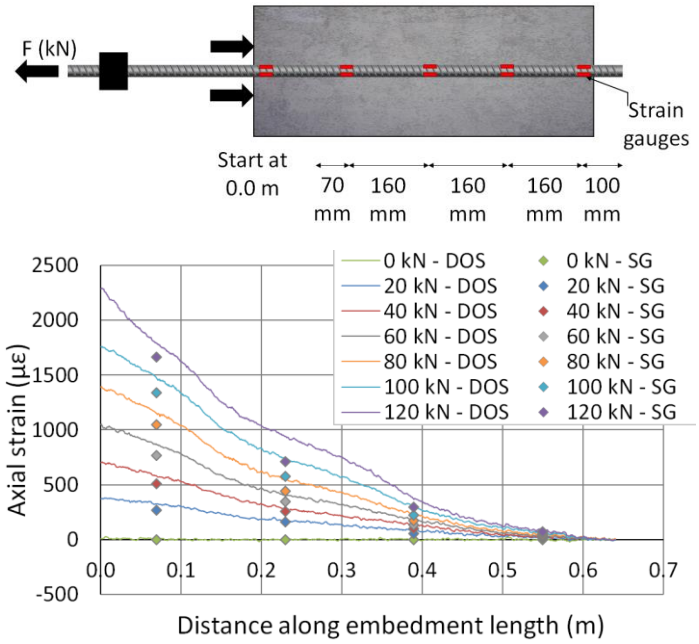

Figure B.34: Strain profile results for specimen *o* along embedded bolt section (strain gauge results in diamonds)

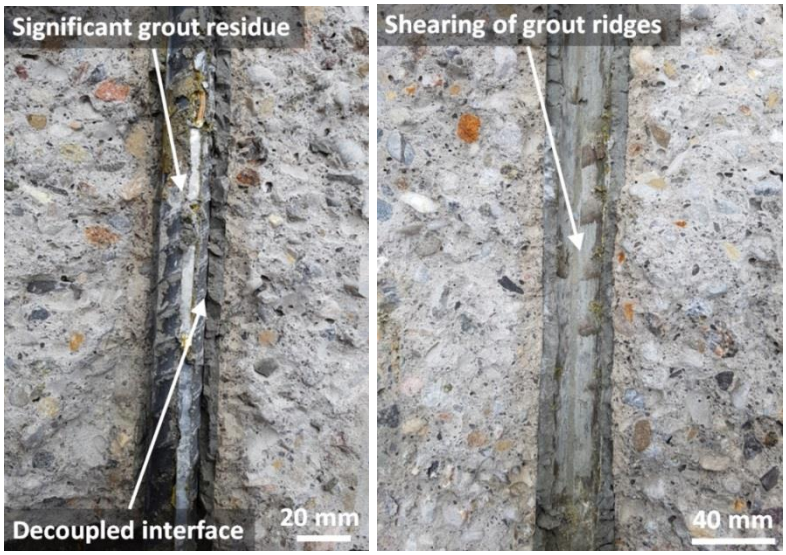

Figure B.35: Specimen *o* post testing analysis

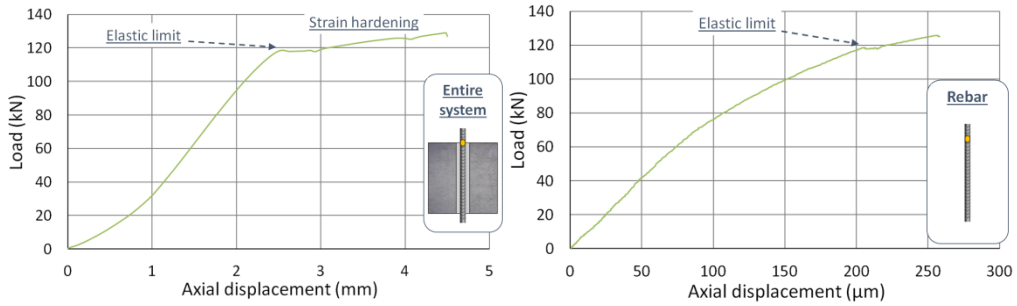

Figure B.36: Load-displacement curves for specimen *h*. Left; Support system response. Right; Rebar response

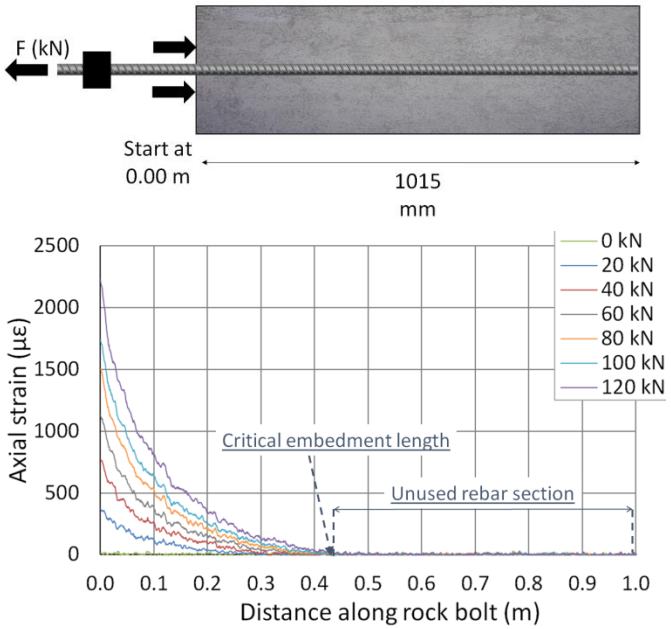

Figure B.37: DOS strain profile results for specimen *h* (embedded bolt section only)

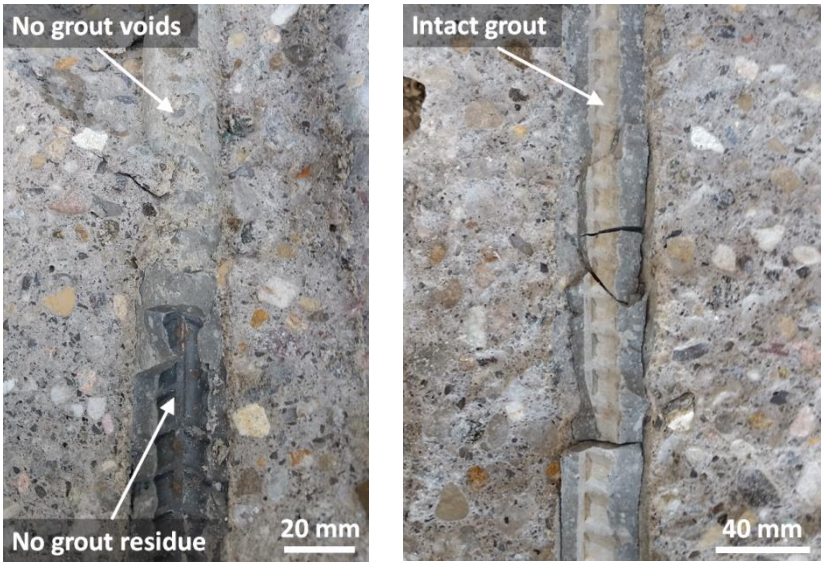

Figure B.38: Specimen *h* post testing analysis

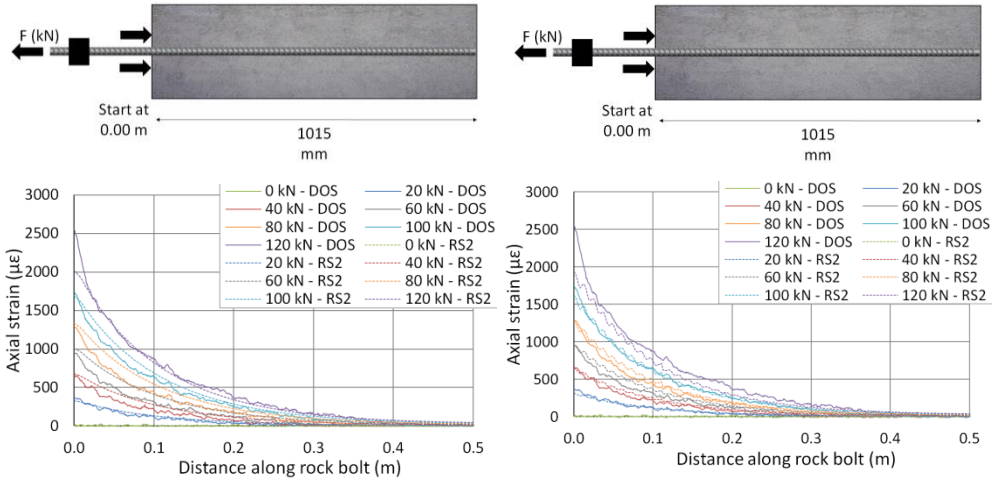

Figure B.39: Numerical model strain profile results for specimen *h* (embedded bolt section only). Left; RS2 model with no ribs. Right; RS2 model with ribs

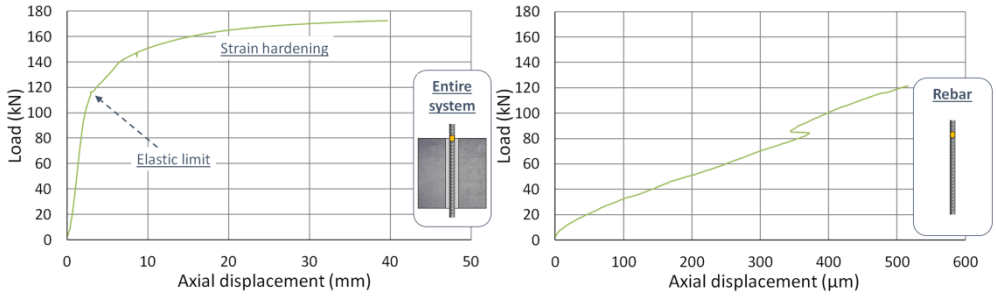

Figure B.40: Load-displacement curves for specimen *g*. Left; Support system response. Right; Rebar response

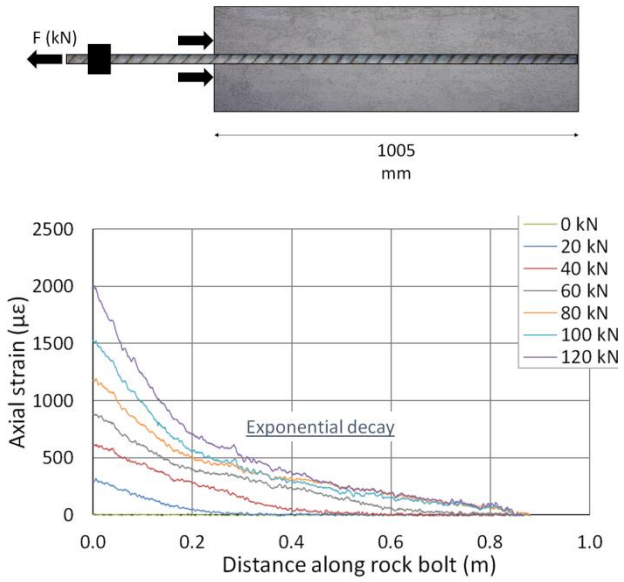

Figure B.41: DOS strain profile results for specimen *g* (embedded bolt section only)

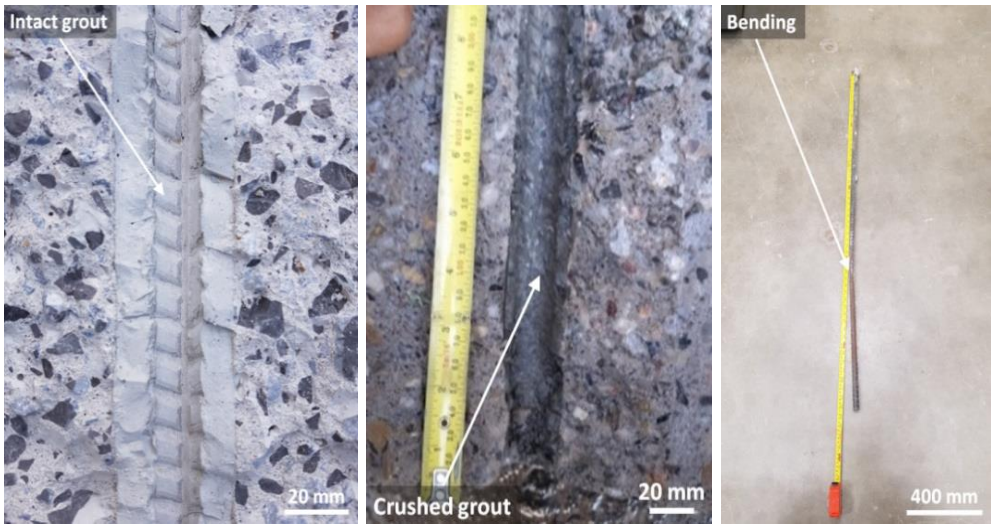

Figure B.42: Specimen *g* post testing analysis

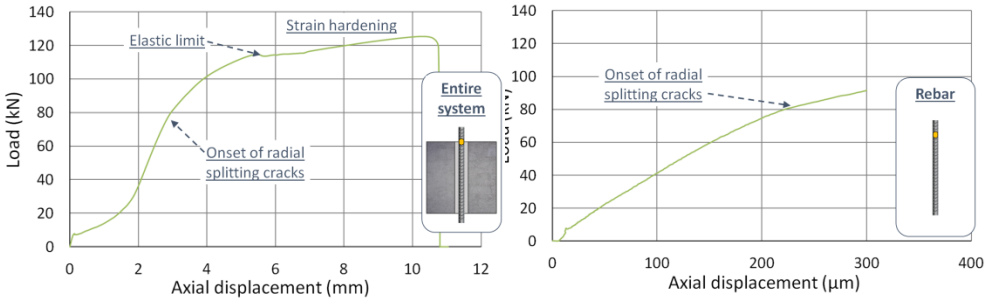

Figure B.43: Load-displacement curves for specimen *j*. Left; Support system response. Right; Rebar response

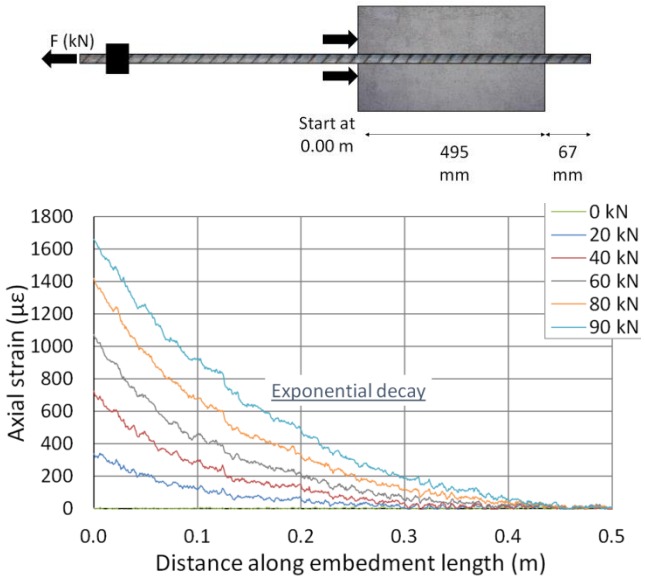

Figure B.44: DOS strain profile results for specimen *j* (embedded bolt section only)

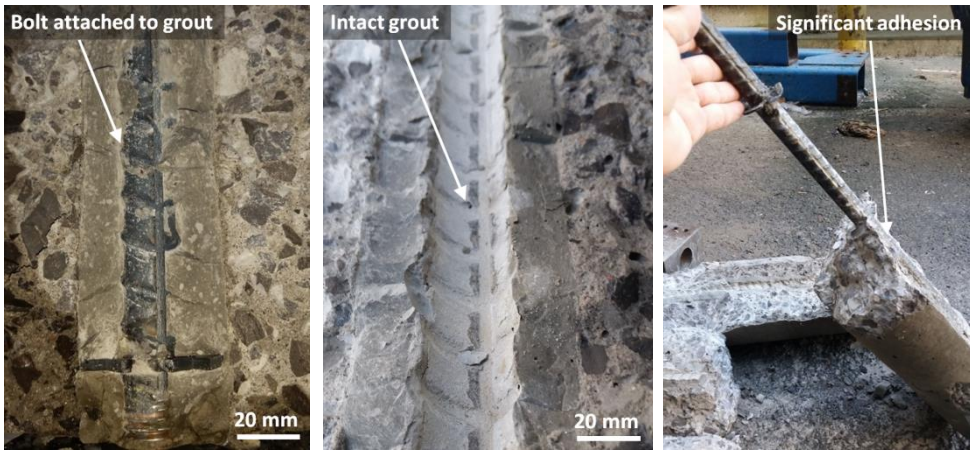

Figure B.45: Specimen *j* post testing analysis

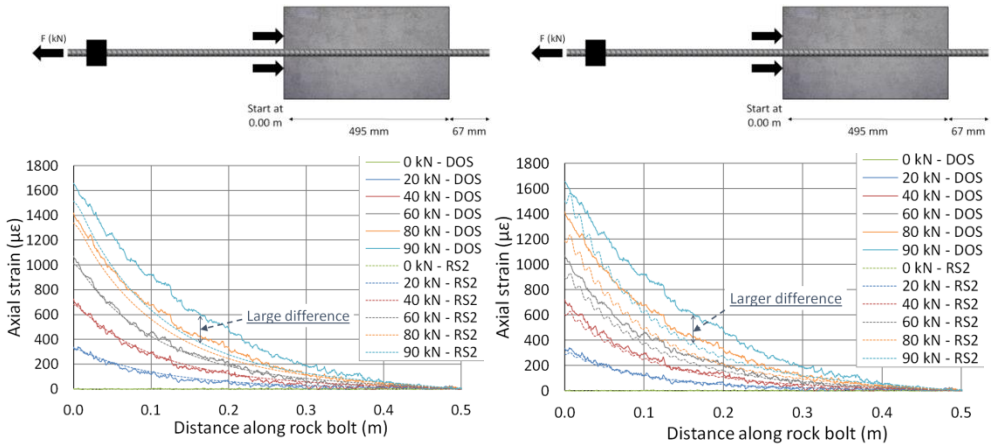

Figure B.46: Numerical model strain profile results for specimen *j* (embedded bolt section only). Left; RS2 model with no ribs. Right; RS2 model with ribs

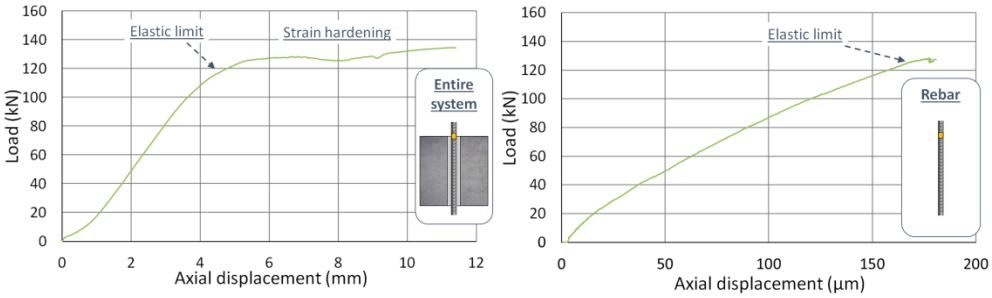

Figure B.47: Load-displacement curves for specimen *n*. Left; Support system response. Right; Rebar response

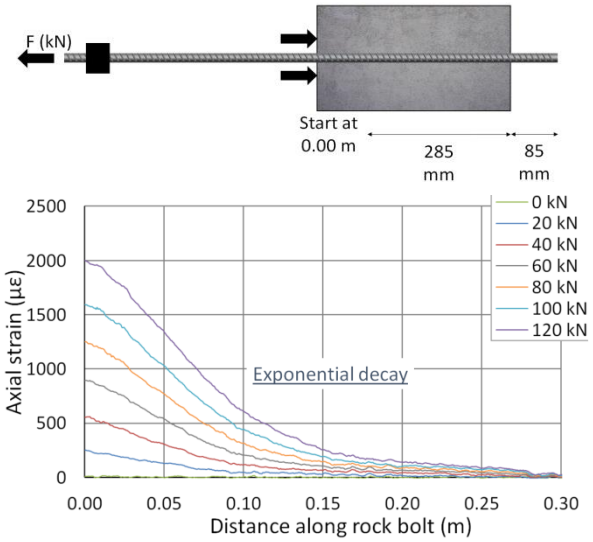

Figure B.48: Detailed strain profile results for specimen *n* (embedded bolt section only)

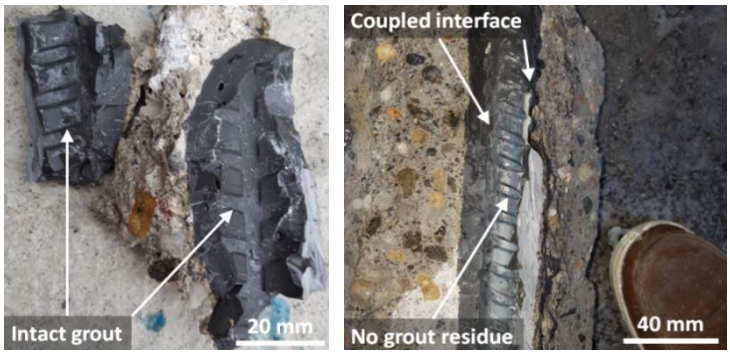

Figure B.49: Specimen *n* post testing analysis

Figure B.50: Resin encapsulation of rebar and borehole wall

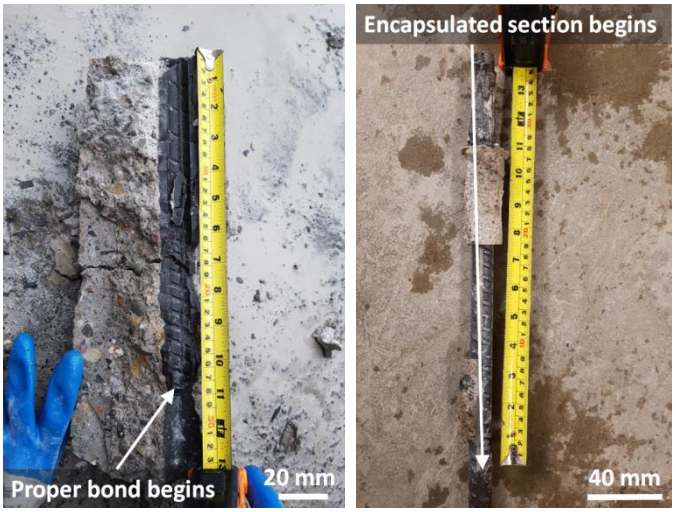

Figure B.51: Effective embedment length of specimen *n*

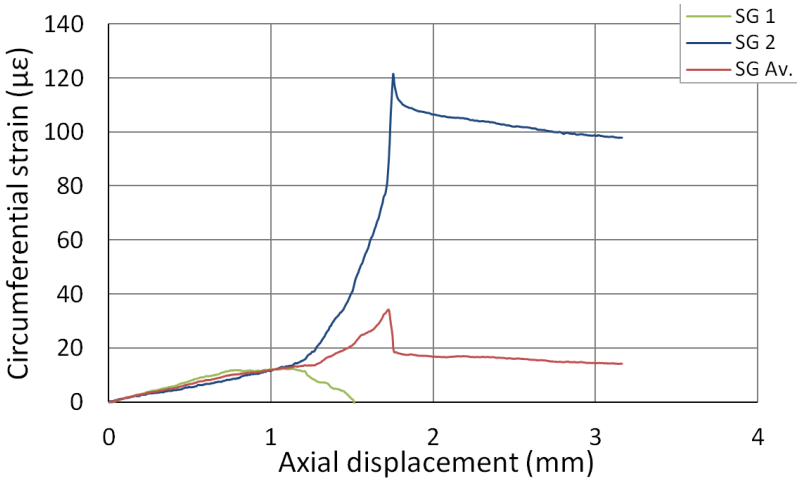

Figure B.52: Specimen *m* strain gauge results

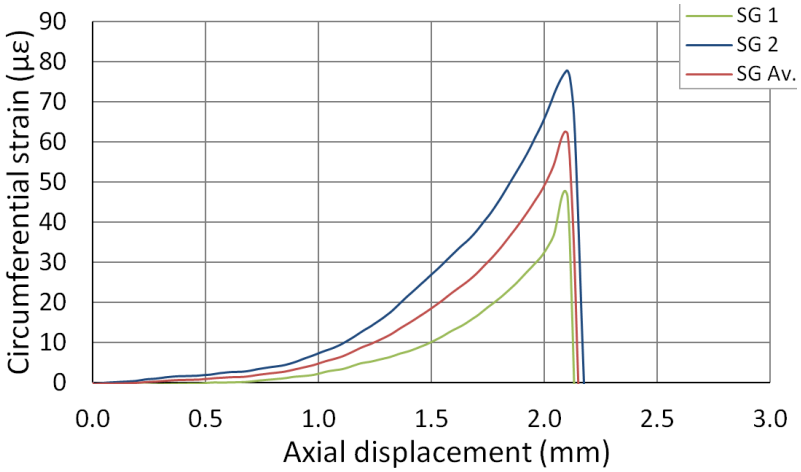

Figure B.53: Specimen *k* strain gauge results

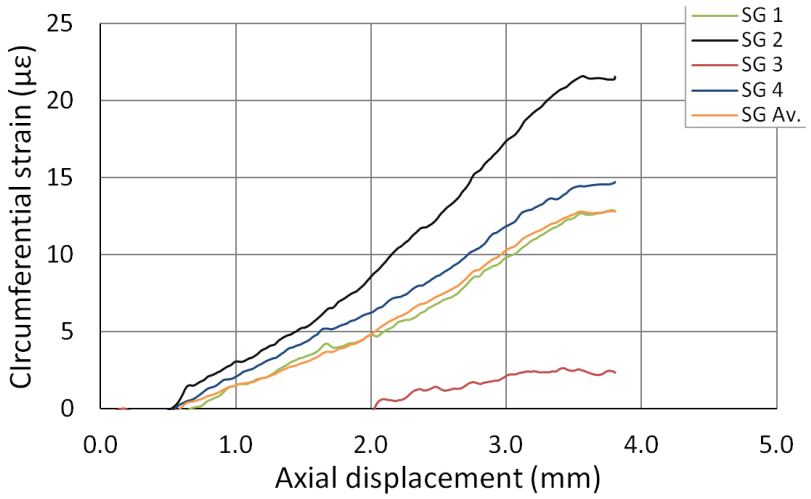

Figure B.54: Specimen *i* strain gauge results

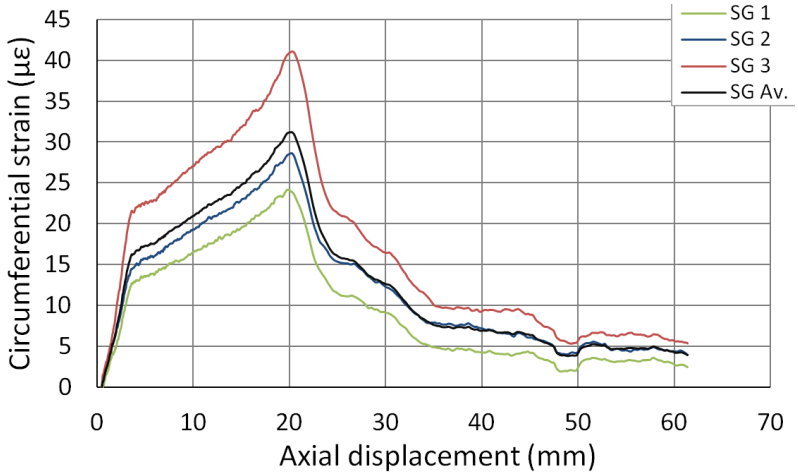

Figure B.55: Specimen *o* strain gauge results

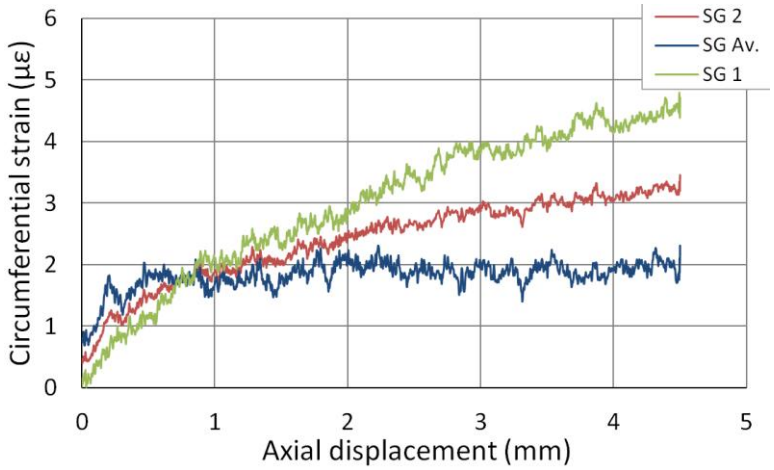

Figure B.56: Specimen *h* strain gauge results

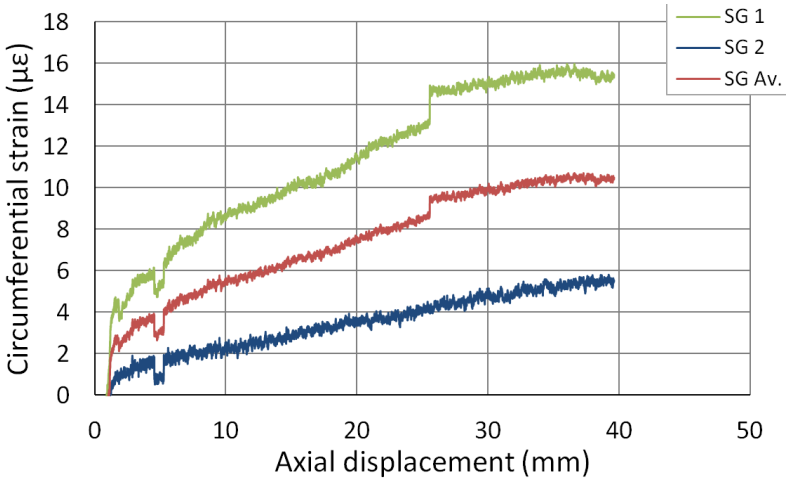

Figure B.57: Specimen *g* strain gauge results

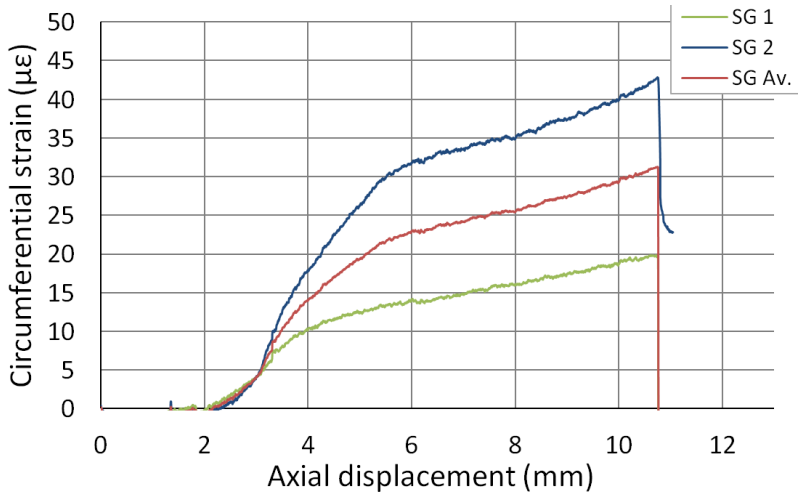

Figure B.58: Specimen *j* strain gauge results

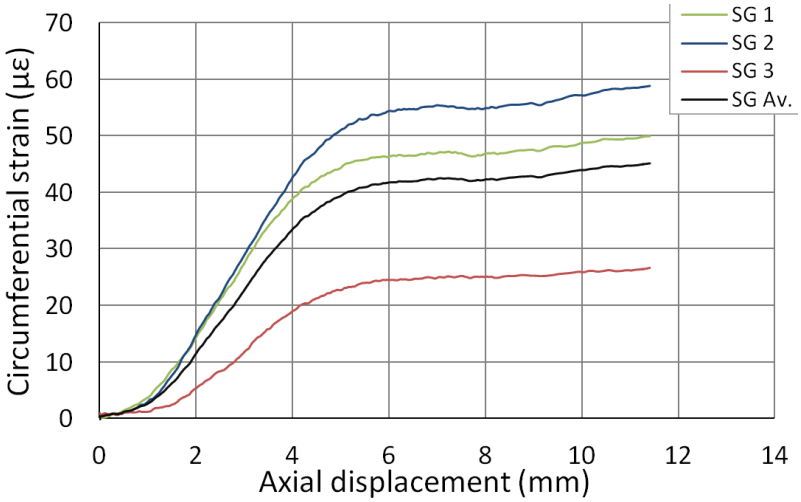

Figure B.59: Specimen *n* strain gauge results

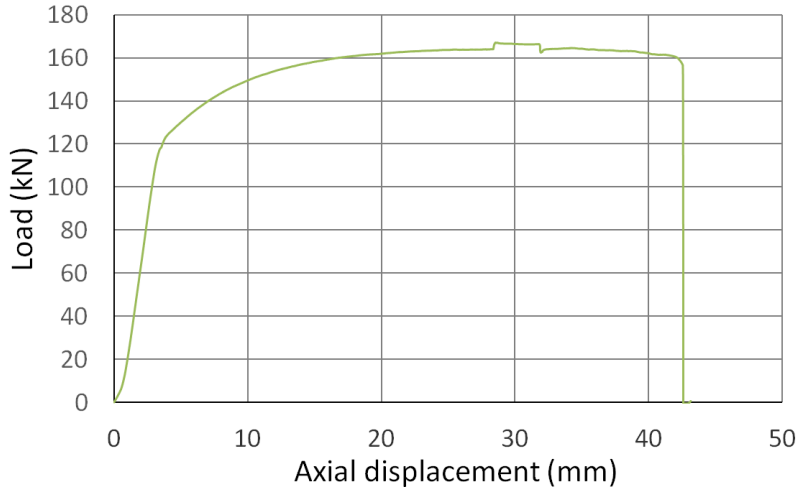

Figure B.60: Specimen *d* load displacement curve attained with conventional instrumentation

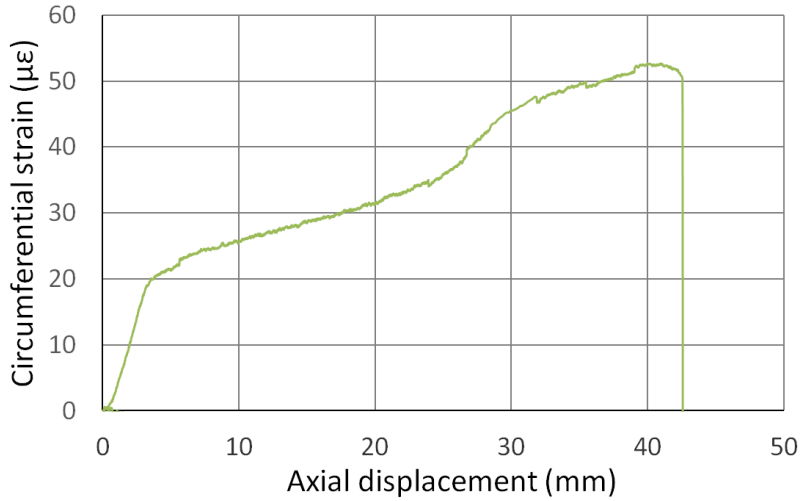

Figure 0.61: Specimen *d* strain gauge results